SYNTHESIS OF POROUS GRAPHENE FROM SRI LANKAN GRAPHITE FOR SUPERCAPACITOR APPLICATIONS

Makandana Kankanamalage Ayesha Sandaruwani

198043F

Thesis submitted in partial fulfillment of the requirements for the degree
Master of Philosophy

Department of Materials Science and Engineering
University of Moratuwa
Sri Lanka

July 2022

DECLARATION

I declare that this is my own work, and this thesis does not incorporate without acknowledgement any material previously submitted for a Degree or Diploma in any other University or Institute of higher learning and to the best of my knowledge and belief it does not contain any material previously published or written by another person except where the acknowledgement is made in the text.

I hereby grant to The University of Moratuwa the irrevocable, non-exclusive, and royalty free license to archive and make accessible my work in whole or in part in all forms of media, now or hereafter known. I agree that the document mentioned above may be made available immediately for worldwide access unless an embargo applies.

I retain all other ownership rights to the copyright of my work. I also retain the right to use in future works (such as articles or books) all or part of my work. I understand that I am free to register the copyright to my work.

Signature: Date:

M.K.A.Sandaruwani

The above candidate has carried out research for the MPhil thesis under my supervision.

Signature of the supervisor: Date:

Name of the Supervisor: Dr. (Mrs)H.S.Sitinamaluwa

Signature of the supervisor: *UOM Verified Signature* Date: 23/11/2021

Name of the Supervisor: Dr. G.D.D. Galpaya

ACKNOWLEDGEMENT

I would like to give my acknowledge and warmest thank to my research supervisor, Dr.(Mrs) H.S.Sitinamaluwa, not only for her guidance throughout my research but also for the knowledge and experience that she has shared with me. Her guidance and advice carried me through all the stages of this research she played a major role in my career development also. Next, I would also like to thank my other supervisor, Dr. Dilini Galpayage for her brilliant comments and suggestions.

The staff [Academic and Non-academic] at the Department of Materials Science and Engineering, especially all the research assistants who were there with me working together is a main part of the success of this research. I would like to give my heartiest gratitude to all of them for being with me. I would like to give my special thanks to all the academic and non-academic staff of the Department of Chemical and Process Engineering, who helped me to make this work possible.

Finally, I would like to acknowledge SRC grant of SRC/CAP/2019/01, which provided the financial assistance for this project.

ABSTRACT

A feasible process to synthesize porous graphene with ultra-high surface area is presented in this thesis. Graphene oxide (GO) was synthesized from Sri Lankan graphite via the modified hummers method. Then, GO was subjected to a chemical activation process to produce graphene with a mesoporous structure, where KOH was used as the activation agent. The influence of the critical activation process parameters on the specific surface area of graphene was studied. In this study, activation time at 60 min, activation temperature at 800 ℃ and KOH/GO mass ratio at 4 were identified as the optimum activation parameters for high surface area. As an alternative route to find the specific surface area (SSA), a dye adsorption based SSA calculation method was followed, and the methylene blue adsorption kinetics were studied for that. Second order kinetic model and Langmuir isotherms were the most suitable kinetic models for the methylene blue adsorption onto porous graphene which were produced from Sri Lankan vein graphite. A combined mathematical model of methylene blue number (MBN) and iodine number (IN) was used to calculate the SSA for high accuracy. The obtained optimum activated graphene sample showed a high specific surface area of 768.15 m^2/g as measured from the dye adsorption method and it was verified by BET analysis. Furthermore, methylene blue and Iodine adsorption methods are studied as a low-cost and feasible method for surface area determination of porous graphene. The high surface area of the obtained graphene would make it a promising material for supercapacitor applications. The present study mainly focuses on the value addition to Sri Lankan vein graphite trough the utilization of vein graphite as an electrode material in electrochemical double layer capacitor (EDLC).

Contents

LIST OF FIGURES

LIST OF TABLES

LIST OF ABBREVIATIONS

Abbreviation	Description
GO	Graphene Oxide
AGO	Activated Graphene Oxide
SSA	Specific Surface Area
BET	Brunauer, Emmett and Teller
XRD	X-Ray Diffraction
SEM	Scanning Electron Microscopy
FTIR	Fourier Transform Infrared
EDX	Dispersive X-Ray analysis
EDLC	Electrochemical Double Layer Capacitor
KOH	Potassium Hydroxide

1. INTRODUCTION

Nowadays, a quality life in the modern society is heavily dependent on fossil fuels, however, the current model of the modern society is becoming unsustainable, specially due to rapid depletion of fossil fuels and the brutal environmental concerns associated with its usage [1]. Hence, sustainable energy consumption is at utmost importance, which can be accomplished through developing alternative energy sources (e.g. renewable energy sources) and sustainable energy storage technologies [3,4]. Among the currently available energy storage technologies, supercapacitors play a key role due to their advantages such as fast response, higher charging efficiency, long lifetime and wide operating temperature range [4]. Among the supercapacitors, electrochemical double layer capacitor (EDLC) is much preferred, specially due to its high efficiency and cycling stability [5–8].

The electrode material is a key component for supercapacitor performance. The mechanism of the charge accumulation is the main factor which manipulate the supercapacitor performance. Therefore, porous materials are ideal to use as the electrode material in supercapacitors due to its ability to store the electrolyte ions in its pores for the charge accumulation. Hence, carbon-based materials such as graphene, carbon aerogels, activated carbon, and carbon nanotubes are promising as EDLC electrodes owing to their high surface area, availability, low cost, and well-established electrode production technologies [9]–[17]. Activated carbon has got a great deal of attention in electrochemical double layer capacitors, due to its precursor availability, cost effectiveness and specially the high specific surface area which promotes the charge accumulation for the capacitance [18].

The objective of this research is to propose a feasible synthesis process to develop a graphene-based electrode material using Sri Lankan vein graphite. It is expected to develop an electrode material which has ultra-high surface area for EDLC application, in order to develop supercapacitors with higher energy density compared with existing devices. Sri Lankan graphite has a huge potential to use for energy storage applications, however its performance on EDLC electrodes has not well studied yet. Mohsin Ali Raza [19] and his group have compared the surface area of GOs which were

synthesized from various graphite sources. They have proven the capability of Sri Lankan graphite of promoting the product for higher surface area compared to other tested graphite sources. Therefore, Sri Lankan graphite was used as the starting material for this research, after considering its promising properties such as high purity (above 98 %) [20], high crystallinity and extensive mineralization [21].

Wettability of the electrode by the electrolyte is an important factor for high charge accumulation in the electrode [22–24]. Wettability of the electrode is the ability of the electrode material to be wetted by the electrolyte, which facilitates the transport of electrolyte ions into the electrode pores. For that purpose, a pore structure with matching pore sizes and pore connectivity is important. Recent studies have proven that the pore size range of 0.7-3 nm (micro/meso structure) shows the best performance in EDLCs [10–12]**.** Hence, pore structure tailoring is a prominent approach to enhance the electrochemical capacitance of the electrode material.

Graphene is a promising material in developing EDLC electrodes with low thickness and high conductivity, and very low electrical resistivity [26]. Theoretically, graphene has much higher specific surface area (SSA) around 2630 m^2/g and, it can attain a capacitance value up to 550 F/g when its SSA is fully utilized [17]. Though graphene has theoretically high specific surface area, practically attaining this value is a challenge due to its tendency of layer restacking or agglomeration [15, 16]. KOH activation is a promising method for pore structure tailoring of graphene oxide, which results in a mesoporous structure[15–18].To enhance the specific surface area, chemical activation with activation agents such as KOH has been studied as a successful approach [17, 18].

This research focuses to propose a feasible synthesis route to develop a graphene-based electrode material with high surface area and tailored pore structure, which has potential application on EDLCs. A dye adsorption method is introduced as an alternative method to BET analysis to determine the specific surface area of porous graphene oxide. Methylene blue and iodine adsorption is performed, and their kinetics are studied to clearly understand the adsorption mechanism. Then the SSA which is calculated from dye adsorption method is confirmed by BET analysis. Furthermore,

structure, morphology and material properties of graphite powder, graphene oxide and activated graphene oxide were characterized using variety of techniques, and the changes occurring during synthesis process is discussed in detail. Finally, the activation mechanism is optimized for the critical parameters, which are activation time, temperature, and duration. Here, Sri Lankan vein graphite from Bogala graphite mine is used as the raw material. The outcome of this research will give a novel insight on utilization of Sri Lankan vein graphite for energy storage technologies. Also, the outcome of this research is much beneficial for the industries which are focused on development of value-added products from Sri Lankan vein graphite.

2. LITERATURE REVIEW

2.1. Energy storage devices

The dependence of the modern society on fossil fuels has been problematic due to the increase of the cost of fuels, environmental pollutions such as global warming due to the fossil fuel burning, and geopolitical concerns [1]. It is important to find solutions for these matters, and one promising way is moving to renewable energy sources. However, sustainable energy storage solutions are much needed to effectively utilize the renewable energy sources [3,4]. Therefore, the increasing global energy demand and moving to sustainable energy sources can be linked with the rapid development of sustainable energy technologies [34].

In recent years, more attention has been given to protect the natural resources. For this purpose, search for renewable energy sources (most notably, solar and wind energy) became popular, however, as the energy demand continues to grow, improving energy storage capability was essential due to the seasonal availability of these renewable energy sources [5,21]. Batteries (Li-ion, Li-sulfur, Li-air, Na-ion, Lead-acid, Ni-Cd, Ni-MH) and supercapacitors are the mainly available energy storage devices [4].

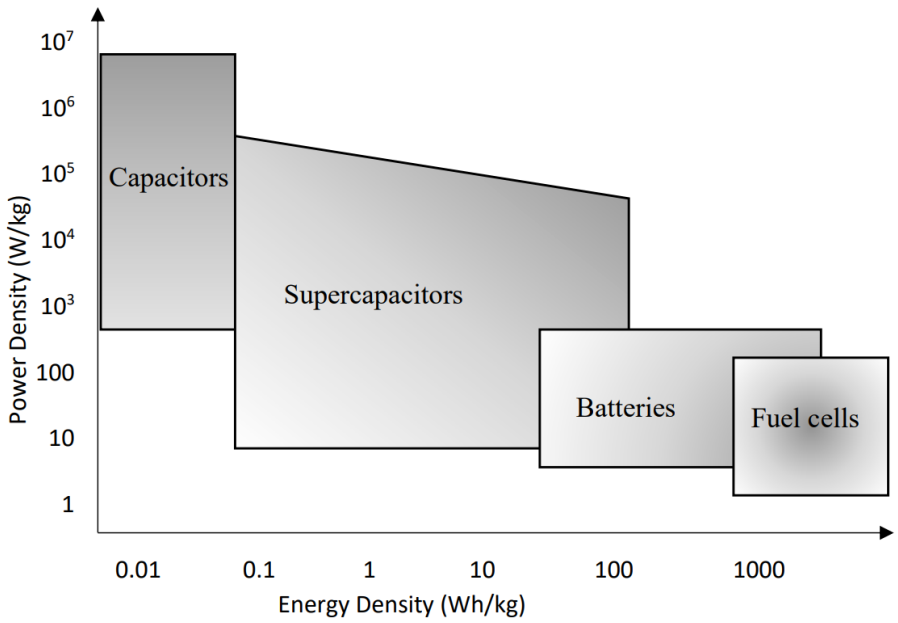

Figure 1. Ragone plot [36]

The Ragone plot demonstrated in Figure 1 compares the energy densities and power densities of several energy storage devices. According to the Ragone plot, supercapacitors can deliver high power density compared to batteries and fuel cells; however, their energy densities are lower than that of batteries and fuel cells. Therefore, increasing the energy densities of existing supercapacitors would result in a device with both high energy and power density, which meets the industry demand.

Chemical and physical mechanisms are the respective storage mechanisms for the batteries and supercapacitors respectively. Therefor the power is limited on the reaction kinetics in batteries and on the electrolyte conductivity in supercapacitors. Even though the charge rate is kinetically limited in the batteries, it is not limited in supercapacitors[1]. Lithium-ion battery is the most commonly used energy storage device which have 10-60 minutes charge time and 1000-3000 W/kg specific power. However, supercapacitors show higher performance than lithium-ion batteries having rapid charge/dischage time typically at 1-10 seconds and specific power upto 10000 W/kg. Hence, supercapacitors are much attractive class of energy storage devices, having an extremely high cyclability (higher than 100,000 cycles), high power density and fast charge/discharge [16].

2.2. Supercapacitor categories

Electrochemical capacitors, also named as ultra-capacitors and supercapacitors, comprise of two electrodes with a separator between them as illustrated in Figure 2. The element which blocks the electrical contact between the two electrodes is called the separator and it is soaked in the electrolyte in between the electrodes. The supercapacitors generally have much higher capacitance compared to conventional capacitors. There are three types of supercapacitors; which are electrochemical double layer capacitors (EDLC), pseudocapacitors and hybrid capacitors, categorized based on their charge storage mechanism. EDLCs use electrostatic interaction to accumulate energy via creating an electrical double layer on the interface between the electrode and the electrolyte. The double layer capacitance is arising from the energy which is stored electrostatically at the interface of the electrode and the electrolyte in the capacitor. The phenomenon of the pseudo capacitance is different from EDLC, where electrode materials in the pseudo capacitor undergo redox reactions to transfer the

electrons. The pseudo capacitance occurs at the electrode surfaces, where faradaic reactions origin, and the reactions affecting to the movement of energy across the double layer. The combination of EDLC and pseudo capacitor is called as hybrid capacitors. Further details about these supercapacitor categories and their working principles are explained below.

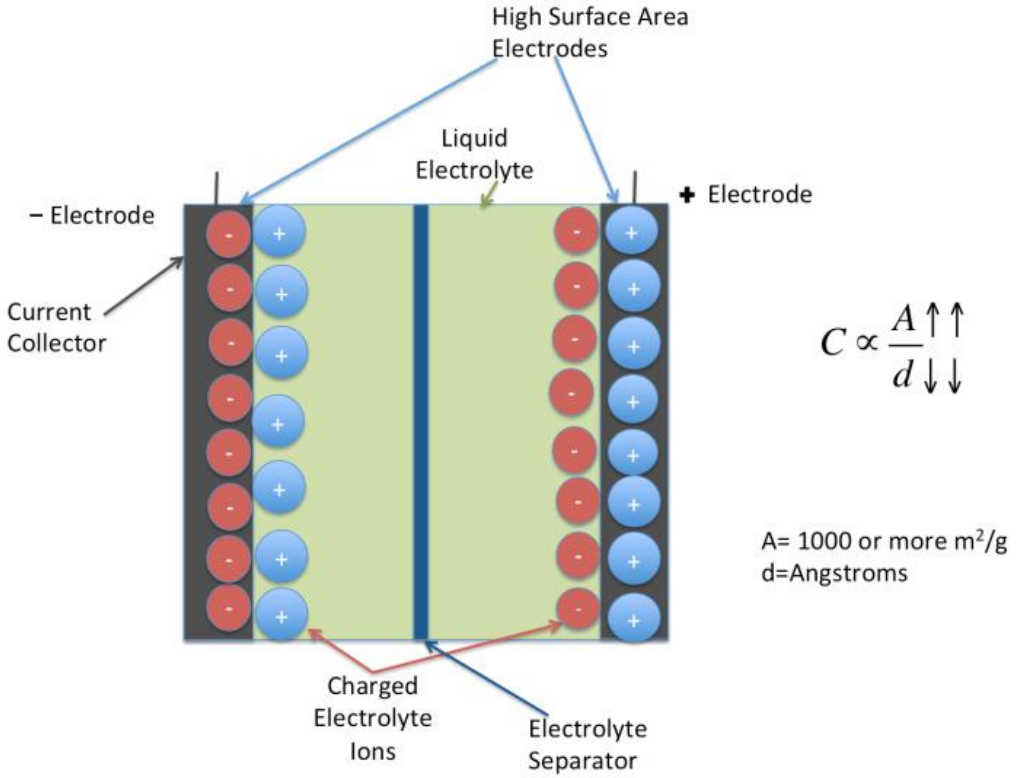

Figure 2. Schematic diagram of supercapacitor [37]

Electrostatic interaction in EDLC is used to gather the energy in Helmholtz double layer on the interface among electrodes and the electrolyte. Double layer capacitance is occurring from the potential deference, which is kept electrostatically at the boundary of capacitor electrodes. The key structural feature to gain an exceptionally high capacity is the large surface area of electrode material which have low Helmholtz layer thickness. Pseudocapacitors and hybrid capacitors have low durability and low cycling stability due to its electrodes tends to degradation by redox reactions. However, in EDLC, redox reactions do not take place, and the energy is collected non-faradaically being the reason to possess good durability and high cycling stability. Due

to these performances and much higher capacitance, EDLC is the most common type of supercapacitor in different sectors such as consumer electronics, automotive, energy, and industrial sectors [38].

The second category is pseudocapacitors or faradaic supercapacitors. The pseudocapacitance is developed at the surface of the electrode and the electrolyte, where faradaic reactions occur, and these reactions connects the energy transferring route across the double layer. The disadvantage of pseudocapacitors is the faster degrading of the electrode due to the stress on the electrode material during its charging and also discharging processes. Pseudocapacitive materials like manganese dioxide (MnO_2) and ruthenium oxide (RuO_2) are used for the preparation of the electrodes of the pseudocapacitors. The main drawbacks of the pseudocapacitors compares to EDLCs are the lower stability, cyclability and charging efficiency and the longer time response [39].

The newest category of the supercapacitor is hybrid supercapacitors that the combination of pseudocapacitor and EDLC. The main advantage of hybrid supercapacitor is the greater volumetric and gravimetric energy density which is relates to provide high currents. Higher energy density is due to the occurrence of the faradaic reactions on the negative electrode. This negative electrode is created from a pseudocapacitive material as in pseudocapacitors. Hybrid supercapacitors can deliver higher currents as EDLCs, as the electrostatic energy is stored in a double layer at the positive electrode interface. This positive electrode is made from a porous material like activated carbon. Hybrid supercapacitors have same assembling and operation principle as lithium-ion batteries [39].

Figure 3 illustrates the charging mechanism of three types of supercapacitors. Among these supercapacitor categories, pseudocapacitors have the main disadvantage of fast degradation of electrode. Hybrid supercapacitors also have the similar drawback due to its pseudocapacitive negative electrode. Therefore, in comparison, EDLC is advantageous due to its high capacitance, fast response, prolonged lifetime and having a wide range in operational temperature [40].

Among supercapacitor categories, EDLC can be used for energy storage applications with the benefits of fast response, higher charging efficiency, long lifetime, and wide range in operational temperature. EDLC is a promising technology, which certainly performs a most important role in satisfying the demand of electronic devices for present and future.

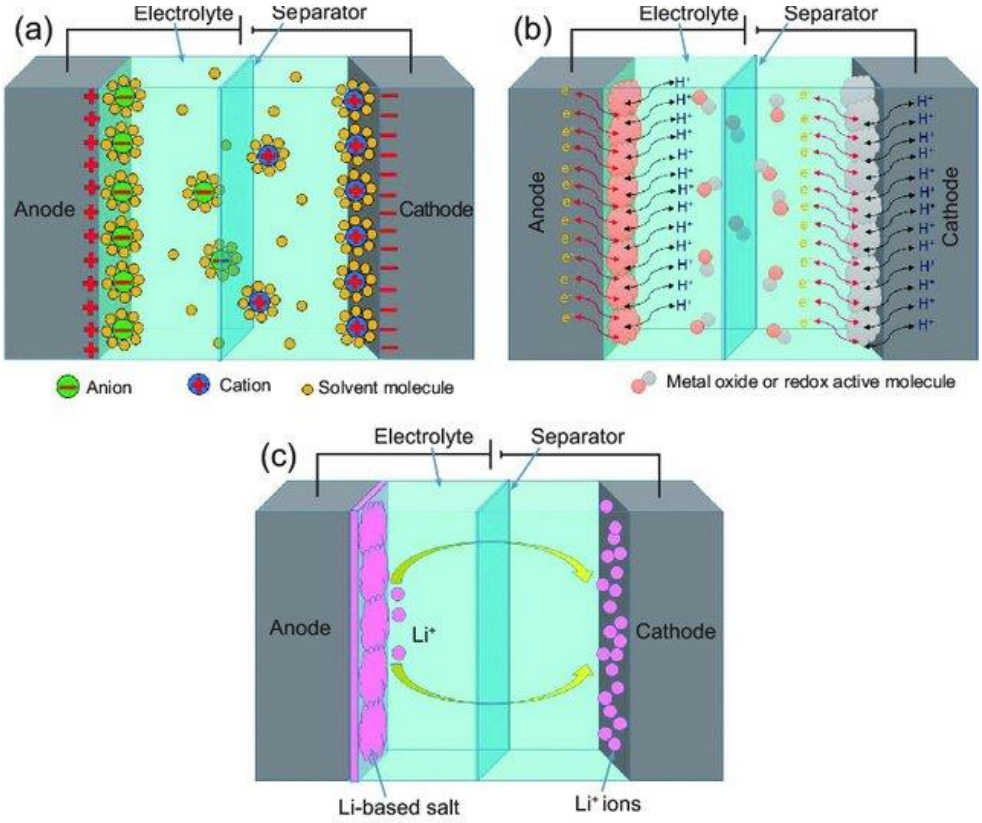

Figure 3. Diagrams of (a) electric double layer capacitor (EDLC), (b) Pseudocapacitor, and (c) hybrid supercapacitor [41]

2.3. Mechanisms of Electric Double Layer Formation

The electric double layer is created in between a charged object and a liquid. When a charged body is positioned in a liquid, the counter charges from the liquid concentrate near the surface of the charged body forming a double layer. As illustrated in Figure 4, there are three models which describe this phonomenon, namely Helmholtz model, Gouy-Chapman model and Stern model; where ψ is the potential, ψ_0 is the electrode potential, IHP is the inner Halmholtz plane and OHP is the outer Helmholtz plane [1]

.

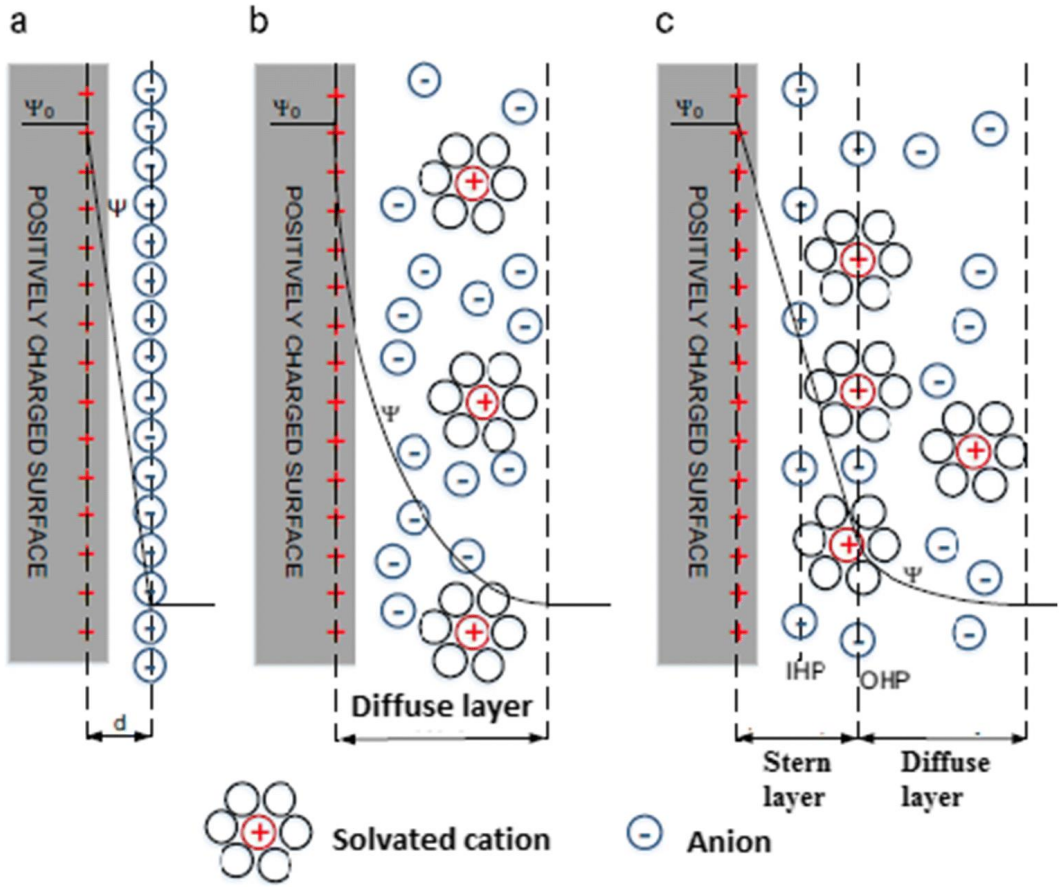

Figure 4. EDL models, (a) Helmholtz model, (b) Gouy-Chapman model, and (c) Stern model

[1]

2.3.1. Helmholtz model

The simplest theoretical model for the spatial charge distribution which occurs at double layer interface is illustrated by the Helmholtz model. The electrode charge is neutralized by the ions which are in opposite sign at a “d” distance. This model is believed as a simplest hypothesis, however, it cannot sufficiently describe the mechanism behind double layer formation [2,3].

2.3.2. Gouy-Chapman or Diffuse model

This model proposes that a liquid surrounding of a charged solid has an equal quantity of opposite ionic charge, but these ions are not tightly bound to the solid surface. Counter ions in the liquid solution are scattered into the solution in thermal disarray.

The thickness of the diffuse layer would be found by on the kinetic energy of these ions in the solution. Gouy and Chapman established the concepts of this diffuse layer which the ions in the solution which are near to the surface behave as the Boltzmann distribution, however, this concept not sufficient to describe a double layer which is highly charged [1].

2.3.3. Stern model for diffuse double layer

Even though the Gouy-Chapman model is based on certain assumptions, it could be considered as a successful model compared to the Helmholtz model. Gouy-Chapman model assumes that ions can approach the surface without any limit because of being point charges. Later, Stern model was introduced by Gouy-Chapman by considering the limits to approach the surface owing to finite size of ions. Therefore, Stern model assumes that some ions are at a distance away from the surface, while the surface adsorbed ions in a particular layer which follow the Stern model. And this layer is identified as the Stern layer. They assumed that the compact layer is a combination of the mostly adsorbed ions (creating the inner Helmholtz plane), and non-particularly adsorbed counter ions (creating the counter Helmholtz plane) [2,3,5].

2.3.4. Electric double layer in supercapacitors

According to Figure 5, the electron transfer is from positively charged electrode to the negatively charged electrode when the supercapacitor is charged, and this electron transferring is happened through an external circuit. Consequently, cations are concentrated at the negatively charged electrode and anions at the positively charged electrode to develop an EDL that balances the external charge imbalance. The electrons move from the negatively charged electrode to the positively charged electrode through an external circuit during the discharge and both positive and negative ions which are in the pores of the electrode mix again until the cell is fully discharged [2].

The movement of ions in the bulk electrode is not similar to the movement of ions into the pores of the electrode material. The movement of ions into the pores are significantly affected by the pore size and the pore structure. When the pore sizes are too small, it will not contribute to double layer capacitance because of the inaccessibility of electrolyte ions into the electrode. Since the size, shape and the orientation of the pores are crucial factors for the accessibility to the ions, a linear relationship cannot be developed between the capacitance and the porosity of the electrode [2].

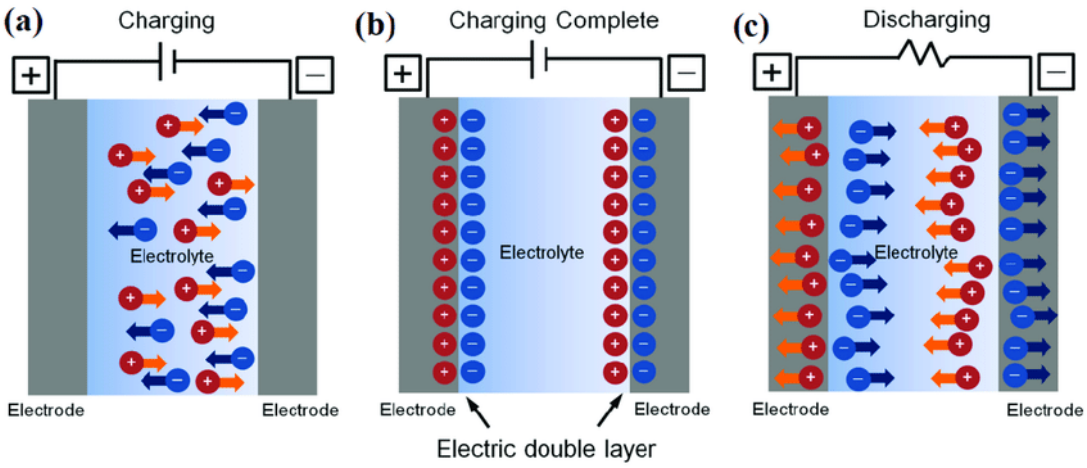

Figure 5. Charging discharging process of electric double layer capacitor [41]

2.4. Electrode materials for EDLC

In EDLC, energy is accumulated in the electrochemical double layer which forms at the electrode and electrolyte interface. Therefore, the electrochemical performance mainly depends on the surface area of the electrode which is accessible to the ions in the electrolyte. EDLC performance depends on the properties of the electrode material such as pore shape and structure, specific surface area, electrical conductivity, pore size distribution, and surface chemistry. Carbon based materials such as carbon nanotubes, activated carbon, carbon aerogels and graphene have attracted a great interest as EDLC electrodes owing to their high surface area, availability, low cost, and well-established electrode fabrication technologies. Graphene and its derivatives have much consideration in this field because of its properties [42].

2.4.1. Important characteristics of electrode material

Performance of EDLC is depended on the combination of properties of electrode, electrolyte, and the device construction. It is easy to improve the EDLC performance by improving the favorable properties of electrode material. The mainly importnatelectrode material properties are the surface area, porous network, surface chemistry, conductivity. Furthermore, the mass of the active material in the electrode is also important.

Surface Area/ pore structure

Generally, the capacitance of EDLC increases with the surface area of the electrode; however, it is not linearly proportional due to the change of the capacitance with the pore structure.

Pore structures are categorized in different groups depending on their pore size and pore shape. Micropores (size <2 nm), ultra-micropores (size <0.7 nm), mesopores (2 nm <size<50 nm) and macropores (size >50 nm) are the pore categories depending on pore size. Figure 6 illustrates the three main pore structures as slits, cylinders, and voids. The pore structure also very critical to the energy storage mechanism in EDLC because it restrict or facilitates the amount of electrolyte ions transportation on to the porous electrode for the double layer formation.

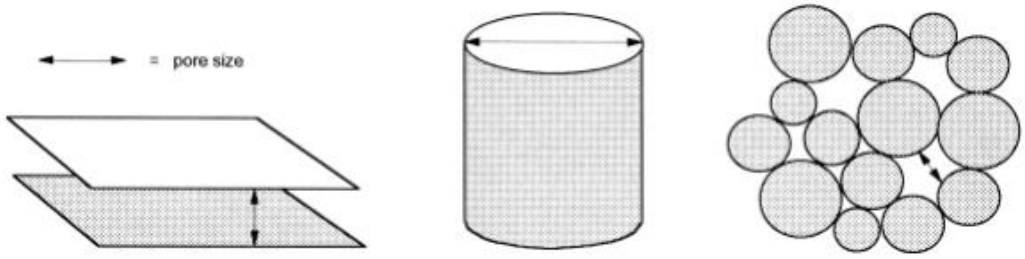

Figure 6. (a).Slits: size distance between walls (b).Cylinders: size diameter (c).Voids between connected solids: size of void [43]

Several studies suggested that the contribution of the micropores in the EDL capacitance is higher than other pore in various sizes as the bare ions size of the electrolyte is near to the size of micropores. Therefore, micropores contribute more effectively for the EDL capacitance [41]. A study by Chmiola et al. [44] suggested

that accessibility of ions in the electrolyte into micropores was enhanced by the partial desolvation of the ions in the electrolyte when quaternary ammonium ion was used as the electrolyte. Since the gravimetric capacitance depends of the electrolyte, cell assembling technique and etc. , the gravimetric capacitance was not high on all microporous carbon [35–37].

Though microporous electrodes with high specific surface area are supposed to deliver greater electrochemical double layer capacitance, always the microporous have been considered not to make a considerable impact to the electrochemical double layer capacitance. Because, if the size of solvated electrolyte ions is larger than the pore size of the electrodes, these ions cannot access into the electrode for contribute to EDL formation. It is considered that mesoporous carbons whose mean pore size is from 2 nm to 50 nm have an perfect configuration as EDLC electrodes [44].

Creating a carbon electrode which is having a higher gravimetric capacitance EDLC involves awareness of the pore size distribution and the pore shape rather than only knowing the average pore size. This research investigate the connection between pore structures and EDL capacitances to explain the porous structures accomplishing very high EDL capacitance because porous structure seems to be more dominant factor than others [8].

EDLCs normally have best electrochemical performances when size of electrolyte ions is similar with pore size in electrodes, this enhances both capacitance and rate of performance. Therefore, to achieve an optimum capacitance, pore size of electrode and the selected electrolyte are the major parameters, which want to consider in simultaneously. With the type of selected electrolyte, the electrode pore size is superior to maintain about 0.2-0.5 nm and 0.8-1.3 nm for aqueous and organic electrolytes respectively [48]. According to Inchan Yang and group [49], mesoporous carbon is better than microporous carbon for organic electrolytes to optimize the capacitance.

Figure 7 illustrates the importance of the accessible area of the electrode material for the ion transferring. This figure shows the way of electrolyte ion adsorb onto the electrode material surface. As the Figure 7(a) ion adsorption occurs only at the surface of the electrode film because of its density packed morphology. Figure 7(b) illustrates

the effective adsorption of the electrode material because of its less dense corrugated three-dimensional morphology.

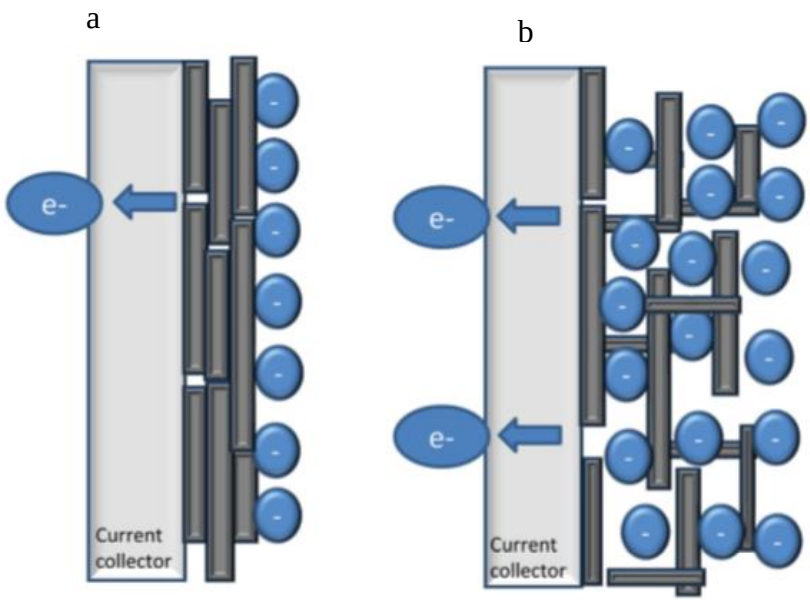

Figure 7. Schematic representation of the electrolyte ions penetrate onto the accessible surface of the porous electrode (a) Electrolyte ions adsorption onto densely packed morphology, (b) Electrolyte ions penetration through less dense porous morphology [50]

Surface Chemistry

Functional groups such as oxygen, nitrogen, hydroxyl, phosphorus, and epoxy are the common types of functional sites on some electrode materials [51]. Though most of oxygen, phosphorous and nitrogen containing groups improve the electrode-electrolyte interactions by increasing the wettability, some types of these functional groups result in the effect of pseudocapacitance. Specially, pyridinic and pyrrolic nitrogen groups increase pseudocapacitance, however, quaternary nitrogen groups increase the conductivity [52]. The molecular dynamic simulations predicted that hydroxyl groups can decrease the integral capacitance and the effect of the epoxy groups are comparatively less important. As these oxygen containing functional groups affects to decrease the capacitance at higher power densities, rate capability is increased by the surface chlorination [53]. And also previous studies on graphene has found that the doping of foreign atoms in to the honeycomb lattice as a simplistic way to modify its band gap [54].

2.4.2. Electrode material selection

Electrodes from graphene and its derivatives have attracted much attention in EDLCs. Graphene is a one-atom thick carbon-based material, which is a two-dimensional crystal which consists of sp^2 hybridized carbon atoms.

Graphene has much higher theoretical specific surface area (SSA) around 2630 m^2/g and, it can achieve the capacitance up to 550 F/g when its SSA is completely utilized. Graphene surface functional groups have significant impact on the specific capacitance. However, some functional groups may contribute more than others to the specific capacitance. As a general trend, the existence of the functional groups reduces the capacitance. Therefore graphene oxide (GO) has lower capacitance than its reduced version of graphene [17].

Graphene is a promising material in developing EDLC electrodes with low thickness and high conductivity, very low electrical resistivity [26]. Table I illustrates the physical properties of graphene.

Though graphene has high theoretical specific surface area, practically attaining this value is a challenge due to its tendency of layer restacking or agglomeration. To reach this theoretical value, heteroatom doping, and construction of three-dimensional frameworks can be identified as successful approaches. Doping with heteroatoms is a promising approach, and Having a similar atomic radius and electron number to carbon, nitrogen plays a major role as a dopant [16].

Several derivatives of graphene have been studied for EDLC electrodes, including holey graphene [15, 58], graphene oxide [59], graphene nanoribbons [60], graphene aerogel [41], graphene nanosheet [52], graphene hydrogel [61] and reduced graphene oxide (rGO) [62]. Graphene related electrodes have been tremendously investigated, which has shown a relatively high capacitance value than other carbon derivatives.

Table I. Physical properties of graphene

Property	Estimated value	Remarks
Tensile strength(E)	1.01TPa	-
Ultimate strength (σ)	130GPa	-
Absorbency	2.3% light	Completely transparent
Specific surface area	2630 m^2 g^{-1}	-
Thermal conductivity	5300 W m^{-1} K^{-1}	>carbon nanotube and diamond
Electron mobility	15,000$cm^2V^{-1}S^{-1}$at room temperature	>carbon nanotubes or silicon crystal
Electrical resistivity	10−6 Ωcm (lowest resistivity material in the world)	<copper or silver
electrical conductivity	1738 siemens/m	-
Ease of functionalization	π – π stacking interaction/ Electrostatic interaction	-

Source: [50–52]

The capacitance is varied significantly according to the type of carbon material. Zhu et al. [30] achieved capacitance of 316 F/g at a current rate of 1 A/g for a N-doped porous carbon with nanofiber electrode. He et al. [48] attained a capacitance around 233 F/g at a current density of 0.5 A/g for an electrode in the type of ordered mesoporous carbon (CMK-3) which was produced by magnetic blending and ultrasonic activation. By doing a steam-pretreatment for activated carbon, Li and co-workers [12] employed a capacitance about 155.16 F/g at a current rate of 0.5 A/g; however this capacitance value is a comparatively lower than other graphene-based carbon electrodes.

Under graphene based materials, heteroatoms doping shows a comparatively higher capacitance values. Kumar et al. [54] explored nitrogen-doped graphene using NH_4OH and it had a capacitance of 457 F/g at a current density of 1m A/cm which is near to the theoretical value. Another study was conducted by Gopalsamy et al. [35]

which followed a co-doping process using graphene nanoribbons, where co-doping was done using nitrogen and sulfur and they achieved a specific capacitance about 442 F/g at a current density of 0.5 A/g. By the deposition of graphene aerogel onto nickel form by Ye et al. [63] reached a capacitance of 366 F/g at a current density of 2 A/g. Another successful approaches were taken by Jiang et al. [16] and Sun et al. [52] by nitrogen doped porous carbon with nanofiber and nitrogen doped graphene using GO and urea which results nitrogen doped graphene nanosheets respectively. They achieved comparatively high capacitance values of 316 F/g at a current density of 1 A/g and 326 F/g at a current density of 0.2 A/g correspondingly.

KOH activation is a promising method to prepare an electrode material with high surface area and to attain high capacitance. Bo Zeng and his group [64] have synthesized KOH-activated nitrogen-doped graphene nanosheets (aNG) using thermal annealing method. According to their results, the electrochemical findings exhibit that a capacitance of 132.4 F/g at a charge/discharge current density of 0.1 A/g is achieved for KOH-activated nitrogen-doped graphene which is approximately five times higher than that without KOH activation. It implies the impact of the KOH activation on the electrochemical performances. And K.Kierzek et al. [65] showed very promising capacitance values, ranging from 200 to 320 F/g to the KOH activated various coal and pitch-derived carbonaceous materials. KOH activation has been done for microwave exfoliated graphite oxide (MEGO) by Shuilin Wu and his group [66] and obtained a specific capacitance of 265 F/g (185 F cm^{-3}) at a current density of 1 A/g in 6 M KOH electrolyte, which remained 223 F/g (156 F cm^{-3}) at the current density of 10 A/g. Therefore, above literatures show that the variation of electrode performances based on the type of graphene-based material and the influence of KOH activation on the higher capacitance

Increasing the areal loading (thickness) of a film tends to the reduction of its gravimetric capacitance. It has been proved for rGO film, the capacitance for thick films was about 135 F/g and this value could be increased up to 290 F/g by using its thinner films, where the thickness was measured in terms of area loading and 0.45 mg/cm^2 was their optimum value.[67].

Figure 8 is a summary of several graphene-based electrode material preparation routes, which have obtained specific capacitance value higher than 200 F/g. Since the easiness, high yield, higher level of exfoliation and environment friendliness, chemical vapour deposition (CVD) and Hummer's method are the most commonly-used methods for graphene synthesis among various top-down and bottom-up processes [6 ,11] . CVD is a bottom-up synthesis process and it requires more energy to produce the precursor which is the gaseous state of the process molecule [68]. High heat requirement and small production scale are the drawbacks of CVD. Therefore, Hummer's method becomes feasible due to low energy requirement, low cost and ability to large-scale production [69]. More research has been focused on modified Hummer's method to synthesis of graphene oxide and then they have followed various approaches to alter the surface properties to enhance the electrode performances. Surface modification of prepared graphene oxide is the most intriguing step in the electrode preparation. Template methods, graphene based composite preparation and heteroatom doping are the common surface modification methods. Among these methods, heteroatom doping, especially nitrogen atom doping can be identified as the most effective graphene oxide modification method because it enhances the electrode wettability and prevents the GO layer restacking. However chemical reduction by KOH also can be identified as a common method because it gives mesoporous structure.

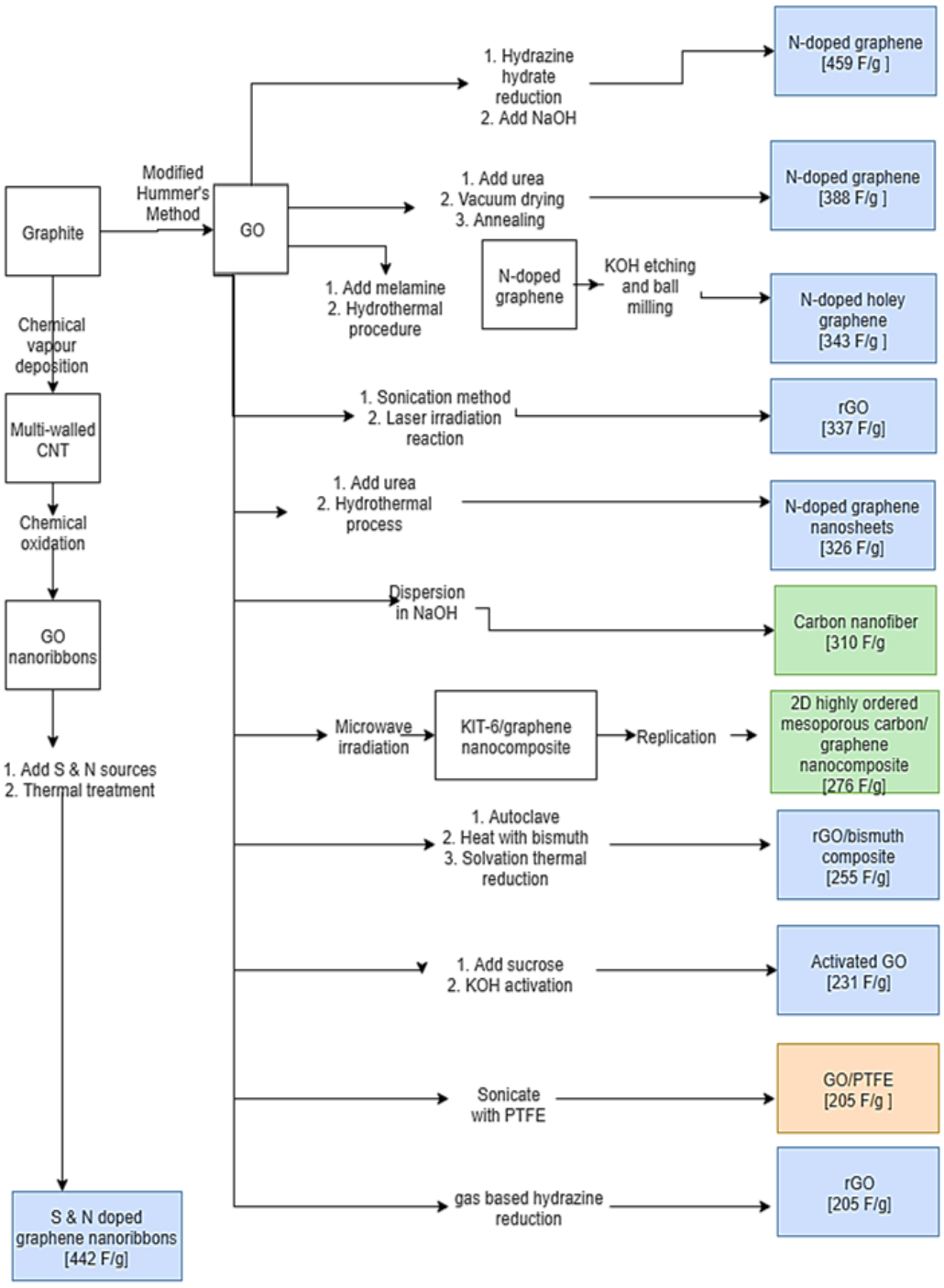

Figure 8. Preparation methods of graphene-based electrode materials

2.4.3. Synthesis routes for preparation of graphene from graphite

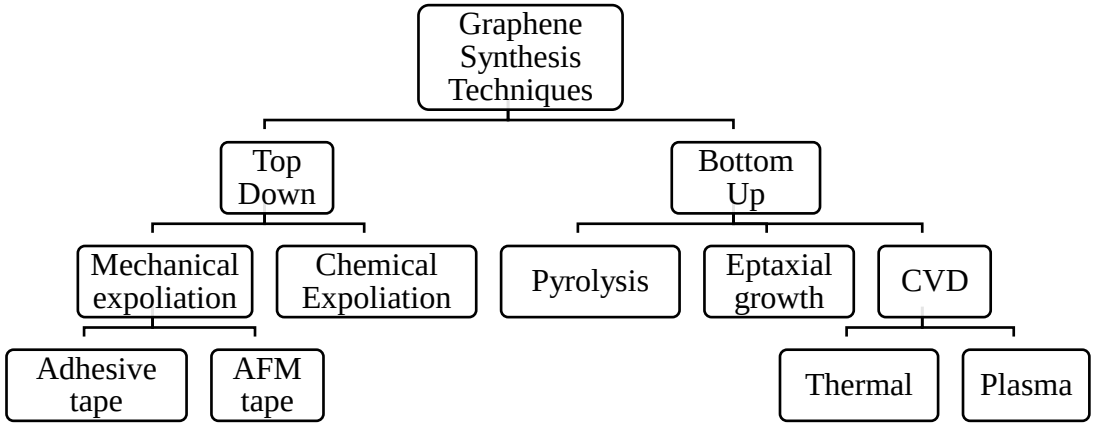

Figure 9. A flow chart of graphene synthesis processes[68]

Figure 9 illustrates the several graphene syntheses routes by the top-down and bottom-up approaches. Mechanical exfoliation is the rarest and less effective procedure used for isolating single layer graphene sheets from desired source. This method can be identified as the first-established procedure for graphene synthesis [68]. In this exfoliation method, longitudinal or transverse stress is exerted on the graphite surface for the exfoliation [68,69,67].

Chemical exfoliation is a feasible method for the synthesis of graphene [73]. Chemical exfoliation methods produce colloidal suspension of graphene from graphite and graphite intercalation compounds. This is a combined process which has two steps. In the first step, the Van der Waals forces which are in between layers (interlayer forces) are lessened by chemical interactions to widening the distance between layers. Therefore, it produces graphene- intercalated compounds [74]. Finally, it exfoliates to graphene which has single to few layers by sonication or by the rapid heating. Hummer's method is the most widely used chemical exfoliation process [69].

Chemical synthesis is a successful approach to produce graphene. Sonication and GO reduction are the two methods in chemical synthesis. A conventional procedure of the

preparation of graphene in larger quantities is the chemical reduction [75]. GO is mostly synthesized by the oxidation of graphite using some oxidants based on chemical exfoliation method. Then graphene is produced by sonication or reduction process of GO. Sonication and reduction of GO are another famous approach to the graphene production. Some reducing agents are phenyl hydrazine, hydroxylamine, glucose, ascorbic acid, and hydroquinone [74].

Pyrolysis is a bottom-up approached used for graphene synthesis. This is a thermal reduction of graphite with sodium ethoxide under sonication. In this process, graphene sheets are smoothly detached [74]. Epitaxial graphene production is a thermal graphitization process using SiC surface; has the limitations in higher temperature requirement and the failure to transfer on to another substrates [76].

CVD involves a chemical reaction process where the gaseous state of the precursor is prepared by heating. At a higher temperature, a substrate like a solid, a film, or liquid is diffused on thermally disintegrated precursors. Finally, the deposition is taken place from the gaseous precursors on the surface of the substrate such as Ni, Pd, Ru, Ir and Cu. Therefore, thermal CVD techniques are highly beneficial for large-area device manufacture and advantageous in upcoming corresponding metal- oxide semiconductor (CMOS) technology by substituting Si [76].

Among these methods, chemical exfoliation method consists of low energy consuming process and low environmental impacts comparative to other graphene synthesis methods. Because bottom-up processes need large amount of energy, and they need modified atmospheric conditions. Therefore, modified Hummer's method is selected under chemical exfoliation method as the GO synthesis method in this research.

Hummer's Method

Sulfuric acid and potassium permanganate are used in this method. Even though potassium permanganate is a common oxidizing agent, the real oxidizer in this process is dimanganese heptoxide (Mn_2O_7).

$$KMnO_4 + 3H_2SO_4 \rightarrow K^+ + MnO_3^+ + H_3O^+ + 3HSO_4 \quad (1)$$

$MnO_3^+ + MnO_4^+ \rightarrow Mn_2O_7$ (2)

Graphite flake is a naturally occurring mineral, which consist of some impurities and some purification processes are needed to remove the undesired atoms. Many defects in its π structure can be occurred during this purification process, and these defects can initiate the oxidation process.

Graphite sheets have sp^2 hybridized structure and this structure is destroyed, and wrinkled defects are formed when it is oxidized to produce GO. The interlayer distance is increased due to the formation of defects and the average interlayer distances of graphite powder and GO are 3.35 Å and 6.8 Å respectively. The interlayer distance is depended on the exfoliation level and the amount of intercalated water which are in between sheets. Therefore, single-layer GO can be produced from GO by low-energy ultrasonication in water. GO has a hydrophilic surface and it is negatively charged due to oxygen-containing functional groups.

2.4.4. Tailoring pore structure

Template methods and chemical activation are the dominant methods of pore structure tailoring. In template method, pre-designed silica templates are commonly used, and it gives a well-controlled pore arrangement. However, cost of the templates and their unavailability are the main drawbacks of these methods. Since the easiness and the having a mesoporous structure of the product, KOH activation method is the most promising method in chemical activation. A homogeneous contact between the KOH and the solid graphene sheets can be created after drying with the colloid with injected KOH. And chemical activation in annealing of graphene with KOH leads to a ultra-high specific surface area with a mesopore structure [15, 41, 57, 79].

2.4.5. Tailoring surface chemistry

Surface chemistry is another important characteristic of electrode material apart from conductivity and pore structure. Functional groups, defects, dopants, and heteroatoms on surface are addressed under the surface chemistry. The incorporation of heteroatoms, such as nitrogen, into carbon materials can considerably improve the specific capacitance, because the nitrogen-containing functional groups can induce pseudocapacitive effects and improve the wettability of carbon materials to electrolyte

solution [77]. Therefore, wettability is the main factor which effects on the pseudocapacitance [77].

Oxygen-containing functional groups are the major factor which effects on the wettability [78]. Especially, hydrophilic oxygen-containing functional groups, such as carboxyl, hydroxyl, and carbonyl reduce the wettability due to these oxygen-containing functional groups have an excellent affinity toward water droplets [77, 78], . The understanding about the wetting properties of graphene in water is important to design a graphene-based energy storage device in microstructural aspect and to improve the performances. Increasing the wettability and avoiding from pseudocapacitance can be achieved by modifying the surface chemistry accordingly. GO reduction is a dominant process for tailor the surface chemistry.

The reduction step can also be completed through several methods, such as the environmentally methods of flash photoreduction, hydrothermal, catalytic reduction and thermal annealing [79–81]. Slow thermal annealing and chemical methods are used to achieve the complete reduction of the functional groups. Thermal annealing normally operate in a modified atmosphere which prevents the oxidation, however it can be also locally induced in air by scanning a heated AFM (Atomic Force Microscopy) tip around the surface of the GO [82]. Sodium borohydride, ascorbic acid [83], baker's yeast with hydrazine hydrate are the frequently used reducing agents [81, 83]. An exfoliated material having a higher BET (Brunauer, Emmett and Teller) can be obtained from the combination of both thermal and chemical reduction methods of GO. Because the surface area is useful in electronic and energy storage applications.

Generally, thermal reduction of GO gives comparatively higher surface area values than the chemical reduction of GO as GO tends more to remove its functional groups under high temperature condition [81, 82, 84, 85]. For the energy storage purpose, specific surface area are critical parameters. Therefore, thermal reduction method can be selected because it produces high surface area and homogeneous structure, thus enabling the functions of graphene-based materials for large-scale products.

2.4.6. KOH activation mechanism

Mechanism of KOH activation

Activation of graphene oxide (GO) from KOH starts in a solid-solid reaction and it converts to a set of solid-liquid reactions [87]. These solid-liquid reactions are involved in the reduction of potassium compounds to form metallic potassium, carbon oxidation and production of various active intermediates.

KOH dehydrates to form K_2O at 400℃ (Eqn.3). Three consecutive reactions happen to the production of K_2CO_3. H_2O consumes carbon and form CO (Eqn.4). Then CO reacts with H_2O to form CO_2 (Eqn.5). K_2CO_3 is formed as the result of the reaction between CO_2 and K_2O (Eqn.6). K_2CO_3 forms at above 400℃. Although KOH is completely decomposed at about 600 ^{0}C.

The prominent reaction between C and KOH is previously reported as Eqn.7 [33]. The standard Gibbs free energy (ΔG^0) of this reaction which is illustrated in Eqn.7 is positive at ambient temperature and it has a negative value when the temperature is increased upto 570 ℃. Due to the dilution of the solution with the inert gas flow, the partial pressure of H_2 is less than the ambient pressure. Therefore ΔG^0 becomes negative at a temperature below 570℃. Though the Eqn.7 is the prominent reaction, there are several reactions happen to consume carbon.

$$2KOH \rightarrow K_2O + H_2O \quad (3)$$

$$C + H_2O \rightarrow CO + H_2 \quad (4)$$

$$CO + H_2O \rightarrow CO_2 + H_2 \quad (5)$$

$$CO_2 + K_2O \rightarrow K_2CO_3 \quad (6)$$

$$6KOH + 2C \rightarrow 2K + 3H_2 + 2K_2CO_3 \quad (7)\ (400℃)$$

According to the Eqn.8, K_2CO_3 significantly decomposes to K_2O and CO_2 at higher temperatures above 700℃and K_2CO_3 completely disappears by the total decomposition at about 800℃. According to the Eqn.9, K_2CO_3 consumes carbon about 493^{o}C to produce metallic K. However, K_2O and CO_2 consume carbon at high temperatures above 700℃as the Eqn.10 and 11.

$K_2CO_3 \rightarrow K_2O + CO_2$ (8) (Above 700℃)

$K_2CO_3 + C \rightarrow K + CO$ (9) (Above 493℃)

$K_2O + C \rightarrow K + CO$ (10) (Above 700℃)

$CO_2 + C \rightarrow CO$ (11) (Above 700℃)

KOH activation process consists of both chemical and physical activation mechanisms, and it can be divided into four main stages. These stages are (i) etching the carbon framework (chemical activation), (ii) gasification of carbon (physical activation), (iii) K intercalation and (iv) removal of intercalated metallic K. Porous network generation starts from the chemical activation which involves to the redox reactions between various potassium compounds with carbon (Eqn.7, Eqn.9 and Eqn.10). Further development of the porosity takes place under the physical activation, which results in formation of H_2O and CO_2 (Eqn.3, Eqn.5 and Eqn.8). According to the Eqn.7 and Eqn.8, metallic potassium is formed, and it is intercalated to the GO lattice, as it is formed which causes in significant expansion of the GO lattice. Finally, the intercalated metallic potassium and other remaining potassium compounds are removed by washing by HCl and distilled water. After the washing process the formed porous carbon lattice stays at its expanded structure [88].

Critical process parameters of KOH activation

Development of porous carbon structures using KOH activation has been reported by many authors. In the previous studies, that KOH activation has been carried out for both natural carbon sources, and also modified carbonaceous materials such as graphene, expanded graphite etc. [81–84]. Most studies were focused on the identification of favorable ranges of critical process parameters in KOH activation by varying one or more parameters. KOH/C ratio, activation temperature, activation time, the temperature increasing rate and sweep gas rate can be identified as the critical parameters that influence the porosity and surface area of the activated material.

Influence of activation temperature

Activation temperature above 800℃ is commonly used, in order to surpass the complete decomposition temperature of K_2CO_3 to confirm the supply of sufficient

energy to produce metallic K for the optimum activation. However, activation at low temperatures around 600℃ have also been reported [6,12]. However, activation at lower temperatures generally results in lower specific surface area [66]. Min Li and his co-workers [91] followed KOH activation of carbon spheres from glucose, which resulted in specific surface area about 1282.8 m^2/g at an activation temperature of 600℃. However, the average pore size obtained was about 250 nm, which is not adequate for the effective electrolyte ion penetration. Therefore, previous studies suggest that an activation temperature above 800℃ can result in higher specific surface area, together with favorable pore size distribution [86, 88].

Influence of the duration of activation

Xiaoyu Gao et al. [92] synthesized a graphite-based electrode material for lithium-ion capacitor by twice KOH activation of Sri Lankan vein graphite without any prior modification. In this study, the KOH/C ratio was maintained at 4, and activation was carried out for 1h duration at 800℃ followed by a second activation step for 1h duration at 950℃. During this activation process, the SSA of vein graphite was increased from 326 m^2/g to 1857 m^2/g. They have used higher activation duration when compared to other similar studies which used same KOH/C ratio and activation temperature, and it has resulted in comparatively high specific surface area.

Though most of the reported KOH activations were carried out for 1 h duration, limited number of studies have used 2 -5 h duration and achieved extraordinary SSAs. For example, Pitch- derived carbonaceous was successfully activated by Min Zhou and co-workers [77] (ratio of KOH/C as 1 at the activation temperature 700℃), and a 2-hour activation process has improved the SSA to 3200 m^2/g from 521 m^2/g.

K. Kierzeka et al.[65] activated carbonaceous precursors with KOH in 1:4 ratio at 800 ℃ for 5h duration and obtained high SSA about 3200 m^2/g. Therefore, it is evident that longer activation duration at high activation temperature results in higher SSA and smaller pore sizes about 1.79-2.21 nm. Their obtained pore size is in the range of expected pore size (0.7-3 nm) for the best performance in electrolyte ion penetration. Some studies were used the KOH/C mass ration in 4 and temperature at 800℃, but

they couldn't maintain the material porosity in this range. These experiments illustrate the effect of activation duration for the SSA modification.

Influence of minor parameters

The influence of the heating method in KOH activation was studied by Yongbin Ji and his group [9], comparing the SSA from both microwave heating and electrical furnace heating of the mixture of KOH and commercial coal-tar pitch. According to their results, microwave heating had been given better SSA than electrical furnace heating. The reason is that the creation of mesopores in microwave heating is related to the fast heating with compared to slow electric furnace heating. Though, Yongbin Ji and his group suggested the microwave heating as the best heating method for the KOH activation, considering other literature influence of the heating method can be neglected with the prioritizing other key parameters.

Despite the main three parameters (activation temperature, activation time and KOH/C ratio), studying the effect of the other minor variables such as nature of the sweep gas and its flow rate [87], pH of the activation environment [93] and furnace temperature increasing rate are important. The sweep gas should be an inert gas. And the maintaining of sweep gas flow rate at a low value is important for give sufficient time to occur the reactions in between liquid and gas phases. This rate is maintained by measuring the exhaust gas flow rate at one air bubble per second. Various amounts of KOH are added with graphene oxide in the activation process. This varies the pH of the activation environment. Maintaining the sample pH can be done after finding the optimum KOH/C mass ratio for the activation process. Therefore, understanding of the KOH activation mechanism is important to have a great awareness about the influence of these parameters.

2.5. Electrolyte

Figure 10 shows the impacts of the electrolyte on the energy storage capability. Mainly it alters the power density, capacitance, cycle life, energy density and thermal stability of the EDLC. Therefore, the proper selection of the electrolyte is significant for the electrode cell fabrication. The achievable cell voltage of a supercapacitor differs with the breakdown voltage of the electrolyte; therefore, the energy density of the cell is

controlled by the electrolyte rather than depending on the voltage. Electrolyte conductivity is a very important factor which should be concern when selecting the electrolyte, because it differs the cell's electric serial resistance which directly alter the power density [26]. Normally electrolytes are in liquid phase, and it conduct electricity through conveying ions and maintain an electronic insulation among positive and negative electrodes [94].

The choice of the electrolyte directly affects the capacitance, power density, cycle life, energy density, thermal stability, and equivalent series resistance of electrochemical capacitors. Compatibility with the electrode material is an imperative factor when selecting an electrolyte. Because the electrolyte should not tend to change the surface chemistry of the electrode and not react with it or dissolve any component in the electrode.

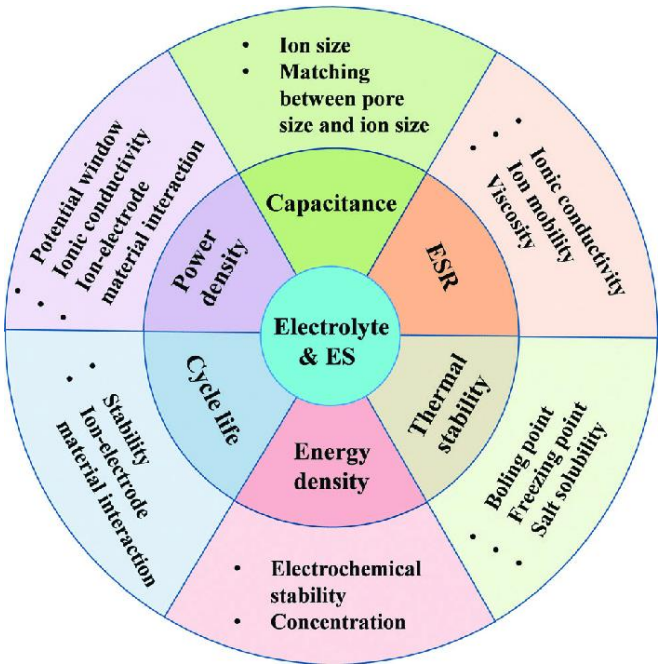

Figure 10. Effects of the electrolyte on the energy storage performance [95]

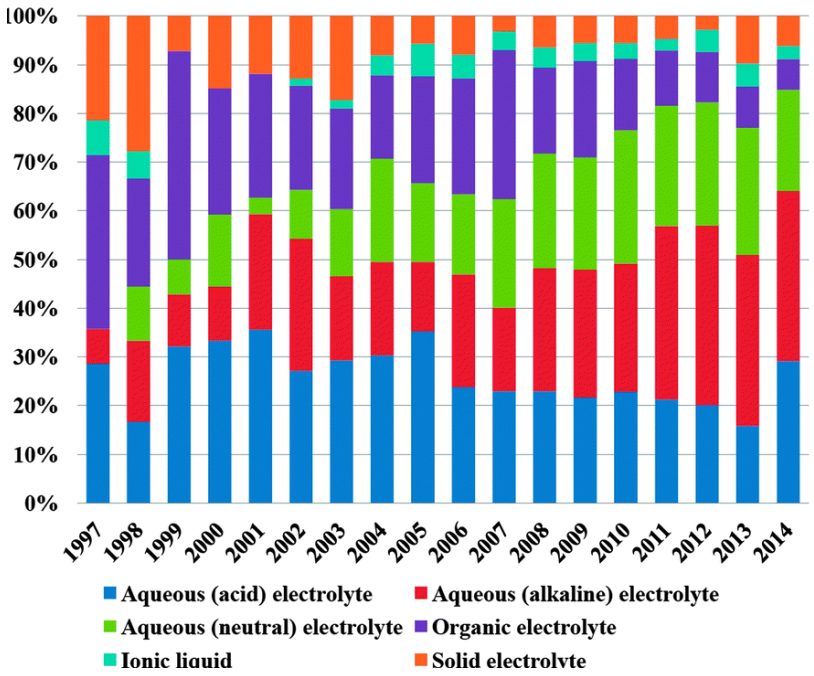

Figure 11. Percentage of different electrolytes used for the electrochemical supercapacitors. Source: Web of Science [96]

2.5.1. Aqueous electrolytes

Owing the narrow voltage window of the aqueous electrolytes, it has low attention in the commercial energy storage applications. This may be the major reasons to the more commercial energy storage applications use organic electrolytes. However, according to Figure 11, aqueous electrolytes were the widely used electrolyte in research sector.

Typically, aqueous electrolytes show higher conductivity (as 0.8 S cm^{-2} for 1 M H_2SO_4 at 25℃), which is at higher than electrolytes such as ionic and organic electrolytes. This characteristic is favorable for reduce the ESR for a better power delivery. The bare size, hydrated anions and cations and their mobility are the parameters of electrolyte, which effect on the ionic conductivity and also on the specific capacitance.

The aqueous electrolytes have three groups as acid (H_2SO_4), alkaline (KOH, LiOH, NaOH), and neutral solutions (Na_2SO_4, NaCl, KCl, $MgSO_4$, $LiSO_4$,). Among these aqueous electrolytes H_2SO_4, KOH and Na_2SO_4 are the widely used electrolytes. Since water decomposition, it has a lower potential window (1V-1.3V), which is a major drawback in electrolyte performances.

Acidic electrolytes are the widely used electrolyte in research and H_2SO_4 is the mostly used acid electrolyte owing its higher ionic conductivity (0.8 S cm^{-1} for 1 M H_2SO_4 at 25℃). Because of the strong dependence of the ionic conductivity on the H_2SO_4 concentration, optimum concentrations in various temperatures have been studied. Majority of the researches used 1M concentration as the optimum value [87,88,10]. The maximum potential window which was achieved using 1 M H_2SO_4 is 1V and the specific capacitance values are varied between 100 -460 F/g. organic electrolytes could maintain much potential windows than acid electrolytes as well as the specific capacitance values are significantly high [11,16,44,60,89,90].

However, the energy densities and the specific capacitance values are similar for both KOH and H_2SO_4 electrolytes [28,48,77,84, 91].

2.5.2. Organic electrolytes

Organic electrolytes have a higher potential window at 2.5 V to 3 V. Therefore, most of the commercial applications tends to select a suitable organic substrate as the electrolyte for their EDLC preparation. Since the energy density and power density of EDLC are directly dependent on the cell voltage, organic electrolytes can give increased both power and energy densities. Moreover, organic electrolytes allow to select a low-cost material as Al for the current collectors and as the packaging materials. Conventional EDLCs which uses organic electrolytes use some conductive salts (e.g., tetraethylammonium tetrafluoroborate ($TEABF_4$) liquified in PC (propylene carbonate) solvent [11,16,44,60,89,90]. Among the organic electrolytes, gel electrolytes which made from the combination of polyvinyl alcohol (PVA), acid/base and/or carbon source shows low potential window compared to acetonitrile basis electrolytes [11,89].

2.5.3. Ionic liquid (IL) electrolytes

The pure liquid salts can be labeled as Ionic liquids (ILs). Since having a practically zero or negligible volatility, broad operating voltage window, highly ionized nature, and behaving as a liquid for wide temperature range, ILs are used in more electrochemical energy storage devices as the best performing electrolyte [86,92].

N-butyl-N-methylpyrrolidinium (trifluromethanesulfonyl) imide ($PYR_{14}TFSI$) is a common type of ionic electrolyte, which use with blend with propylene carbonate. This electrolyte increases the energy storage of the EDLC but its high viscosity limits power density [107].

As the conclusion of selecting the best type of electrolyte, though aqueous electrolytes have been become a prominent group because of high ionic conductivity, functioning safety, because of maximum charging voltage is limited by splitting voltage of water, research have moved toward the organic electrolytes. However traditional organic electrolytes have difficulties in some maintenance, high cost, high environmental influence, safety matters and low ionic conductivity, ionic liquids (IL) have more attention today in view of voltage window, conductivity, viscosity, boiling/ melting points, dielectric constant, salt chemistry of different liquid solutions. However, research still research finding new electrolytes to accomplish estimated values.

2.6. Sri Lankan vein graphite

Natural and synthetic graphite are the sources for graphene synthesis. However, graphite flakes are the mostly used carbon source for the graphene synthesis in industrial and lab scale [15,42,44,56,96,99,103,104]. Sri Lankan graphite veins are unique because of its high purity, high crystallinity and the large scale of their occurrence. Because of its unique properties, large number of studies has been done for find its formation [18,19], trace elements [20,21], thermal and chemical behavior [114] and surface modification methods [23,24]. Capability of increasing the electrochemical interaction by simple mechanical or chemical processes is a main finding about vein graphite which is beneficial for use in this research [25,26].

Though more research has been done with Sri Lankan vein graphite, no one have successfully attained to vein graphite for EDLC applications. Therefore, the unique properties of Sri Lankan vein graphite are considerable for the EDLC electrode preparation.

2.7. National Relevance

As the only country to export commercial quantities of Vein graphite, Sri Lanka recognizes the mineral's value in creating significant foreign investment from both local and foreign private sectors. High purity vein graphite is available in Sri Lanka. It has an extremely high grade with over 90% carbon. Vein graphite is today in demand for numerous industries owing to its composition. The unique properties including chemical inertness, high density, lubricating properties, high electrical and thermal conductivity, resistance to oxidation and crystalline perfection that vein graphite has proven to be precious to industrial applications.

Sri Lankan vein graphite has unique properties, which could have a high commercial value in energy storage sector. Therefore, innovations are essential for the value addition of Sri Lankan graphite for the applications in energy storage devices. It is a national need to build Sri Lanka's capabilities in energy storage solutions through research and development.

Various categories of graphene-based materials have been studied to use in the EDLCs. However, higher energy and time consumption, environment pollution and requirement of more additives when assembling the cell are the drawbacks in reported studies. Therefore, it is needed to create simple and greener ways to attain high functioning and cost-effective electrodes using high quality Sri Lankan vein graphite.

3. RESEARCH METHODOLOGY

3.1. Materials

Sri Lankan vein graphite was received from Bogala graphite mine, Sri Lanka. Other chemicals such as H_2SO_4, $KMnO_4$, H_2O_2, H_3PO_4, HCl, ethanol and KOH, methylene blue, $Na_2S_2O_3$, iodine, starch were supplied by Breckland scientific chemical suppliers, UK. All chemicals were analytical grade and used as received without any further purification. All solutions which were used in the surface area analysis were freshly prepared with distilled water.

3.2. Graphene oxide (GO) Synthesis

GO was synthesized from Sri Lankan vein graphite by modified hummers method. A combination of vein graphite powder (10 g) and $KMnO_4$ (60 g) was added to a mixture of concentrated H_2SO_4/H_3PO_4 (1200:133 ml), stirring and keeping the temperature at between 10-20℃. Then the mixture was stirred while heating at 60℃ for 10 h. The reacted mixture was cooled down to room temperature and poured onto the ice cubes(~500ml) with 3 ml of 30% H_2O_2. The resulting precipitate was washed twice with distilled water, HCl, ethanol and again twice with distilled water by centrifuging at 4000 rpm for 20 min per each washing stage. The properly washed precipitate in neutral pH was called GO aqueous dispersion. This dispersion was freeze-dried, followed by freeze-drying at -45℃ under vacuum condition (0.6 bar) for 72 h.

3.3. Activation

GO was activated by following the KOH activation method. A mixture of GO powder and KOH was dissolved in 5 ml of ethanol. A thick paste of this mixture was prepared by heating below 60℃ with continuous stirring. The mass ratio of KOH: GO was varied at 1, 2, 3, 4, and 5. The resultant mixtures were carbonized at 700℃, 800℃ and 900℃ under an N_2 environment in a horizontal tube furnace. The activation time was varied to 50 min, 60 min, 70 min, and 90 min. The activated samples were cleaned from diluted HCl and distilled water until having a neutral pH of the filtrate. The properly cleaned samples were air-dried, and the final products were called as the activated GO (AGO). The activated samples are named as AGO(T)-m-t, where AGO means activated graphene oxide, “m” is the KOH/GO mass ratio and “t” is the activation time (min). For example, GO sample activated at 800℃ with KOH/GO

mass ratios at 4 for 60 min is noted as AGO(800)-4-60. This naming convention will be used in the discussion hereafter.

3.4. Morphology, composition, and structure characterization

For the morphological analysis, Scanning Electron Microscopy (SEM-ZEISS, EV018, Germany) was used. Elemental analysis was done using Energy Dispersive X-Ray analysis (EDX). The presence of functional groups was observed by the Fourier Transform Infrared (FTIR-Bruker, Alpha, Germany) facility. Furthermore, X-Ray Diffraction (XRD- Bruker, Alpha, Germany) was used to examine the crystallinity and the interlayer distance of prepared activated graphene.

3.5. Surface area analysis

As the main aim of this research is to prepare an ultra-high surface area electrode material for an EDLC, surface area analysis is done on all activated samples. The adsorption properties of methylene blue ($C_{16}H_{18}ClN_3S$) and iodine (I_2) were used as the primary indicators of the surface area analysis of these AGO. Calculated specific surface area was verified by Brunauer-Emmett-Teller (BET-gas sorption analyser Anton Paar, USA) test.

3.5.1. Determination of methylene blue number (MBN)

The methylene blue number is the maximum amount of dye, methylene blue (MB) adsorbed on 1.0 g of adsorbent (AGO). First, the UV-visible absorption spectra of MB were recorded by using a UV/Vis spectrophotometer in the 200–700 nm range. The maximum absorbance for MB was observed at the wavelength of 664 nm. Therefore, the calibration curve of MB dye was obtained at 664 nm.

AGO samples were dissolved for the preparation of 0.01 g/ml aqueous solutions. 1 ml of each solution was contacted with 9 ml of 50 ppm MB solution for 24 hours. Then the mixture was filtered. The filtrate was transferred to the UV/Vis spectrophotometer cuvette for absorbance determination at 664 nm. A distilled water sample was used as the reference.

The mass of MB dye adsorbed by each activated GO samples was calculated by the Eqn:12.

$$q_{eq} = (C_o - C_e) \times \frac{V}{M} \quad (12)$$

Where,

q_{eq}(mg/g): Mass of absorbed MB

C_o(mg/L) : Starting concentration of MB

C_e(mg/L): Equilibrium concentration of MB

V(L): Volume of the MB treated

M(g): Mass of the absorbent (GO)

Langmuir model was used to find the methylene blue number. For that, q_{eq} vs C_e plot was made, and Langmuir parameters (Q_{max} and K_l) were found by least square fitting regression.

3.5.2. Determination of iodine number (IN)

The iodine number is defined as the milligrams of iodine adsorbed by 1.0 g of carbon when the iodine concentration of the filtrate is 0.02 N (0.02 mol/L). The iodine number was determined according to the ASTM D4607-94 method.

3.5.2.1. Preparation of standard solutions

First, 5 % w/w HCl solution was prepared. Then, Sodium Thiosulfate (0.1 N) was prepared by following procedure. 24.8 g of sodium thiosulfate was dissolved in 100 ml of freshly boiled distilled water. Well dissolved solution was transferred to 1 L volumetric flask and diluted up to 1 L. The solution was stored in an amber bottle. This solution was allowed to stand at least 4 days before use.

Then, following procedure was used to prepare the standard Iodine Solution (0.001 N). 12.7 g of iodine and 19.100 g of potassium iodide (KI) were weighed into a beaker and were mixed properly. 50 ml of distilled water was added to the mixture and stirred. More water was continuously added and stirred until all crystals were thoroughly dissolved. It was transferred to a 1 L volumetric flask and filled to the mark with distilled water. Final solution was freshly stored in an amber bottle.

To make starch indicator, 1 g of starch was mixed with 10 mL of cold water to make a paste. This paste was diluted to 1 L while stirring and boiling for 5 min. This solution was freshly made before each titration.

3.5.2.2. Titration Procedure

Three appropriate amounts (0.01 g, 0.02 g, and 0.03 g) of AGO were weighed and noted the weights. Each weighted sample was transferred to a dry and clean 250 ml conical flask. 5ml of 5 w/w% HCl acid was pipetted onto the activated GO sample. The flask was swirled gently until the sample was completely wetted by HCl. This was boiled for 1 min to remove any sulfur contaminate on which might interfere with the titration findings. Then it was cooled to ambient temperature. 25 ml of 0.1 N iodine solution was pipetted into each flask. The solutions were shaken vigorously for 1 min and all mixture ware filtered quickly.

Then, 15 ml of each filtrate was collected to clean conical flask for the titration. Each filtrate was titrated with 0.1 N sodium thiosulfate solution until the solution was pale yellow. The 2 ml of freshly made starch indicator was added, and titration was continued with sodium thiosulfate until convert to a colorless. Volumes of sodium thiosulfate consumed for the titration were noted.

3.5.2.3. Calculation

Mass of I_2 added for the absorbance (A)

$$A = \frac{N_I \times V_I \times 126.93 \times 1000}{1000} \text{ mg} \quad (13)$$

$$A = N_I \times V_I \times 126$$

Where, N_I is the normality of the iodine solution (0.1 mol/L) and V_I is the volume of the iodine used (ml).

Mass of I_2 remained in the titrated volume (B)

$Na_2S_2O_3$ moles consumed for the titration $= \frac{N_S \times V_S}{1000}$ (14)

I_2 moles remained in the titrated volume $= \frac{N_S \times V_S}{1000} \times \frac{1}{2}$ (15)

$$B = \frac{N_s \times V_s}{1000} \times \frac{1}{2} \times 126.93 \times 2 \times 1000 \text{ mg} \quad (16)$$

$$B = N_s \times V_s \times 126.93 \text{ mg}$$

Where, N_S is the normality of the $Na_2S_2O_3$ solution (0.1 mol/L) and Vs is the volume of $Na_2S_2O_3$ consumed for the titration (ml).

Mass of I_2 remained in the filtrate

Total contacted volume=$V_H + V_I$ (17)

Therefore, Total mass of I_2 remained in the filtrate= $\frac{(V_H + V_I) \times B}{V_F}$ mg (18)

Let, $Dilution\ factor\ (DF) = \frac{V_H + V_I}{V_F}$ (19)

The mass of I_2 remained in the filtrate=$DF \times B$ (20)

Where, V_H is the volume of HCl used (ml), V_F is the volume of filtrate used for the titration (ml) and DF is the dilution factor.

Mass of iodine adsorbed

Mass of iodine absorbed=Mass of I_2 added for the absorbance – Mass of I_2 remained in the filtrate

Mass of iodine absorbed=$A - DF \times B$ (21)

Iodine absorbed per gram of activated GO= $\frac{A - (DF \times B)}{M}$ (22)

Where, M is the mass of activated GO used (g).

4. RESULTS AND DISCUSSION

4.1. Surface area analysis of porous graphene

Porous materials are beneficial in many a wide range of applications. Hence a comprehensive surface area analysis on specific surface area of porous materials is very important. The Brunauer-Emmett-Teller (BET) method can be used for accurate determination of specific surface area. However, due to high cost associated with BET equipment, it is not commonly available. Specially, it is not feasible to have this type of costly equipment in an industrial setting. Alternatively, surface area of porous materials can be determined by dye adsorption methods which is simple and economical. For the measurement of surface area of mesoporous graphene, methylene blue (MB) and iodine adsorption have been studied as suitable methods. However, it is important to study the dye adsorption kinetics related to particular application, to successfully use this for accurate determination of surface area.

According to the previous studies [1–3] the methylene blue (MB) and iodine numbers change proportionally with the surface area, making these mothods appropriate for determination of surface area. The methylene blue molecule has an area of 2.08 nm^2 and can only enter the large micropores and mesopores. The iodine molecule is relatively small with an area of 0.4 nm^2 and can enter into the smaller micropores [120]. Therefore, by determining both the MBN and the IN, a comprehensive surface area analysis can be done. Since the adsorption kinetics of MB molecules is specific to the type of porous material it is important to find the exact adsorption kinetic model for activated graphene oxide (AGO) synthesized in this study.

4.1.1. Kinetic Models

This section describes the identification of the best coordinated reaction order and the adsorption isotherm for the reaction between MB and AGO.

Initially, the full range of UV-Visible absorption spectrum of MB aqueous solution was obtained, (Figure 12(a)), and it showed the highest intensity absorbance peak at 664 nm. Therefore, 664 nm was used to measure the absorbance values in all samples. The absorbance values of the concentration known MB samples were measured to prepare the calibration curve. The calibration curve was obtained at 664 nm is shown in Figure 12(b) and this curve will be used for determining the concentration of MB

in the filtrates at different AGO samples. Figure 12(b) shows a plot of MB concentration versus spectrophotometer absorbance readings. Figure 12(b) confirms that the absorbance values are linearly proportional to MB concentration with a relationship of y=0.11092x (where y is absorbance and x is filtrate concentration) with R^2=0.98621.

In this study, AGO and MB were allowed to adsorb for 3 hours and, then the spectrophotometer reading was taken for the filtrate. The calibration curve was used to measure the filtrate MB concentration from the absorbance. Then, adsorbed methylene mass per one gram of AGO was calculated.

The spectrophotometry readings of the filtrates were taken and it was converted to the milligrams of MB adsorbed by 1 gram of GO at equilibrium (q_{eq}) and the adsorption quantity at any state from the calibration curve. High absorbance values of the filtrate indicate poor adsorption of MB onto the AGO surface. Therefore, the filtrate absorbance is inversely related to q_{eq} values.

Figure 13 depicts that the adsorption amount clearly correlated with the initial MB concentration. The amount of dye adsorbed per unit mass of adsorbent at equilibrium (q_{eq})values are gradually increased with the initial MB concentrations. It shows a MB absorption capacitance below 50 mg/g at the initial MB concentration of 1ppm and the capacitance has been increased to more than 150 mg/g after raising the initial MB concentration to 20 ppm. The q_{eq} gets higher probably due to an increase in driving force (concentration gradient) when the initial MB concentrations are increased. The diffusion of MB molecules onto the activated GO is definitely accelerated by the increase of the initial dye concentration of MB. At a lower concentration of MB dye, the driving force seems less to adsorb methylene blue. However, when the initial concentrations reach 5 ppm the q_{eq} values get increased at a higher rate of the gradient. At that point, the driving force may be sufficient enough to access most of the active sites of GO [118].

(a)

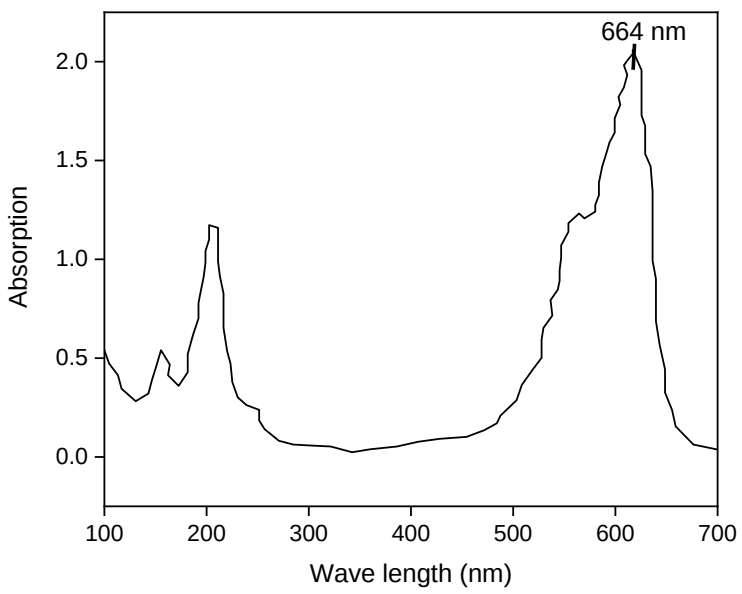

(b)

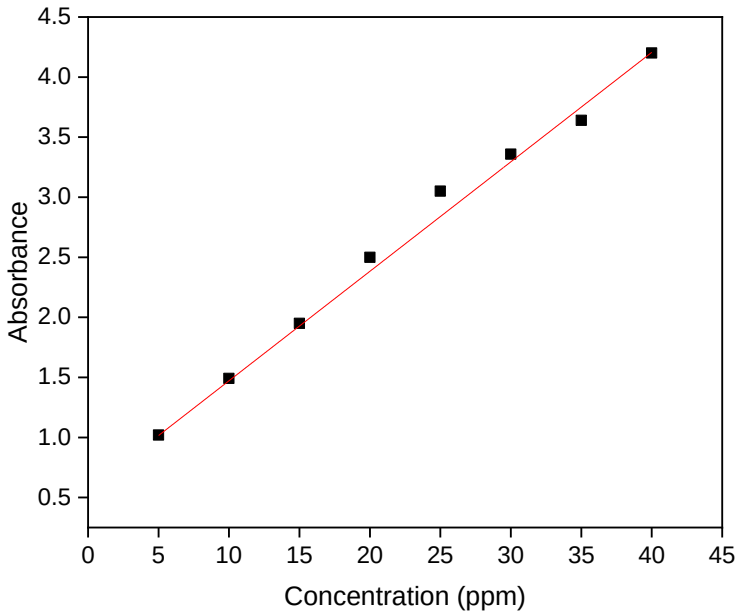

Figure 12: (a) The spectrophotometer absorption curve in whole wavelength, (b) The spectrophotometer calibration curve of MB at λ=664nm

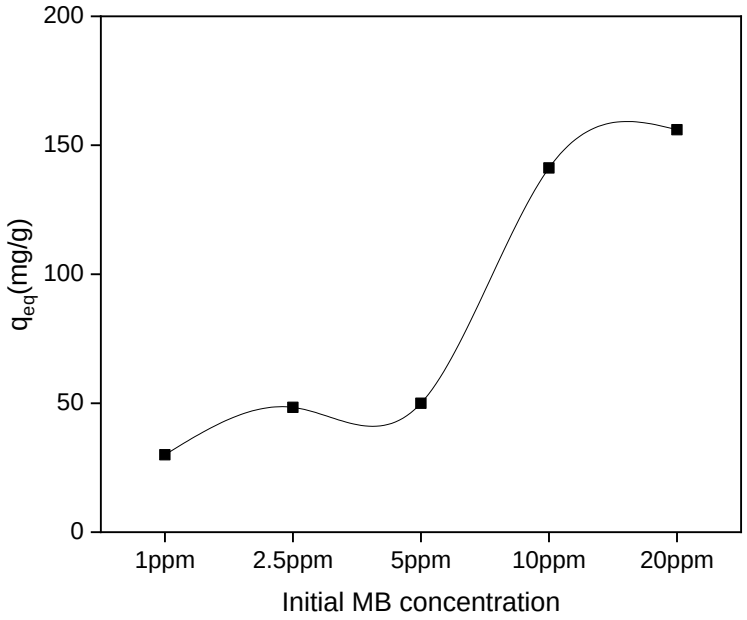

Figure 13: Effect of initial MB concentration on q_{eq}

Experimental values were fitted to the first order and second order kinetic models in order to investigate the adsorption process. The equations for the kinetic rates are as follows.

$$\frac{dq_t}{dt} = K_n(q_e - q_t)^n \quad (23)$$

Here q_e is the mass of dye (MB) adsorbed by unit mass of adsorbent (activated GO) in the units of mg g^{-1} at the equilibrium state where q_t corresponds to the mass of dye adsorbed by unit mass of adsorbent after time t. The rate constant (k_n) is n^{th} order adsorption (at n=1 unit is min−1 and at n = 2 unit is $gmg^{-1}min^{-1}$). The equations can be written in the linearized integrated forms as follows,

n=1; for the 1^{st} order kinetics:

$$\ln(q_e - q_t) = \ln q_e - k_1 t \quad (24)$$

n= 2; for the 2^{nd} order kinetics:

$$\frac{t}{q_t} = \frac{1}{k_2 q_e^2} + \frac{t}{q_e} \quad (25)$$

$\ln(q_e - q_t)$ vs t and t/q_t vs t graphs were plotted to calculate the rate constants and the coefficients of the 1st and 2nd order kinetic models. Based on the linear regression coefficient (R^2) and the q_e values which are calculated he best fitting kinetic model was chosen. Intraparticle diffusion model describes the dependency of reaction by diffusion. Hence, possibility of the diffusion to be the rate control step in this process can be investigated by using this model [118,119]. Here k_p is the inter particle diffusion rate constant. k_p is calculated from the gradient of linear part of the curve q_t against $t^{1/2}$.

$$q_t = k_p t^{1/2} + c \quad (26)$$

According to Figure 14, initially adsorption rate is high for the AGO samples and equilibrium is reached around 120 min. The availability of larger surface area and the external activation sites which can be reached fast by dye molecules have contributed to the fast adsorption rate of AGO. The efficiency of dye adsorption is also high in AGO because the single layered atomic structure facilitates the dye molecules to reach active sites. The saturation of dye adsorption occurs around 120 min. According to previously reported studies [120, 121], time taken to achieve equilibrium in MB adsorption in AGO may range upto several hours. However, in the present work, the adsorption of methylene blue onto the AGO was observed to be faster with equilibrium adsorption being achieved after 120 min.

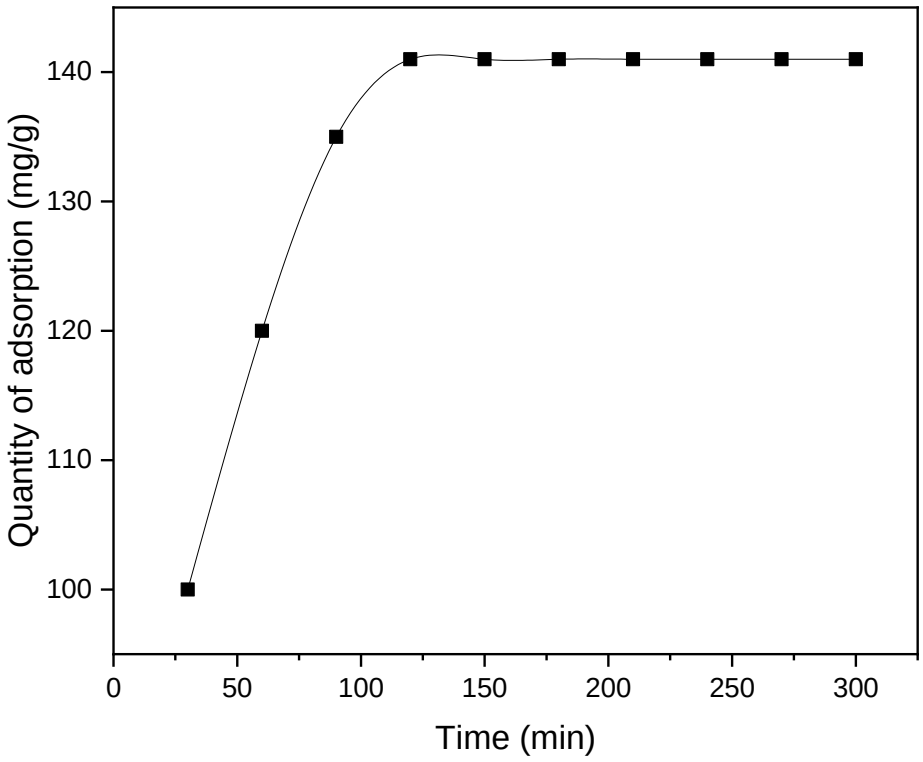

Figure 14: Effect of activation time on the quantity of MB adsorption

The kinetic models of MB molecules adsorption on AGO was investigated by plotting the 1st order and 2nd order versions of kinetic rate equations, which are given by eqn (24) and eqn (25) correspondingly. The respective plots are illustrated in Figure 15(a) shows the first order kinetic model and Figure 15(b) shows the second order kinetic model. The respective kinetic parameters are tabulated in Table II. The 1st order model predicts the q_e values with 16.23% of underestimation. However, the 2nd order model precisely predicts those values with only 4.3% overestimation. Therefore, 1st order model does not fit for the MB adsorption onto the AGO surface. Thus, the 2nd order model reasonably describes the MB adsorption having R^2 of 0.998. Thus, it may be concluded that the rate restrictive stage might be chemisorption which is promoted by either valency forces or covalent forces [125]. The valency forces can be occurred by sharing the electrons between adsorbent and sorbate and the covalent forces can be created by the exchange of electrons between the individuals concerned [125].

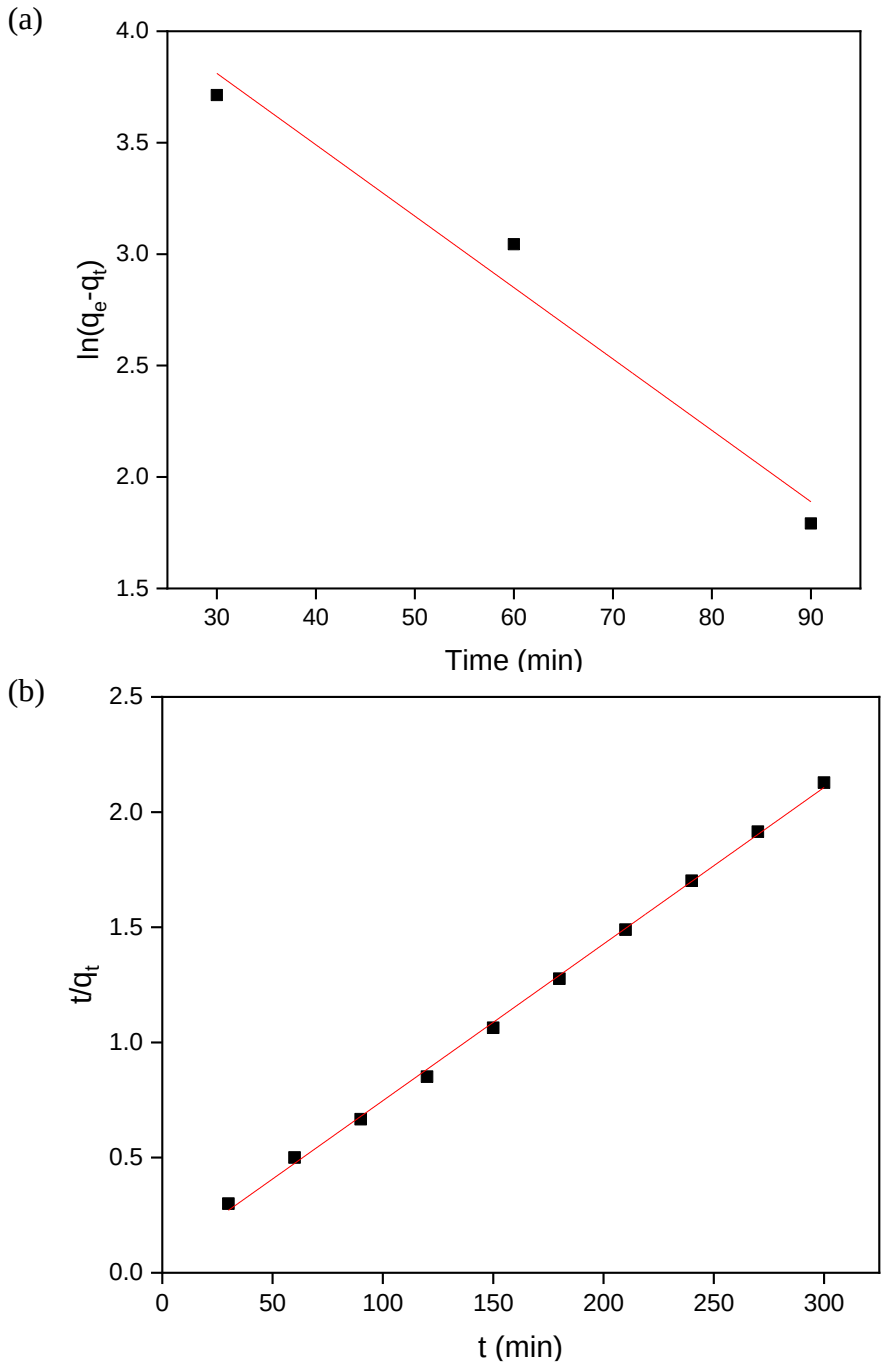

Figure 15: (a) Plot for the 1st order kinetic model, (b) Plot for the 2nd order kinetic model

Table II: Summery of kinetic models

Order	Plot equation	K	q_e.calculated	%difference	R^2
1st order	y = -0.032x + 4.7718	K_1=0.032	118.13	-16.23 %	0.973
2nd order	y = 0.0068x + 0.0673	K_2=0.000747	147.06	+4.3%	0.998

The effect of the intraparticle diffusion on the MB adsorption onto the AGO surface was evaluated based on the intraparticle diffusion model [118,119]. According to Figure 16, this plot behaves having small curvature (mostly linear) initially and an equilibrium state throughout the rest of the plot. This initial curvature represents the bulk diffusion, and the linear section represents the intraparticle diffusion. Normally, bulk diffusion depends on the initial adsorbent concentration. A line is fitted by connecting the data points which behave slight linearly as drawn in the Figure 16. The intercept of this straight line uses to predicts whether the interparticle diffusion is the rate controlling mechanism or not. Figure 16 shows the intraparticle diffusion model and the developed straight line doesn't go through the origin. According to this concept if this line passes through the origin interparticle diffusion would be the rate controlling step [126]. However, considering the calculated $K_{p\ and}$ C values from this line (Equation of y = 8.7333x + 52.222, Kp of 8.7333, C at 52.222, R^2 of 0.99), MB adsorption onto the AGO has mainly driven by bulk diffusion and after initiation, the adsorption is happened mainly by intraparticle diffusion.

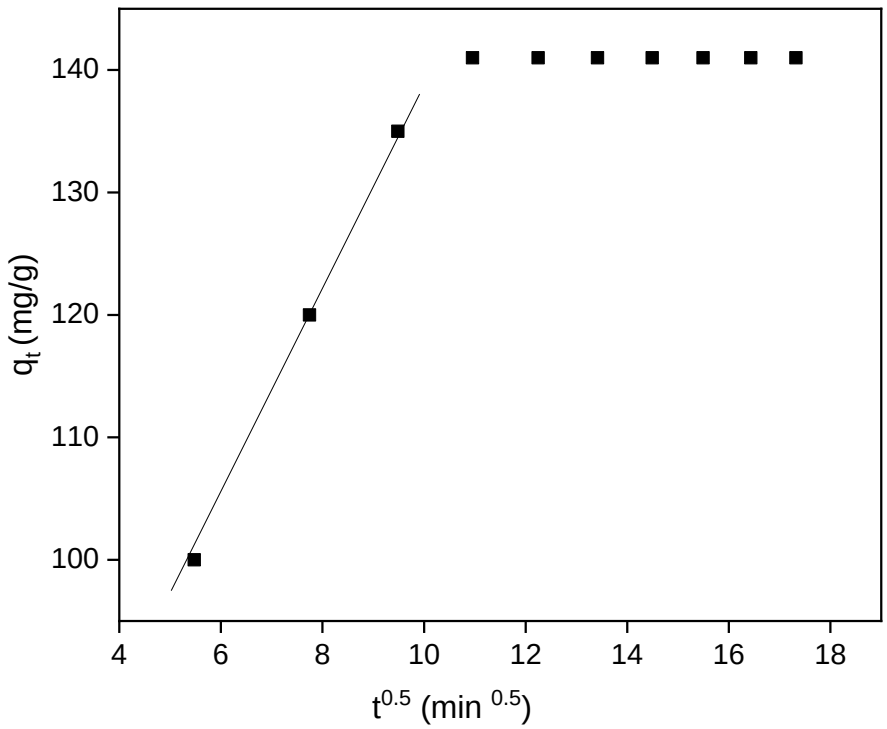

Figure 16: Evaluation of intraparticle model for MB adsorption onto AGO

Adsorption isotherms can be used to understand the adsorption properties of a particular adsorbate into a desired adsorbent and their equilibrium state. Also, the adsorption isotherm describes the adsorption mechanism. The Langmuir model and Freundlich models are the most frequently used equations which explain the adsorption isotherms and in addition, Temkin, Sips, Redlich-Peterson, Halsey, Harkins Jura and Dubinin-Radushkevich isotherms also used [127]. The shape of the isotherm demonstrates the most important information on the adsorption affinity of dye molecules and also gives the thermodynamic data, information about the adsorption spontaneity and the strength of the adsorbent–adsorbate interactions [5, 6, 35, 121, 122]. Models of Langmuir, Freundlich and Temkin were investigated and tested considering the equilibrium conditions at ambient temperature. In Langmuir isotherms, theoretical assumption of monolayer adsorption on adsorbent surface is considered and interactions between the adsorbed molecules are neglected [125]. The methylene blue dye adsorption has successfully described and represented by the equation below.

$$q_e = \frac{q_{max} K_L C_e}{1 + K_L C_e} \quad (27)$$

Here q_e is the amount of absorbate adsorbed per gram of adsorbent after equilibrium(mgg^{-1}) reached and C_e is solute concentration in the aqueous solution (mgL^{-1}) after the equilibrium is reached. K_L and q_{max} and are considered as constants corelated to the adsorption energy (Lmg^{-1}) and to the capacity of maximum adsorption(mgg^{-1}). In Langmuir isotherm another characteristic parameter can be identified as dimension factor r (separation factor) which can be represented as follows.

$$r = (1 + K_L C_0)^{-1} \quad (28)$$

Here C_o denotes the maximum value of commencing absorbate concentration (mgL^{-1}). Type of the isotherm is affiliated to the value of r where the r > 1 means unfavorable, r =1 linear and 0 < r < 1 favorable and r = 0 means irreversible adsorption. This analysis showed the separation factor for at 0.121 and it proves the suitability of Langmuir model for describe this adsorption kinetics.

The empirical model based heterogeneous adsorption on individual active sites is presented by the Freundlich's equation as follows,

$$q_e = K_F C_e^{1/n} \quad (29)$$

Here k_f is the relative adsorption capacity ($mg^{1-(1/n)} L^{1/n} g^{-1}$) and n depicts intensity of adsorption where the n > 1 represents preferable adsorption.

When adsorption sites get filled, Temkin isotherm shows a linear depletion in the adsorption energy. Some amount of heat can be generated by the connections between adsorbate and the adsorbent, which may interrupt the linearity of the MBN with the surface area of the porous material. The characterization of the adsorption can be done by a uniform binding energies distribution until a maximum point. Temkin isotherm is expressed as following equation.

$$q_e = \frac{RT}{b} \ln (AC_e) \quad (30)$$

Here the b is Temkin constant of heat adsorption(J/mol), A is Temkin isotherm constant (Lg^{-1}), T is absolute temperature (K), and R is universal gas constant (8.314

J $mol^{-1}K^{-1}$). Based on the nonlinear X^2 statistic determination test (SS) the best fit model for the distribution was selected where the SS depicts the comparison between experimental q_e and estimated q_e values.

$$SS = \sqrt{\sum(q_{e,calc} - q_{e,exp})^2/N} \qquad (31)$$

Here the N = Number of the experimental points.

As described above, MB adsorption isotherms were evaluated by Langmuir, Freundlich, and Temkin adsorption models and demonstrated in Figure 17. Q_{max} value from the Langmuir isotherm represents the adsorption capacity, having a high value of 655.21 mg/g. This clearly shows its high activation level which corresponds to high porosity. The separation factor (r) is the most important parameter which tells about the favorability of the isotherm for the adsorption behavior. Since r value is in-between 0 and 1, it confirms the appropriateness of Langmuir model to explain the MB adsorption mechanism into AGO. Though the Freundlich equation is an empirical model based on heterogeneous adsorption over independent sites, having n value larger than 1 demonstrates the pertinence of this model for our system. The suitable model for the adsorption mechanism can be found by performing a statistical comparison (SS value). Therefore, according to the Table III the Langmuir model can be selected to sufficiently describe the adsorption of MB onto the AGO surface (higher R^2 and lower SS), considering the corresponding kinetic parameters and mainly from the SS value.

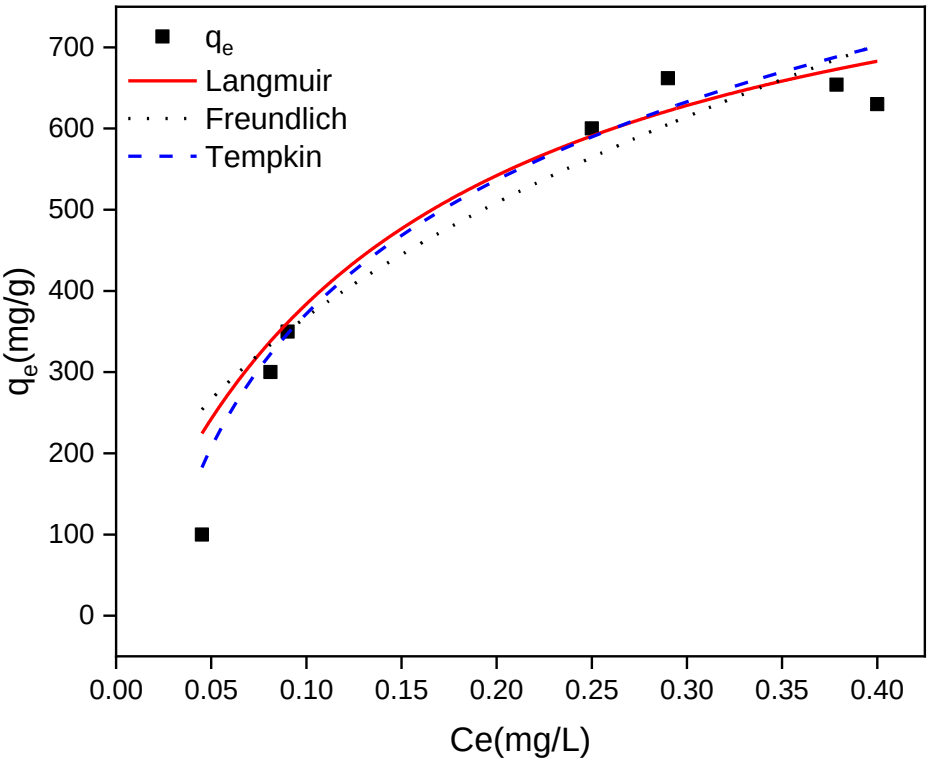

Figure 17: Adsorption isotherms of MB on AGO at 25℃

Table III: Summary of adsorption isotherms

Langmuir		Freundlich		Temkin	
Model	Constant	Model	Constant	Model	Constant
K_L	7.13	K_F	1078	A	47.83
Q_{max}	655.21	n	2.14	b	10.42
r	0.121	R^2	0.78	R^2	0.86
R^2	0.89	SS	2.56	SS	1.96
SS	0.98				

The experiment was conducted to investigate the suitable kinetic and adsorption models for MB adsorption in surface area measurement of AGO. The 2nd order kinetic model was the most favorable kinetic model to describe the MB adsorption onto the AGO surface. And the Langmuir isotherm was found as the best adsorption isotherm among the various adsorption isotherms, which explains this adsorption mechanism adequately. Therefore, having clear understanding of the unique adsorption kinetics of MB dye onto AGO, any surface area calculation would be feasible by following the

2nd order kinetic model and the Langmuir adsorption model. Therefore, MBNs were calculated by following the 2nd order kinetic model and the Langmuir isotherm.

4.1.2. Methylene blue number (MBN)

The amount of methylene blue adsorbed from each solution was calculated by Eqn.19. The analysis of equilibrium condition is important for accurate determination of the MBN. Two classical adsorption models, Langmuir and Freundlich isotherms are most frequently used [1,8,10]. With our sorption experimental results, the Langmuir isotherm equation could be applied to analyze the adsorption equilibrium. Therefore, to determine the MBN for the Langmuir model, the q_{eq} was plotted as a function of C_e. The Langmuir parameters (Q_{max} and K_l) were found by the least square fitting regression[130]–[133].

$$q_{eq} = (C_o - C_e) \times \frac{V}{M} \quad (12)$$

Where, q_{eq}(mg/g) is the amount of methylene blue adsorbed to GO, C_o (mg/L) is the initial concentration of methylene blue, C_e (mg/L) is the equilibrium concentration of methylene blue, V(L) is the treated volume of the methylene blue, and M (g) is the mass of the absorbent (GO).

Langmuir model:

$$q_{eq} = \frac{Q_{\max} K_l C_e}{1 + K_l C_e} \quad (32)$$

Where, q_{eq} (mg/g) is the mass of absorbed methylene blue, C_e (mg/L) is the equilibrium concentration of methylene blue, Q_{max} (mg/g) is the adsorption capacity and K_l (L/mg) is the mass transfer coefficient. Table IV illustrates the MBNs for the AGO samples which were activated at different activation conditions. Sample of AGO(800)-4-60 which was used to verify the SSA by used BET had MBN of 655.21 mg/g.

Table IV:Summary of the Langmuir model for AGO samples

Sample	**Q_{max} (MBN)**		**Sample**	**Q_{max} (MBN)**
AGO(800)-1-60	80.63		**AGO(700)-1-60**	94.73
AGO(800)-2-60	109.87		**AGO(700)-2-60**	101.63
AGO(800)-3-60	545.86		**AGO(700)-3-60**	123.25
AGO(800)-4-60	655.21		**AGO(700)-4-60**	140.22
AGO(800)-5-60	179.84		**AGO(700)-5-60**	101.61

4.1.3. Iodine Number (IN)

The iodine number is defined as the milligrams of iodine adsorbed by 1.0 g of carbon when the iodine concentration of the filtrate is 0.02 N (0.02 mol/L). ASTM D4607-94 method has been used to determine the iodine number. 0.1 N $Na_2S_2O_3$, 0.1 N iodine, 70 mL of concentrated HCl and starch indicator are the standard solutions.

0.1N $Na_2S_2O_3$ solution was prepared by dissolving 24.82 g of sodium thiosulfate in approximately 25 mL of freshly boiled distilled water. Then 0.1 g of sodium carbonate was added to minimize bacterial decomposition of the thiosulfate solution. The mixture was quantitatively transfer to a 1 L volumetric flask and dilute to the mark. Finally, the solution was allowed to stand at least 4 days before standardizing. The solution was stored in an amber bottle.

0.1 N iodine solution was prepared by mixing 12.7 g of iodine (I_2) and 19.1 g of potassium iodide (KI) into a beaker. and it was mixed properly. 5 mL of water was added to the beaker and stirred well. Small increments of water were continuously added while stirring until the total volume is 50 to 60 ml. Then the mixture was allowed to stand a minimum of 4 h to ensure that all crystals are thoroughly dissolved. The mixture was quantitatively transferred to a 1 L volumetric flask and filled to the mark with distilled water. The solution was stored in an amber bottle.

70 mL of concentrated hydrochloric acid to 550 mL of distilled water were added and mixed well to prepare the 5% HCl solution. The starch indicator was prepared as follows. 1 g of starch with 5 to 10 mL of cold water were mixed to make a paste. Then an additional 25 mL of water was added while stirring to the starch paste. Finally, the mixture was Poured into 1 L flask and filled up to the mark the mixture with boiling water. This solution was made fresh daily.

Titration based procedure was followed to calculate the IN. Therefore, three appropriate weighs (0.01 g, 0.02 g, and 0.03 g) of each sample were transferred to a dry and clean 250 ml conical flask. Then 10 ml of 5 w/w% HCl acid was pipetted onto the activated GO sample. The flask was swirled gently until the sample was completely wetted by HCl. This was boiled for 1 min to remove any sulfur contaminate on which might interfere with the titration findings. Then the flask was removed from the hot plate and cooled to room temperature. 100 ml of 0.1 N iodine solution was pipetted into each flask. The solutions were shaken vigorously for 1 min and each mixture was filtered quickly. Then, 50 ml of each filtrate was collected to clean conical flask for the titration. Each filtrate was titrated with 0.1 N sodium thiosulfate solution until the solution was pale yellow. The 2 ml of freshly prepared starch indicator was added, and titration was resumed with sodium thiosulfate until convert to a colorless. Finally, the volumes of sodium thiosulfate consumed for the titration were noted.

Mass of I_2 added for the absorbance (A) was calculated by following equation. Where, N_I is the normality of the iodine solution (0.1 mol/L) and V_I is the volume of the iodine used (ml).

$$A = \frac{N_I \times V_I \times 126.93 \times 1000}{1000} \text{ mg} \quad (13)$$

$$\boldsymbol{A = N_I \times V_I \times 126}$$

Mass of I_2 remained in the titrated volume (B) was calculated as follows.

$Na_2S_2O_3$ moles consumed for the titration $= \frac{N_S \times V_S}{1000}$ (14)

I_2 moles remained in the titrated volume $= \frac{N_S \times V_S}{1000} \times \frac{1}{2}$ (15)

$$B = \frac{N_S \times V_S}{1000} \times \frac{1}{2} \times 126.93 \times 2 \times 1000 \text{ mg} \quad (16)$$

Where, N_S is the normality of the $Na_2S_2O_3$ solution (0.1 mol/L) and Vs is the volume of $Na_2S_2O_3$ consumed for the titration (ml).

$$\boldsymbol{B = N_s \times V_s \times 126.93}$$

Then, the mass of I_2 remained in the filtrate was calculated.

Total contacted volume=$V_H + V_I$

Therefore, Total mass of I_2 remained in the filtrate= $\frac{(V_H + V_I) \times B}{V_F}$ mg (18)

Let, $Dilution\ factor\ (DF) = \frac{V_H + V_I}{V_F}$ (19)

The mass of I_2 remained in the filtrate=$\boldsymbol{DF \times B}$ (20)

Where, V_H is the volume of HCl used (ml), V_F is the volume of filtrate used for the titration (ml) and DF is the dilution factor.

Mass of iodine absorbed.

Mass of iodine absorbed=Mass of I_2 added for the absorbance – Mass of I_2 remained in the filtrate

Mass of iodine absorbed=$A - DF \times B$ (21)

Iodine absorbed per gram of activated GO=$\frac{\boldsymbol{A-(DF \times B)}}{\boldsymbol{M}}$ (22)

Where, M is the mass of activated GO used (g)

Finally, I_2 concentration of the filtrate (C) was found using below equation and the IN was found by Fitting the plot of C vs Mass of iodine absorbed per gram of AGO.

$C=N_I S/F$

The iodine molecule is relatively smaller (area of 0.4 nm^2) than methylene blue molecule, therefore it can enter into the smaller micropores. According to the Table *V*, the adsorption behavior of iodine molecule for the activatied samples is similer to the MB adsorption pattern. It furter proves the suitability of iodine to measure the surface

area of porous materials. Sample of AGO(800)-4-60 which was used to verify the SSA by used BET in a subsequent stage had IN of 548.03 mg/g.

Table V: Calculated Iodine Numbers

Sample	IN (mg/g)	Sample	IN (mg/g)
AGO(800)-1-60	128.12	**AGO(700)-1-60**	110.16
AGO(800)-2-60	369.23	**AGO(700)-2-60**	112.32
AGO(800)-3-60	525.71	**AGO(700)-3-60**	115.36
AGO(800)-4-60	548.03	**AGO(700)-4-60**	120.87
AGO(800)-5-60	310.19	**AGO(700)-5-60**	98.12

4.1.4. Specific Surface area calculation

Cleiton A. and his coworkers have developed two models to calculate the surface area and pore volume and these models have been validated using BET results and literature (Eqn.33 and Eqn.34). Therefore, these two models are used to predict the surface area of the AGO samples.

$$S_{m^2g^{-1}} = 2.28 \times 10^2 - 1.01 \times 10^{-1}\text{MBN} + 3.00 \times 10^{-1}\text{IN} + 1.05 \times 10^{-4}\text{MBN}^2 + 2.00 \times 10^{-4}\text{IN}^2 + 9.38 \times 10^{-4}\text{MBN} \times \text{IN} \quad (33)$$

[120]

$$Vm(cm^3g^{-1}) = 5.60 \times 10^{-2} - 1.00 \times 10^{-3}MBN + 1.55 \times 10^{-4}IN + 7.00 \times 10^{-6}MBN^2 + 1.00 \times 10^{-7}IN^2 - 1.18 \times 10^{-7}MBN\ IN \quad (34)$$

[120]

Table VI illustrates the MBN, IN and calculated SSA values for the activated samples. MBN, IN and SSA values have a similar pattern for the respective samples. It indicates that these dye adsorption results are proportional to the SSA values.

Table VI: Calculated MBN, IN, And SSA

Sample	MBN	IN	SSA
AGO(800)-1-60	80.63	128.12	271.89
AGO(800)-2-60	109.86	369.23	394.13
AGO(800)-3-60	545.86	525.71	685.59
AGO(800)-4-60	655.21	548.03	768.15
AGO(800)-5-60	179.84	310.19	377.75

Sample	MBN	IN	SSA
AGO(700)-1-60	94.73	110.16	264.57
AGO(700)-2-60	101.63	112.32	265.61
AGO(700)-3-60	123.25	115.36	267.59
AGO(700)-4-60	140.22	120.87	270.57
AGO(700)-5-60	101.61	98.12	259.49

Brunauer–Emmett–Teller (BET) is an accurate method to determine surface area and other surface properties such as types of pores and total pore volume. BET analysis was used in this study to verify the SSA which was calculated by dye adsorption. BET explains the physical adsorption of gas molecules on a solid surface, and it is considered an important analysis technique in the specific surface area measurement. Among six types of BET isotherm types, AGO(800)-4-60 shows type I (Figure 18), which illustrates a microporous (< 2 nm) structure of the material. Multipoint BET analysis was done to calculate SSA, resulting a SSA of 749.78 m^2/g.

SSA calculated from MBN and IN for the identical activated sample was 768.15 m^2/g. This value is verified from the BET analysis, which resulted in a SSA value of 749.78 m^2/g. Figure 19 illustrates the pore size distribution, obtained by BET analysis. The average pore size is 1.97 nm.

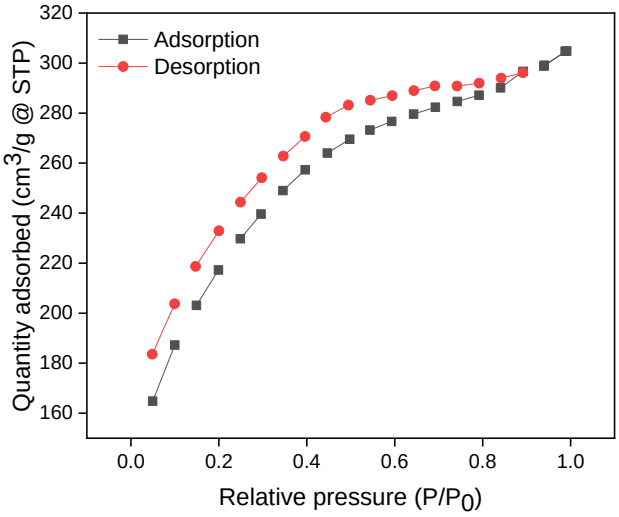

Figure 18: Nitrogen adsorption-desorption isotherm of AGO(800)-4-60

Calculation of SSA

$$\frac{\mathbf{1}}{\boldsymbol{W}[\frac{\boldsymbol{P_0}}{\boldsymbol{P}}-\mathbf{1}]}=\frac{\boldsymbol{C}-\mathbf{1}}{\boldsymbol{W_m C}}\left[\frac{\boldsymbol{P}}{\boldsymbol{P_0}}\right]+\frac{\mathbf{1}}{\boldsymbol{W_m C}} \qquad (35)$$

W- Weight of gas adsorbed

P/P_0- Relative Pressure

W_m- Weight of adsorbate as a monolayer

C-BET constant

Slope: 4.637

Intercept: 0.0095

Wm: 0.215197

C(BET) :489.1474

$$\boldsymbol{Surface\ area}=\frac{\boldsymbol{Wm}\times\boldsymbol{N}\times\boldsymbol{A_{cs}}}{\boldsymbol{M}} \qquad (36)$$

N: Avogadro's number (6.022 X 10^{23})

M: Molecular weight of adsorbate

A_{cs}: Adsorbate cross sectional area (16.2Å for N_2)

Surface area: 749.78 m^2/g

Calculation of average pore size

Total pore volume: 0.3689 cc/g (given)

$$Average\ Pore\ size=\frac{4\times Total\ pore\ volume}{SSA(BET)} \qquad (37)$$

Average pore size = 1.97 nm

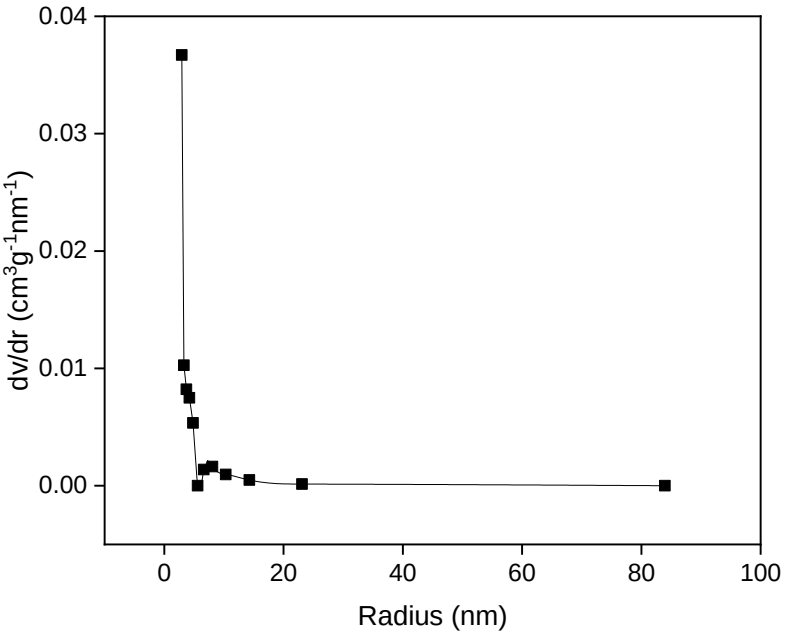

Figure 19: Pore size distribution plot.

The experiment was conducted to investigate the capability of using the MB adsorption in surface area measurement of AGO. The 2nd order kinetic model was the most favorable kinetic model to describe the MB adsorption onto the AGO surface. And the Langmuir isotherm was found as the best adsorption isotherm among the various adsorption isotherms, which explains this adsorption mechanism clearly. Therefore, having clear understanding of the unique adsorption kinetics of MB dye onto AGO, the surface area calculation can be accurately done. Hence, MBN and IN for selected sample of AGO(800)-4-60 was 655.21 mg/g and 548.03 mg/g. The calculated SSA was 768.15 m^2/g and it was almost identical with the value obtained by BET analysis (749.78 m^2/g).

4.2. Preparation and optimization of porous graphene

The target porous material that synthesized in this research is KOH activated GO from Sri Lankan vein graphite. According to the literature review, the modified hummers method is one of the most suitable methods for GO synthesis, particularly in mass scale. Hummer's method promotes to synthesis of more hydrophilic carbon material with higher conductivity and higher yield [134]. Most importantly, the synthesis process doesn't emit any toxic gases [135]. Hence, modified hummers method was followed to synthesize GO from graphite, and then KOH activation was followed to chemically reduce the synthesized GO. The objective of this research is to the preparation of a porous material with ultra-high surface area to replace the existing EDLC electrodes to enhance its performance. Therefore, activation process optimization was done based on the surface area measurements which were taken by dye adsorption methods. This section describes the characterization of graphite, graphene oxide, activated graphene oxide and optimization of the activation process.

4.2.1. Basic characteristics of graphite

The properties of the parent graphite vary the characteristics of the GO such as its functionalization, microstructure and optimum synthesis process parameters [135]. Specially, the crystallinity of the graphite changes the resulted GO sheet size. Hence, Smaller GO sheets with the carboxylic groups, attached at the edges of each sheet can be synthesized from the graphite which have the crystal boundaries with smaller crystallites. However, GO with largely attached epoxy groups can be obtained from the graphite with larger [135]. Sri Lankan vein graphite has high crystallinity and high purity [136]. Therefore, Sri Lankan vein graphite from Bogala graphite mine was used as the carbon precursor for this study. XRD pattern of graphite powder reveals one well-resolved scattering peak (Figure 21) appears at two theta of 26.47 degree and it represents the interlayer distance of 3.36 Å at (002) plane. SEM images of Figure 22 and Figure 23 show that the graphite powder as thick sheet-like structure. And according to Figure 24 the ranges of the graphite surface area and its diameter is 250-500 μm^2 10-20 µm respectively. These indices that graphite powder particles are in the micrometer range, which provides high contact surface area in the synthesis of GO with a better yield. FTIR spectra analysis was presented to investigate the functional groups of the graphite, as shown in Figure 20. The graphite showed apparent

adsorption bands for aromatic C=C (1520 cm^{-1}), alkene C=C (1630 cm^{-1}), and hydroxy –OH (3247 cm^{-1}) groups.

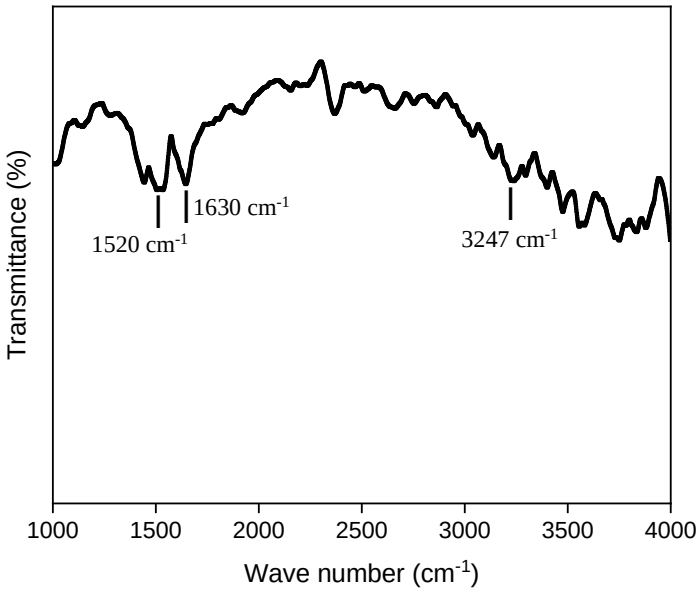

Figure 20: FTIR spectrum of graphite

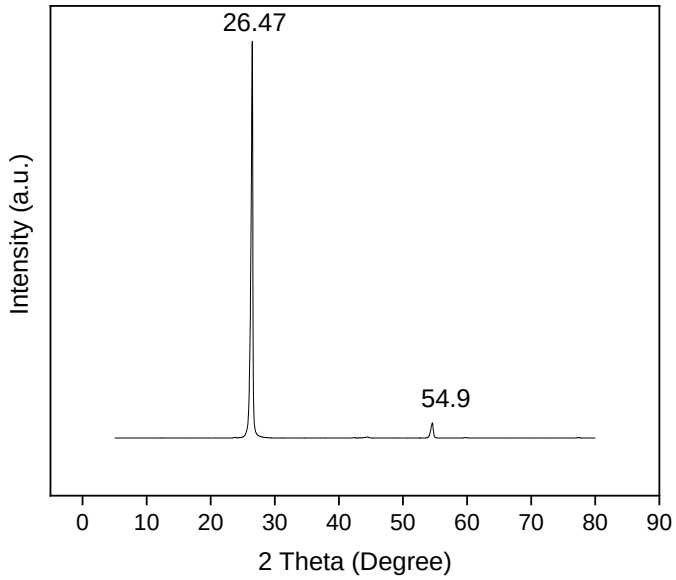

Figure 21: XRD spectrum of graphite

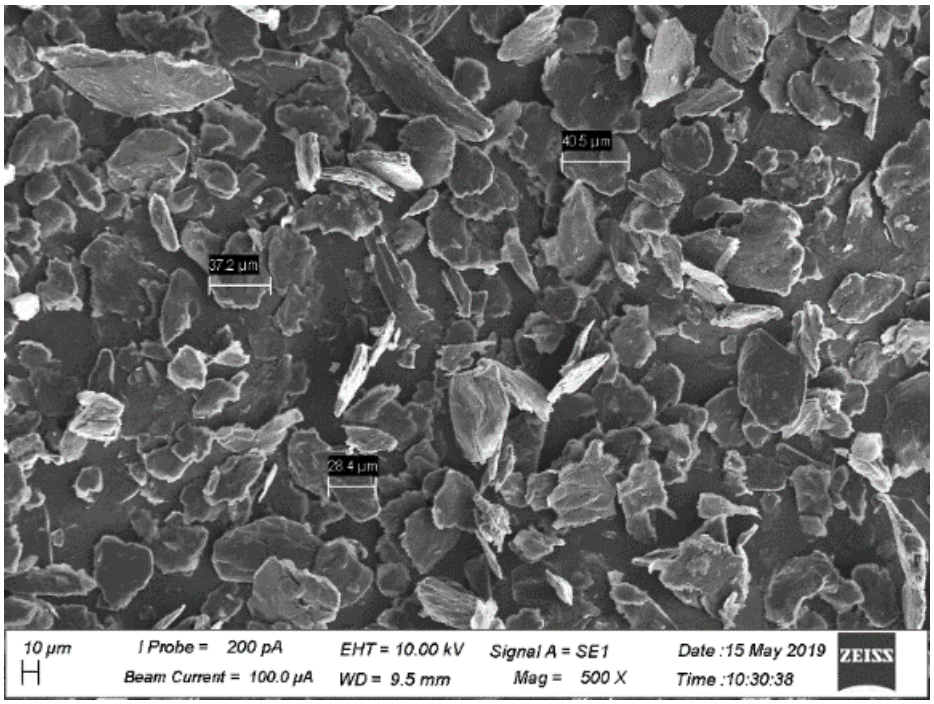

Figure 22:SEM image of graphite powder

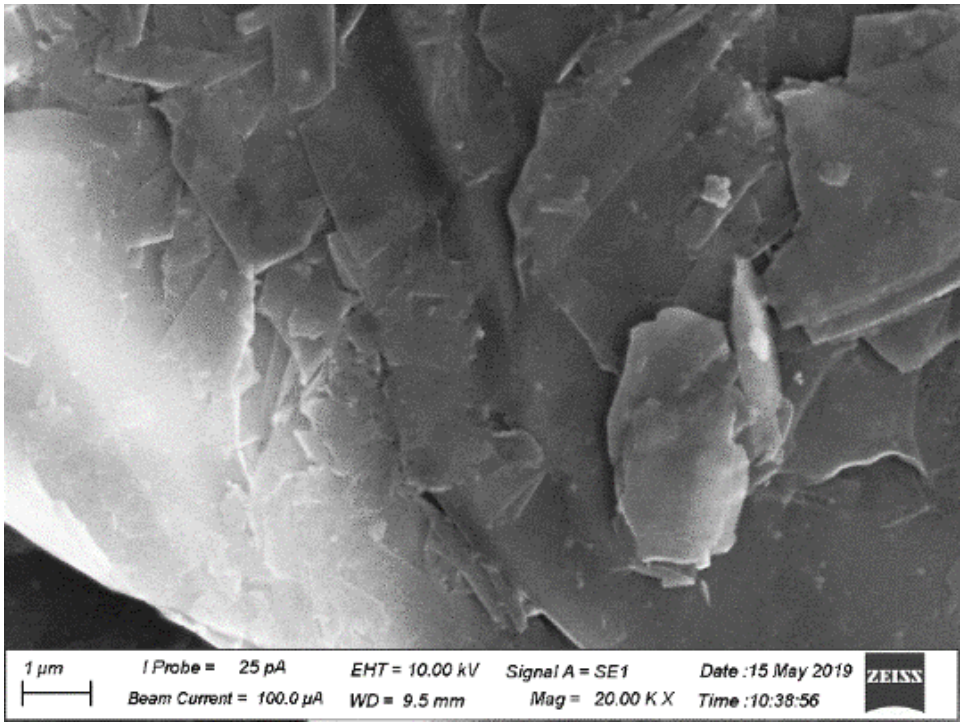

Figure 23: SEM image of the graphite powder particle surface

(a)

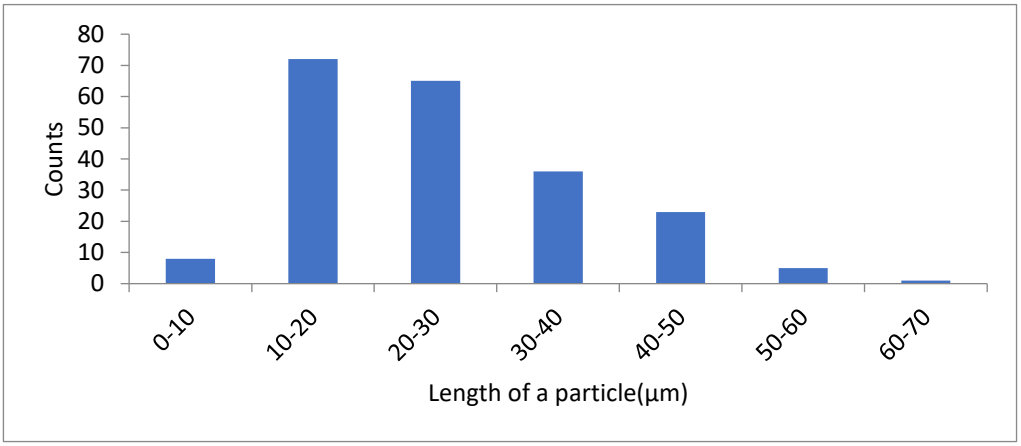

(b)

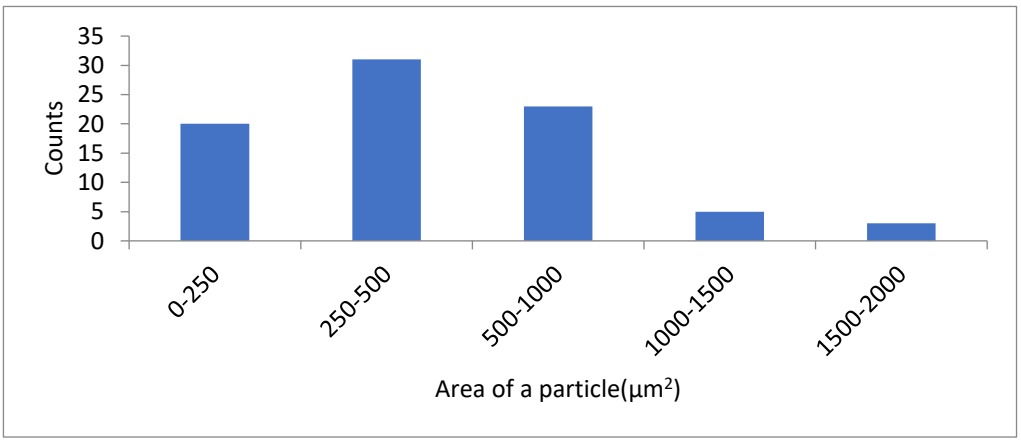

Figure 24:(a) analysis for the length of graphite powder particles. (b) Analysis of the area of the graphite powder particles.

4.2.2. GO characterization.

As shown in Figure 24, the XRD peak of graphite was shifted from 26.48° to 8.718° when it converts to GO. And this results are same as reported in previous studies [129,130]. The position of the XRD peak is related to the spacing between the lattice layers. Hence, the shift of the XRD peak to a lower angle indicates an increase in d-spacing. The sp^2 hybridized shape in a stacked graphite sheet is devastated when the

graphite is oxidized into GO, creating wrinkled defects. These defects have increased the interlayer space from 3.36 Å in graphite powder to 10.14 Å in GO powder. This confirms that the chemical exfoliation has successfully achieved [66,131].

Figure 27 shows the SEM image of graphene oxide (GO) synthesized by modified hummers method. A clear difference can be observed from the SEM images of graphite (Figure 22) and GO (Figure 26), which indicates the proper exfoliation of graphene sheets.

Figure 26 shows the FTIR spectrum of graphite and GO. Significant change of the number of various functional groups after the GO synthesis can be observed directly in the Figure 25. And the FTIR spectrum for GO shows peaks corresponding to the functional groups of hydroxyl (3247 cm^{-1}), C=C aromatic (1520 cm^{-1}) and C=C alkene (1630cm^{-1}) [86], [140]. The presence of aromatic C=C groups shows that even graphite had been oxidized into GO; the main structure of graphite is still retained.

MB absorbance was performed to compare the surface area enhancement after the graphite exfoliation into GO. For this, same weights of graphite powder and GO was contacted with same volumes of identical MB solution and the absorbance of each filtrate were measured after 24 hours. Depending on the porosity, MB molecule can be adsorbed into each material and the filtrate turbidity was used to make a measurement of surface area. Figure 27 shows the color difference of the standard MB solutions after interacting with the same weight of graphite powder and GO for 24 hours. Filtrate absorbance reduction of 0.091 was observed for graphite compared to initial MB solution absorbance and that reading for GO was 3.101. Therefore about 34.08% surface area enhancement can be expected after the GO synthesis. This is strong evidence for greater exfoliation of graphene sheets during the modified hummers method.

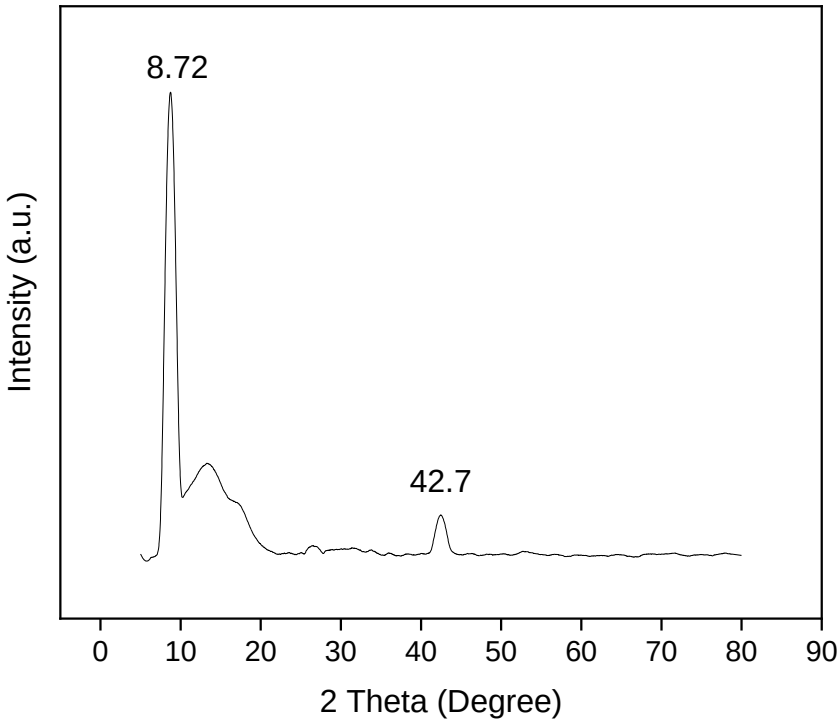

Figure 24:XRD Spectrum of GO

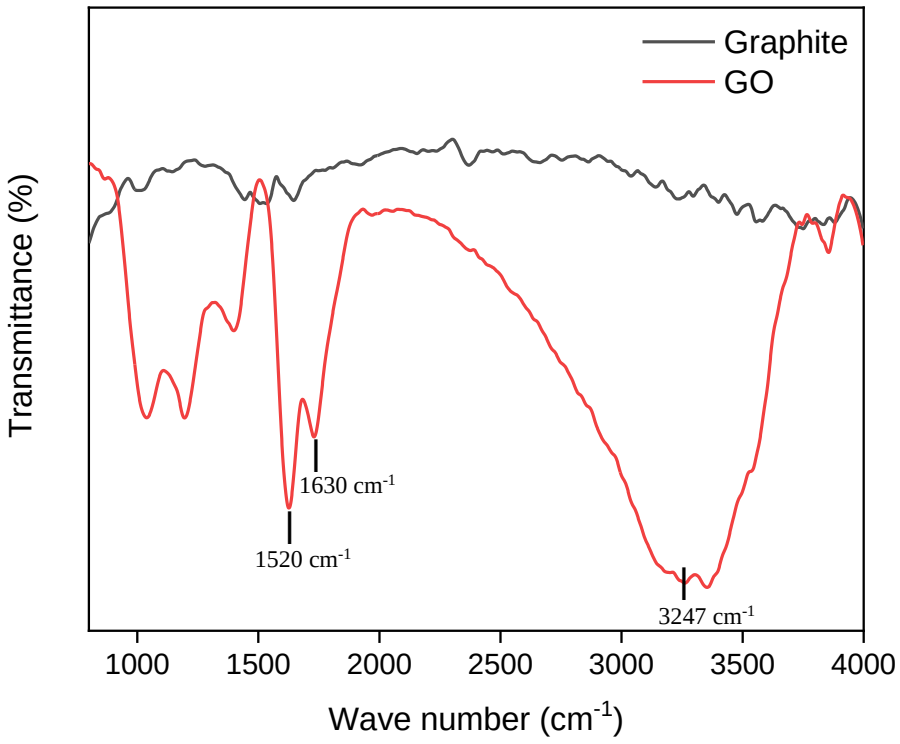

Figure 25:FTIR spectrum of GO

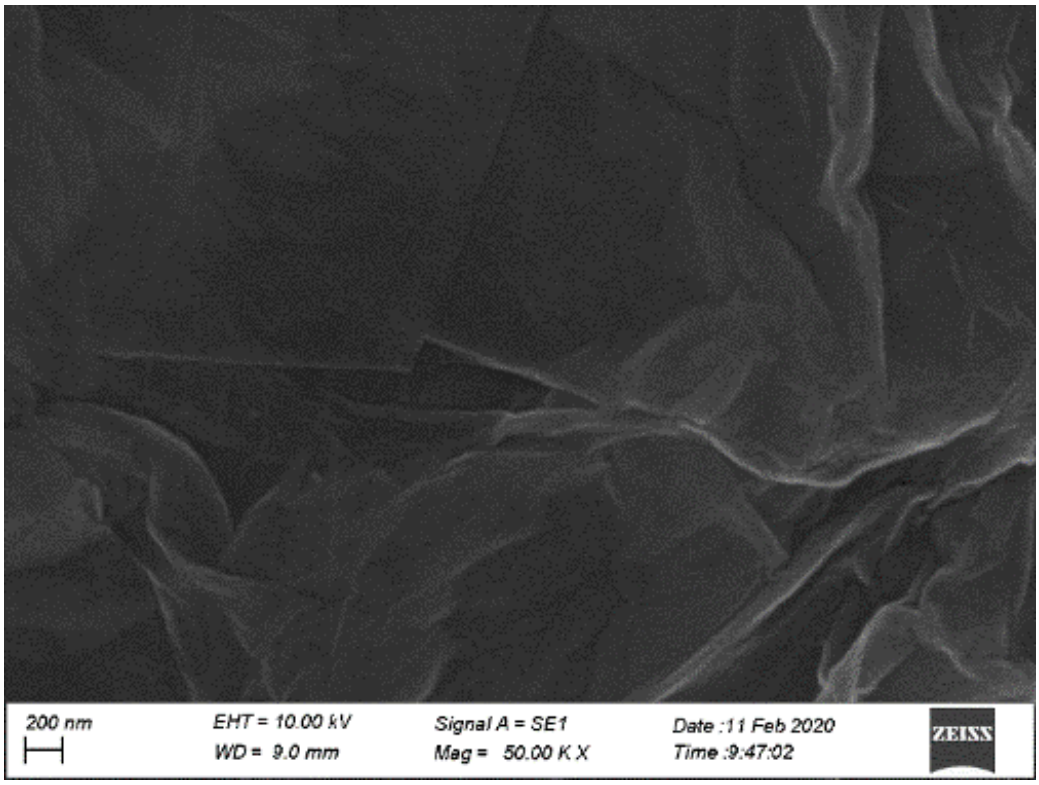

Figure 26: SEM image of GO

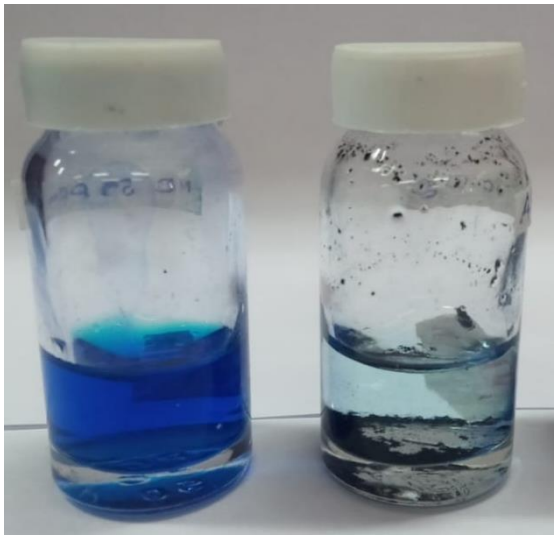

Figure 27: MB absorption performance for graphite (left) and GO (right)

4.2.3. Activation

KOH activation was selected as the one of the promising methods to improve the surface area of GO. Therefore, activation process was done for various samples by varying activation temperature, KOH/GO mass ratio and activation time duration. It was aimed to optimize the most critical activation parameters, to optimize the specific surface area.

5.2.3.1. Activation process finetuning

Despite the major experimental parameters related to the KOH activation, some minor observations were done on several factors which have minor effects on activation process. Even though the effects are not significant, several troubleshooting steps have been taken to improve the activation process. This led to the identification of certain parameters which are not well-studies, however, one need to consider these parameters to carry out a successful activation process.

Effect of the crucible material

The tube furnace is the main equipment that is used for the KOH activation. Tube and the crucibles are made from alumina (Al_2O_3), which is a material with low heat conductivity and high temperature stability. Figure 28 shows; the EDAX spectrum of AGO samples in the first few trials, which showed an unexpected high amount of aluminum (Al).). This clearly showed that the AGO has been contaminated with Al, and it was important to find the root cause of contamination. To investigate this, the precursor materials (graphite and GO) was tested for their purity, however, no Al content is detected in these precursors. Then, the possibility of contamination from crucible material (Al_2O_3) was investigated.

KOH activation occurs in high temperature above 700℃ in liquid and vapor state reaction. Even though alumina is less chemical reactive, a chemical reaction between Al and base (KOH) is possible at extreme temperatures [139].

Therefore, to avoid this issue it was needed to change the crucible material. stainless steel crucible was replaced considering the practical situation and availability. As confirmed by EDAX spectrum in Figure 29, there was not any contaminant of Al when crucible replaced from stainless steel.

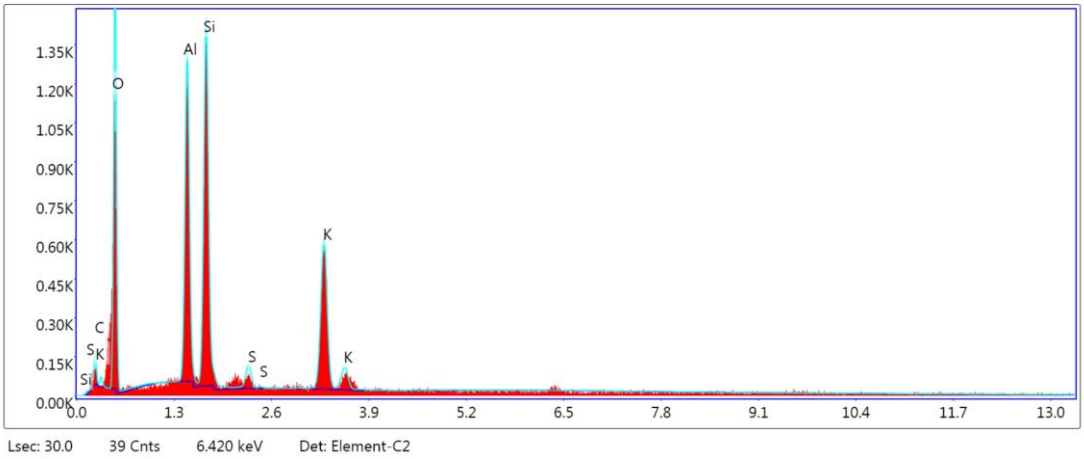

Figure 28:EDAX of activated graphene oxide when alumina was used as the crucible material

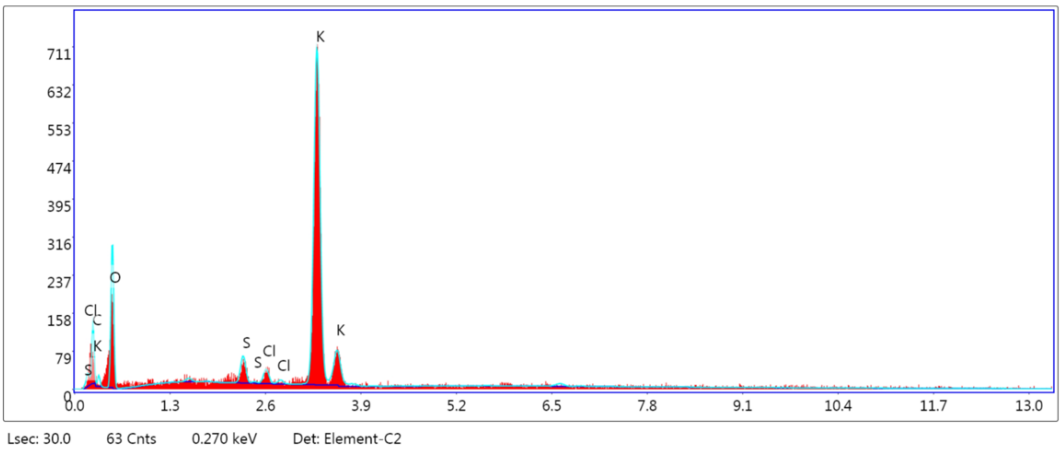

Figure 29: EDAX of AGO when stainless steel was used as the crucible material

Considerable variation of outlet gas flow rate at certain temperatures

Tube furnace gas is exhausted via bubbling into a water bath to measure and control the outlet gas flow rate. The air bubbling rate was noticeably increased at certain temperatures which indicated that some volatile components are emitted due to chemical reactions occurring inside. During the experiment, considerable increase of exhaust gas flow rate was noted at about 300℃ and this can be attributed to emission

of CO_2 and CO as verified by TGA results in Figure 30. Significant rate of mass reduction in TGA curve and remarkable peak upto 350 ℃ in DSC curve verify the formation of gas phase components. This mechanism is discussed in section 2.4.6. Therefore, the observation of exhaust gas flow rate change is helpful confirm that the reactions take place in order. Specially, such observations are helpful to verify the process in industrial setting.

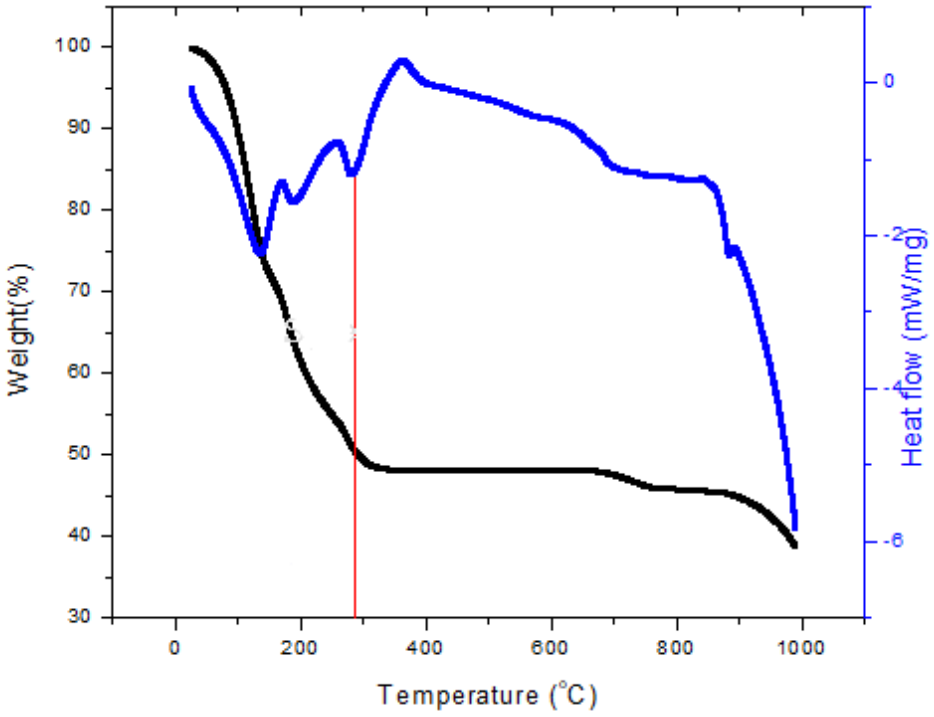

Figure 30: TGA analysis for GO and KOH mixture

Different properties of activated sample by oven drying and freeze drying

Though oven drying of the final suspension from the modified Hummer's method is recommended, physical and chemical properties are not maintained equally to freeze drying does [140]. As Figure 31, the representative physical state of the activated GO is brown color powder, but it is black lumps from the oven drying. Oven dried GO is not totally soluble in alcohol while freeze dried GO easily dissolves in alcohol. Freeze drying is a low temperature process, and the drying is occurred at low temperatures

which restrict the degradation of heat-sensitive products. Therefore, freeze drying is the best method to drying process.

Figure 31:GO samples (a) After oven drying (b) After freeze drying

Effect of the washing duration of activated sample

Effective removal of remaining potassium containing compounds and intercalated metallic K is very important for the porosity development of the GO lattice. Though some literature reported the washing of GO with HCl twice, and twice in distilled water is sufficient, practically this amount of washing is not sufficient for the proper removal of the K compounds. If K compounds are not washed properly, the specific surface area of final product may be decreased. Figure 32 shows a EDAX analysis of insufficiently washed AGO sample. It appears a large amount of remained K compound. Total removal of these elements happens by washing twice with HCl and long duration washing with distilled water until the pH of the filtrate become neutral. This phenomenon can be validated by EDAX characterization (Figure 33).

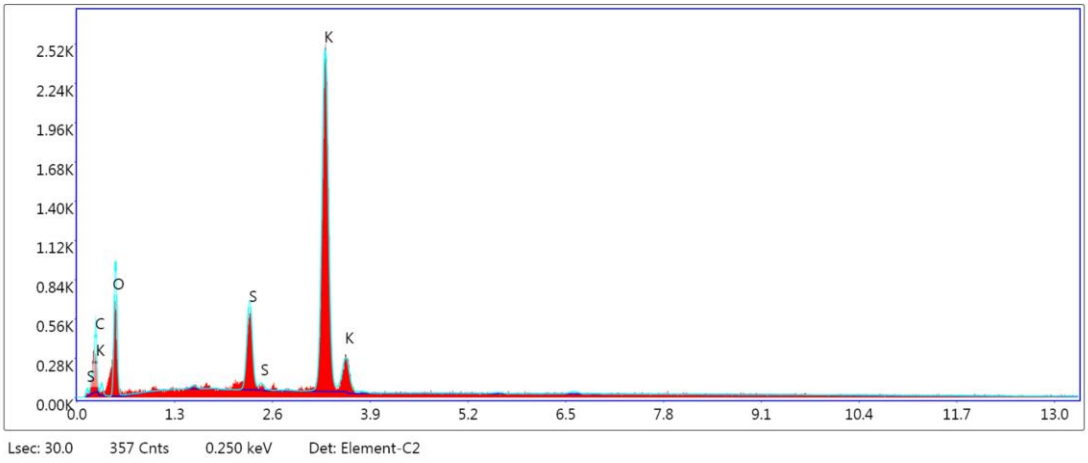

Figure 32: EDAX characterization of activated GO before adequate washing

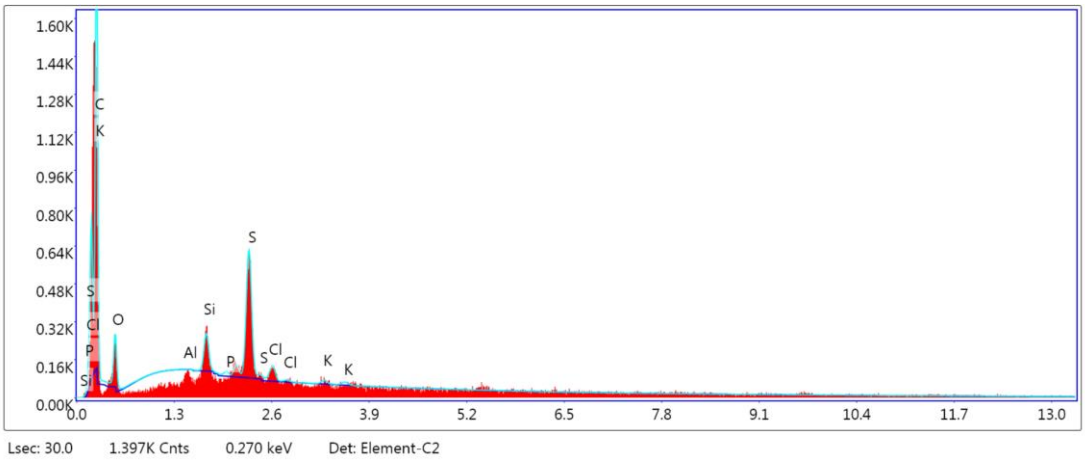

Figure 33:EDAX characterization of activated GO after washing until the filtrate become neutral pH

5.2.3.2. Characteristics of AGO

Many previous researchers have used KOH activation successfully to synthesize porous carbon [87, 90, 132, 133]. Therefore, chemical/heat reduction following KOH activation was used to increase the porosity of the synthesized GO. As shown in SEM micrograph in Figure 34, AGO surface includes crushed thin sheets with notable pores.

The FTIR spectrums for GO and AGO are shown in Figure 35. According to the spectrum, most oxygen containing functional groups observable in GO are absent in the AGO sample. This is expected, as the reduction of oxygen containing functional groups takes place with the chemical activation process. For AGO, the peak at 3247 cm^{-1} decreased compared with GO providing evidence for hydroxy group removal.

The second most important functional group reduction is C=C aromatic and C=C alkene groups which are located between 1520 cm^{-1} -1630cm^{-1} [82 ,137]. This indicates the significant removal of C atoms from the graphene oxide lattice by intercalation of the metallic K during the KOH activation process. This is the reason for the reduction of C=C functional groups after the activation process. This observation is verified with the comparison of SEM micrographs which indicates pores on the GO surface after the activation. The reason for the formation of pores after the KOH activation is the removal of C atoms by the intermediate reactions of the KOH activation process.

Figure 36 shows the graphite, GO, and AGO capabilities to adsorb MB which indicates their surface areas. Two samples of GO and AGO were used to test the MB adsorption capability. As the result, the surface area has been increased by 8.8% in the KOH activation.

Specific surface area was measured following dye adsorption (MBN and IN) isotherms and it was validated by using BET analysis with the optimum sample (AGO(800)-4-60)having the specific surface area at 749.78 m^2/g.

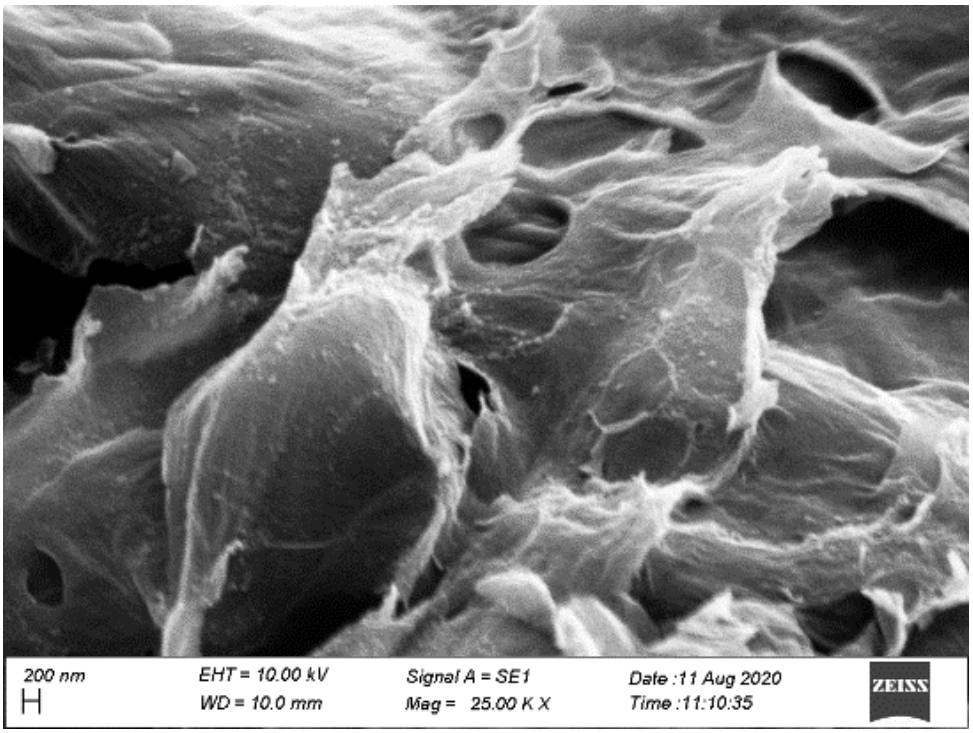

Figure 34:SEM image of AGO

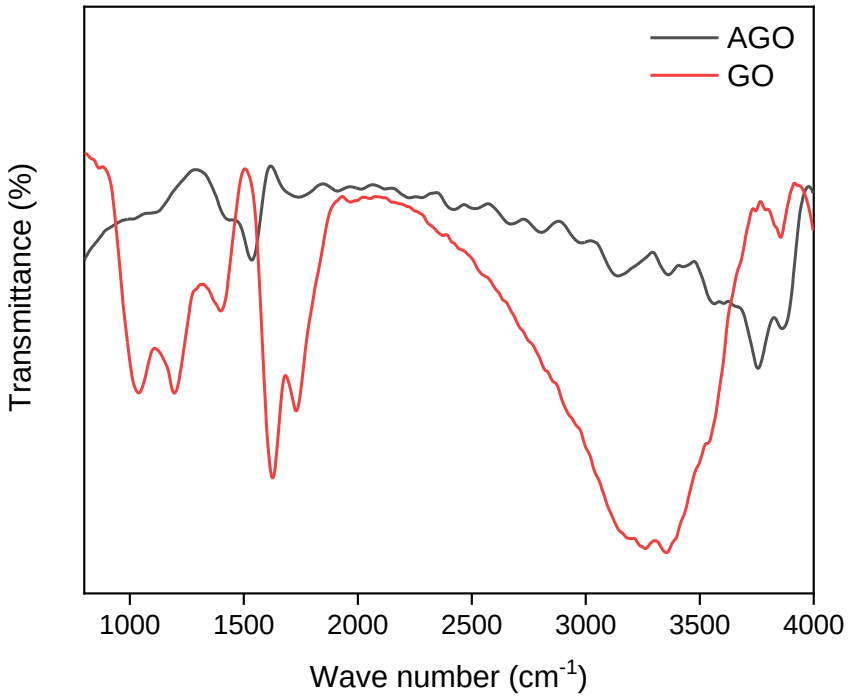

Figure 35:FTIR spectrum for GO and AGO

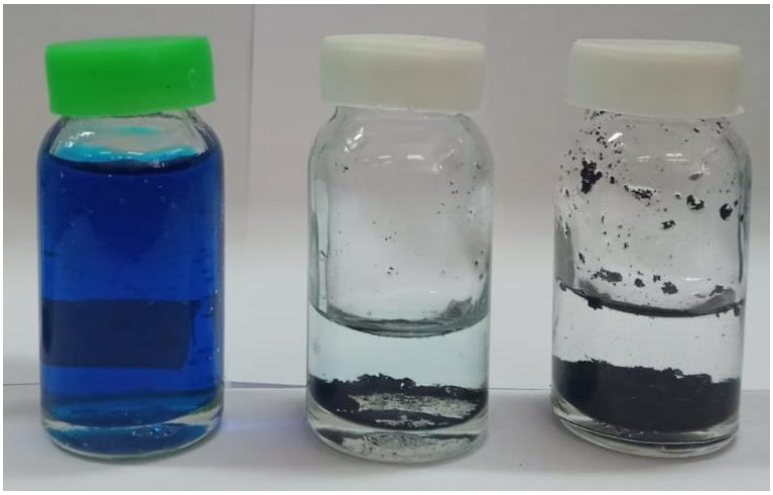

Figure 36: MB adsorption performance of graphite (left), GO (middle) and AGO (right)

5.2.3.3. Influence of KOH activation parameters

Some researchers have reported preparation of activated carbon with a high specific surface area from various carbon sources using KOH as an activation agent [83, 85, 86, 90, 91, 132, 134]. Previous studies have commonly used 800℃ as the activation temperature. However, the activation temperature has not been optimized in earlier studies. Generally, the activation temperature belove 600℃ is not suitable as it doesn't supply sufficient energy to the KOH activation process as explained in section 2.4.6 Hence, 700℃ and 800℃ were chosen as the experimental activation temperatures to find the greatest activation temperature among those temperatures for the GO which was synthesized from the Sri Lankan graphite. Sample titles were given as illustrates in Table VII: Sample names. The activation time durations were 50 min, 60 min, 70 min, and 90 min. And KOH/GO mass ratio was varied from 1 to 5 respectively as the commonly followed KOH/C ratio at 4.

Table VII: Sample names

AGO(700)-1-50	AGO(700)-2-50	AGO(700)-3-50	AGO(700)-4-50	AGO(700)-5-50
AGO(700)-1-60	AGO(700)-2-60	AGO(700)-3-60	AGO(700)-4-60	AGO(700)-5-60
AGO(700)-1-70	AGO(700)-2-70	AGO(700)-3-70	AGO(700)-4-70	AGO(700)-5-70
AGO(700)-1-90	AGO(700)-2-90	AGO(700)-3-90	AGO(700)-4-90	AGO(700)-5-90
AGO(800)-1-50	AGO(800)-2-50	AGO(800)-3-50	AGO(800)-4-50	AGO(800)-5-50
AGO(800)-1-60	AGO(800)-2-60	AGO(800)-3-60	AGO(800)-4-60	AGO(800)-5-60
AGO(800)-1-70	AGO(800)-2-70	AGO(800)-3-70	AGO(800)-4-70	AGO(800)-5-70
AGO(800)-1-90	AGO(800)-2-90	AGO(800)-3-90	AGO(800)-4-90	AGO(800)-5-90

After allowing above samples to adsorb methylene blue samples which are is same concentration and volume, the spectrophotometry readings of the filtrates were taken, and these values were converted to the milligrams of MB adsorbed by 1 gram of GO at the equilibrium state (q_{eq}) from the calibration curve. High absorbance values of the filtrate indicate poor adsorption of MB onto the AGO surface. Therefore, the filtrate absorbance is inversely related to q_{eq} values. In the following discussion, the effect of the three critical activation parameters (activation temperature, KOH/GO mass ratio, activation time) is discussed, with respect to q_{eq} values.

Effect of the activation time

Figure 37 illustrates the q_{eq} values of each filtrate from the reaction between MB and AGOs for 24 hours when the activation temperature at 800 ^{0}C. The absorbance of each filtrate was measured at 664 nm. When any AGO sample has a comparatively higher surface area, it can adsorb a higher amount of MB from the solution. Therefore, the filtrate has a low amount of methylene blue. Then it shows low absorbance than others. Hence, high surface area samples imply lower absorbance values for the filtrate.

According to Figure 37, the variation of the q_{eq} values (relevant to surface area) with the activation times are different. Though it is expected to have an increasing trend of surface area with the activation time, at 60 min implies a high value from the regular pattern at other temperatures for each KOH/C mass ratio. If the curve being parallel to the activation time axis after 60 min, it may prove the activation reaction is terminated because KOH was consumed. However, while the greater porosity at the activation time of 60 min, and it decreases with further increasing the activation time. The possible reason is that when the porosity reaches its maximum at the activation time of 60 min, the KOH is not fully consumed yet. Further increasing the activation time generates additional activation and some micropore structures may get destroyed which leads to a decrease in the specific surface area. A slight increase of q_{eq} values for 90 min is observed. But it is not higher than the q_{eq} values at 60 min. This is more likely to be the removal of volatile matter and mostly due to the severity of carbon burn-off with the increase in holding time [126]. Then it allows creating new pores at these freshly cleared spots with exposure to the heat for a long duration.

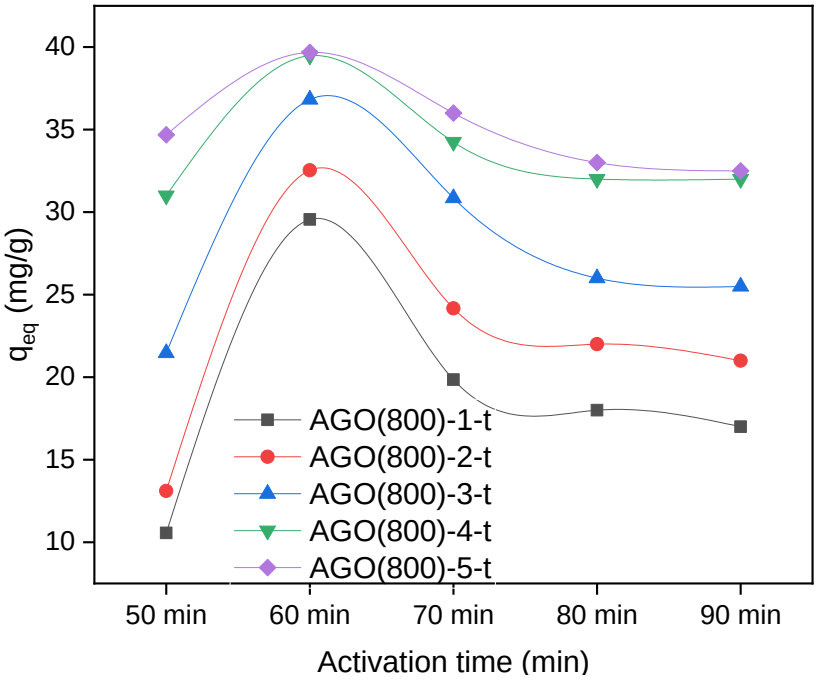

Figure 37: q_{eq}(mg/g) vs activation time (activation at 800℃)

Effect of KOH/GO mass ratio

Figure 38(a) illustrates the effect of the KOH/GO mass ratio on the porosity at different activation times at 800℃. The q_{eq} values are increased with the increase of the KOH/GO mass ratio until 4, and then it becomes a saturated level. This pattern is same for the activation time at 700℃ as Figure 39. Therefore, it indicates that the porosity is increased with the rise of the KOH contribution for the activation process until the mass ratio at 4 and hereafter the remaining KOH is not used significantly. This trend is common for all activation time durations. However, it is not suitable to suggest the highest KOH/GO ratio as the optimum activation condition to achieve a higher surface area. Hence, q_{eq} value growth rate with the KOH/GO mass ratio observation is essential to suggest the optimum KOH/GO mass ratio. Figure 38(b) shows the growth of q_{eq} value at 60 min activation time for different KOH/GO mass ratios. A Higher increment of the q_{eq} indicates a higher increase of the porosity. Therefore, a higher increase of the porosity can be observed at the KOH/GO mass ratio of 3. The increase rate of the porosity is lessened after the KOH/GO mass ratio of 3 and it is negligible at 5. Therefore, a further increase of the KOH mass doesn't have a significant impact on the porosity growth after the KOH/GO mass ratio at 4. The possible reason is that,

though more C atoms are replaced by metallic K atoms during the activation process, at higher KOH/GO mass ratios some micropores are enlarged to mesopores, which lead to decrease the surface area than expected [9].

Effect of activation temperature

Some research groups [143] have reported the optimum temperature for the KOH activation as 800℃. However, it was observed that the activation happens beyond 700℃. Therefore, 700℃ and 800℃ were selected as the activation temperatures in this research compare the effect of activation temperature on the pores tailoring. Increasing activation temperature gradually increases the reaction rate of KOH and GO. As a result, the amount of carbon replacement by metallic K is increased. Simultaneously, there are as such losses in form of carbon burn-off and detach of volatiles at higher temperatures [126]. Therefore, the devolatilization process further develops the random pore structure in the GO surface, whereas the KOH and carbon reaction enhances the existing pores and creates new pores. It is expected, as the increasing temperature will produce increasing the surface area.

Figure 40 reveals the effect of activation temperature on the $Q_{max.}$ Increasing the activation temperature from 700℃ to 800℃ progressively increases the Q_{max} denotes the increment of surface area. Therefore, a further rise of temperature from 700℃ to 800℃, surface area increases due to having more energy for the activation.

(a)

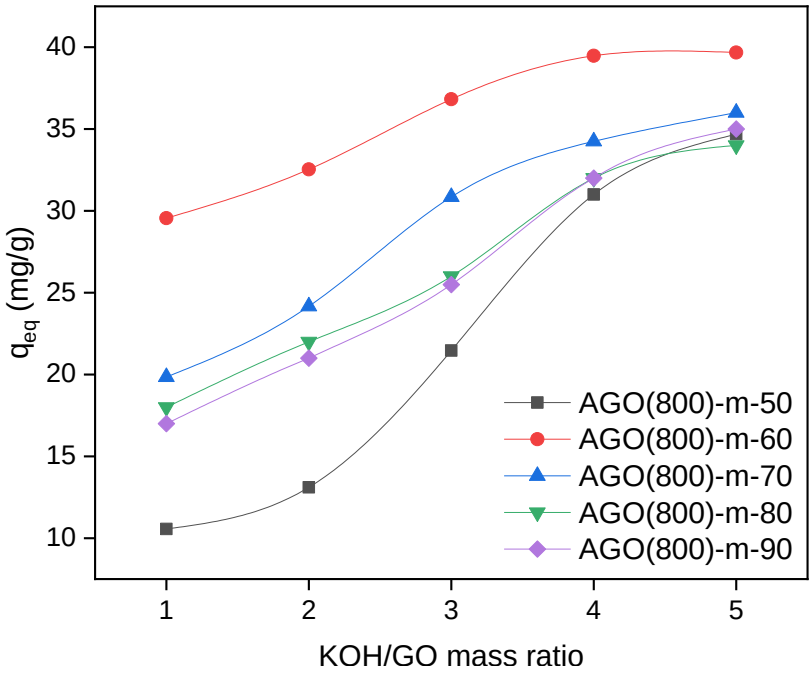

(b)

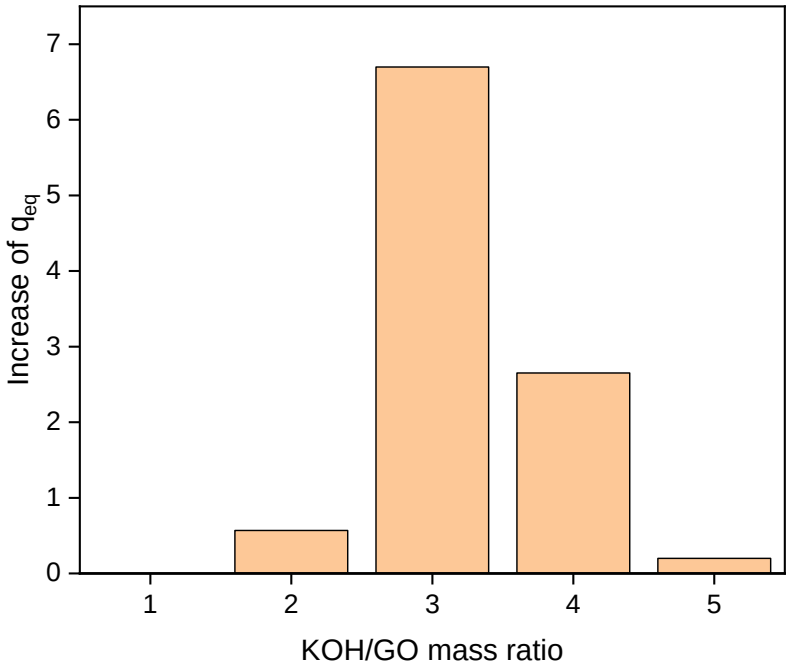

Figure 38:(a) qeq(mg/g) mass of absorbed methylene blue of KOH activated GO samples Vs KOH/GO mass ratio at 800 ^{o}C , (b) Rise of qeq vs KOH/GO mass ratio (activation temperature at 800 ^{o}C for 60 min)

(a)

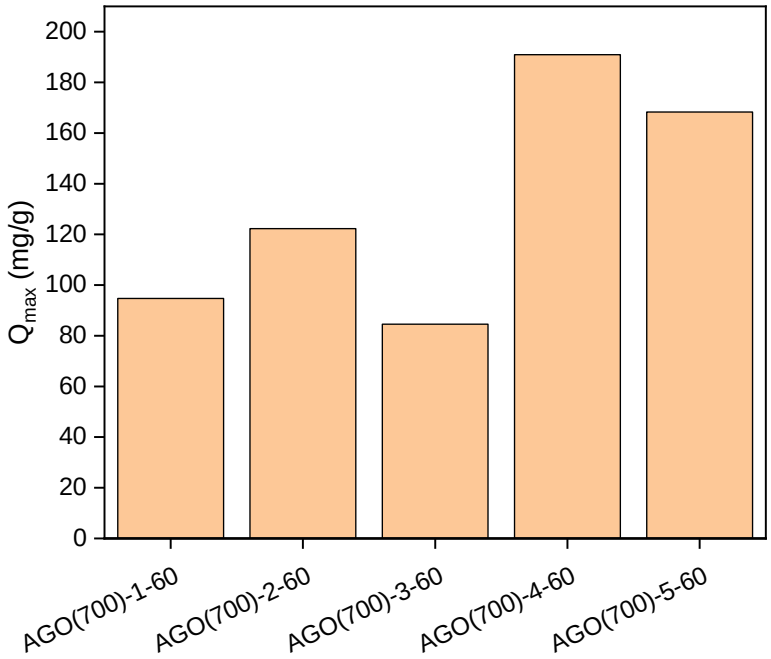

(b)

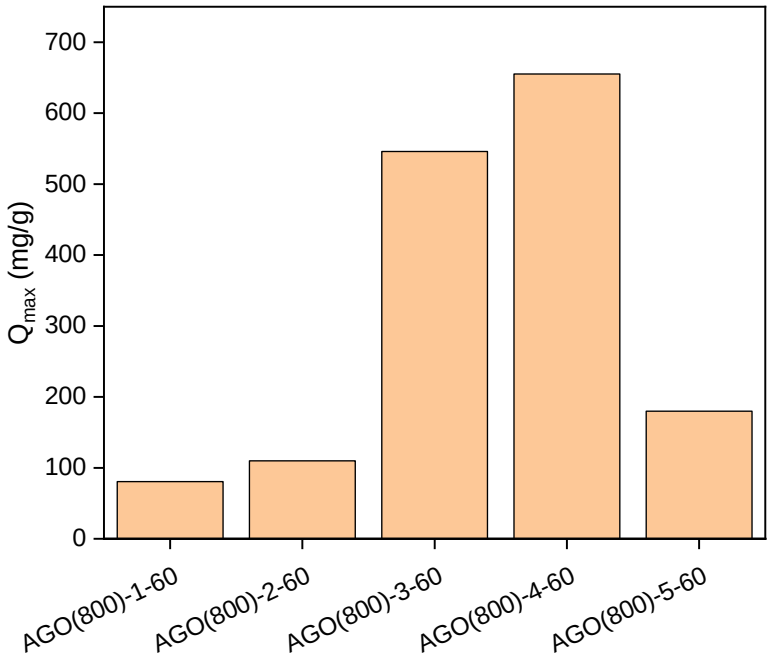

Figure 39:Adsorption capacity (Q_{max}) of AGO samples (a)Activated at 700℃, (b)Activated at 800℃

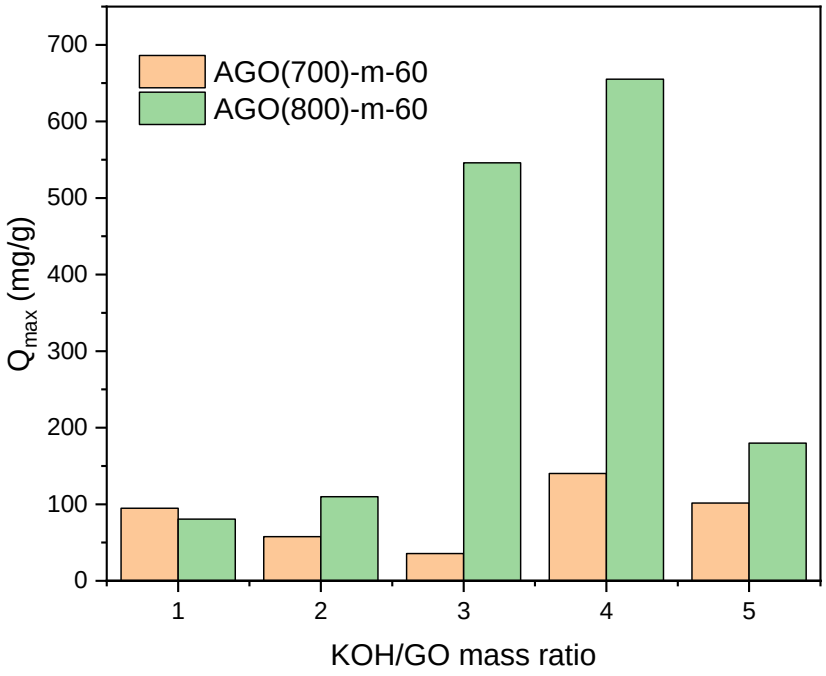

Figure 40: Adsorption capacity (Q_{max}) of AGO samples at the activation temperatures of 700℃ and 800℃

5.2.3.4. Summary

Highly porous graphene was prepared using modified hummers method, followed by KOH activation. In this research, experiments were followed to optimize the critical process parameters of KOH activation process, to optimize the surface area of graphene. Activation time and KOH/GO mass ratio were identified as the critical activation parameters. Therefore, influence of the KOH/GO mass ratio and activation time on the surface area was studied. Methylene blue adsorption was selected to analyze the specific surface area of the prepared materials. In this study, activation time at 60 min and KOH/GO mass ratio at 4 were identified as the optimum activation parameters for high surface area. In addition, obtained optimum activated sample confirmed a high specific surface area (749.78 m^2 /g) comparative to previous studies. This study has provided an insight of KOH activation process, and its effect on the surface area of activated graphene. The outcome of this study is beneficial to produce high capacitance electrode materials for electrochemical double layer capacitors.

5. CONCLUSION

Highly porous graphene was prepared using modified hummers method, followed by KOH activation. In this study, experiments were carried out to optimize the critical process parameters of KOH activation process, by synthesizing of high surface area graphene. Activation time, KOH/GO mass ratio, and activation temperature were identified as the critical activation parameters. Influence of the critical activation parameters on the surface area was studied. Relationship between methylene blue adsorption and the surface area of the activated graphene oxide was elucidated. Kinetics of methylene blue adsorption for the activated samples were studied and the analysis was based on the Langmuir isotherm model.

In this study, activation time was varied from 50 min to 90 min and an activation time of 60 min was identified as the optimum time for high surface area. Further increase of the activation time results in decrease in the specific surface area, as the micropore structure is destroyed. KOH/GO mass ratio was varied from 1 to 5 and this ratio at 4 was identified as the optimum KOH/GO mass ratio. Although, 800°C was identified as the best activation temperature.

Capability of the dye adsorption for the surface area measurement was studied. Methylene blue and iodine was used to analyze the surface area of the activated samples. Strongly validated and published mathematical model was used to calculate the specific surface area by methylene blue number and iodine number. According to the model, optimum sample (AGO(800)-4-60) showed SSA of 768.15 m^2/g and this value was verified by BET analysis (749.78 m^2/g). The obtained optimum activated sample confirmed a high specific surface area, comparative to previous studies. Among the available publications which attempted to enhance the surface area of Sri Lankan graphite, these results show a high potential to prepare highly porous graphene.

Nevertheless, no comprehensive studies have been conducted to chemically activate the graphene oxide from high purity Sri Lankan graphite as well as the analyze the effect of all three critical activation process parameters on the surface area by adsorption isotherms. This study extends the possibility to successfully apply the optimized activated sample in organic and aqueous electrolytes and it will facilitate the fabrication of high capacitance EDLC electrodes.

REFERENCES

[1] A. González, E. Goikolea, J. A. Barrena, and R. Mysyk, "Review on supercapacitors: Technologies and materials," *Renew. Sustain. Energy Rev.*, vol. 58, pp. 1189–1206, 2016, doi: 10.1016/j.rser.2015.12.249.

[2] J. Conder, K. Fic, and T. Electrochemistry, *Supercapacitors (electrochemical capacitors) 10*. 2019.

[3] L. Chen *et al.*, "Synthesis of Nitrogen-Doped Porous Carbon Nanofibers as an Efficient Electrode Material for Supercapacitors," *ACS Nano*, vol. 61, no. 3, pp. 201–2012, 2012, doi: 10.1021/nn302147s.

[4] W. Zuo, R. Li, C. Zhou, Y. Li, J. Xia, and J. Liu, "Battery-Supercapacitor Hybrid Devices: Recent Progress and Future Prospects," *Adv. Sci.*, vol. 4, no. 7, pp. 1–21, 2017, doi: 10.1002/advs.201600539.

[5] P. Sharma and T. S. Bhatti, "A review on electrochemical double-layer capacitors," *Energy Convers. Manag.*, vol. 51, no. 12, pp. 2901–2912, 2010, doi: 10.1016/j.enconman.2010.06.031.

[6] C. Largeot, C. Portet, J. Chmiola, P. L. Taberna, Y. Gogotsi, and P. Simon, "Relation between the ion size and pore size for an electric double-layer capacitor," *J. Am. Chem. Soc.*, vol. 130, no. 9, pp. 2730–2731, 2008, doi: 10.1021/ja7106178.

[7] R. Härmas *et al.*, "Influence of porosity parameters and electrolyte chemical composition on the power densities of non-aqueous and ionic liquid based supercapacitors," *Electrochim. Acta*, vol. 283, pp. 931–948, 2018, doi: 10.1016/j.electacta.2018.06.115.

[8] K. Urita, C. Urita, K. Fujita, K. Horio, M. Yoshida, and I. Moriguchi, "The ideal porous structure of EDLC carbon electrodes with extremely high capacitance," *Nanoscale*, vol. 9, no. 40, pp. 15643–15649, 2017, doi: 10.1039/c7nr05307j.

[9] Y. Ji, T. Li, L. Zhu, X. Wang, and Q. Lin, "Preparation of activated carbons by microwave heating KOH activation," vol. 254, pp. 506–512, 2007, doi:

10.1016/j.apsusc.2007.06.034.

[10] L. Khezami, A. Ould-Dris, and R. Capart, “Activated carbon from thermo-compressed wood and other lignocellulosic precursors,” *BioResources*, vol. 2, no. 2, pp. 193–209, 2007, doi: 10.15376/biores.2.2.193-209.

[11] N. K. N. Quach, W. D. Yang, Z. J. Chung, and H. L. Tran, “The Influence of the Activation Temperature on the Structural Properties of the Activated Carbon Xerogels and Their Electrochemical Performance,” *Adv. Mater. Sci. Eng.*, vol. 2017, 2017, doi: 10.1155/2017/8308612.

[12] Z. Y. Li, M. S. Akhtar, D. H. Kwak, and O. B. Yang, “Improvement in the surface properties of activated carbon via steam pretreatment for high performance supercapacitors,” *Appl. Surf. Sci.*, vol. 404, pp. 88–93, 2017, doi: 10.1016/j.apsusc.2017.01.238.

[13] Q. Lu, Y.-Y. Xu, S.-J. Mu, and W.-C. Li, “The effect of nitrogen and/or boron doping on the electrochemical performance of non-caking coal-derived activated carbons for use as supercapacitor electrodes,” *Carbon N. Y.*, vol. 130, no. 2018, p. 844, 2018, doi: 10.1016/j.carbon.2017.10.057.

[14] T. Kim, G. Jung, S. Yoo, K. S. Suh, and R. S. Ruoff, “Activated graphene-based carbons as supercapacitor electrodes with macro- and mesopores,” *ACS Nano*, vol. 7, no. 8, pp. 6899–6905, 2013, doi: 10.1021/nn402077v.

[15] J. Conder, K. Fic, and C. Matei Ghimbeu, *Supercapacitors (electrochemical capacitors)*. 2019.

[16] E. E. Miller, Y. Hua, and F. H. Tezel, “Materials for energy storage: Review of electrode materials and methods of increasing capacitance for supercapacitors,” *J. Energy Storage*, vol. 20, no. August, pp. 30–40, 2018, doi: 10.1016/j.est.2018.08.009.

[17] V. V. N. Obreja, “Supercapacitors specialities - Materials review,” *AIP Conf. Proc.*, vol. 1597, no. February, pp. 98–120, 2014, doi: 10.1063/1.4878482.

[18] J. M. Chem, “PAPER A comprehensive study on KOH activation of ordered

mesoporous carbons and their supercapacitor application †," pp. 93–99, 2012, doi: 10.1039/c1jm12742j.

[19] M. A. Raza, A. Westwood, A. Brown, N. Hondow, and C. Stirling, "Graphite nanoplatelets produced by oxidation and thermal exfoliation of graphite and electrical conductivities of their epoxy composites," *J. Nanosci. Nanotechnol.*, vol. 12, no. 12, pp. 9259–9270, 2012, doi: 10.1166/jnn.2012.6778.

[20] N. W. B. Balasooriya and P. Touzain, "Capacity improvement of mechanically and chemically treated Sri Lanka natural graphite as an anode material in Li-ion batteries," pp. 305–309, 2007, doi: 10.1007/s11581-007-0114-y.

[21] N. W. B. Balasooriya, H. P. T. S. Hewathilake, R. M. U. M. Somarathna, H. W. M. A. C. Wijayasinghe, L. P. S. Rohitha, and H. M. T. G. A. Pitawala, "Physical and Chemical Purification of Sri Lankan Flake Graphite and Vein Graphite," *5th Int. Symp. 2015 – IntSym, SEUSL Phys.*, no. January, pp. 163–166, 2015,

[22] L. Z. Fan, S. Qiao, W. Song, M. Wu, X. He, and X. Qu, "Effects of the functional groups on the electrochemical properties of ordered porous carbon for supercapacitors," *Electrochim. Acta*, vol. 105, pp. 299–304, 2013, doi: 10.1016/j.electacta.2013.04.137.

[23] C. Liu, Z. Yu, D. Neff, A. Zhamu, and B. Z. Jang, "Graphene-based supercapacitor with an ultrahigh energy density," *Nano Lett.*, vol. 10, no. 12, pp. 4863–4868, 2010, doi: 10.1021/nl102661q.

[24] Y. He *et al.*, "Capacitive mechanism of oxygen functional groups on carbon surface in supercapacitors," *Electrochim. Acta*, vol. 282, pp. 618–625, 2018, doi: 10.1016/j.electacta.2018.06.103.

[25] R. Lin, P. L. Taberna, J. Chmiola, D. Guay, Y. Gogotsi, and P. Simon, "Microelectrode Study of Pore Size, Ion Size, and Solvent Effects on the Charge/Discharge Behavior of Microporous Carbons for Electrical Double-Layer Capacitors," *J. Electrochem. Soc.*, vol. 156, no. 1, p. A7, 2009, doi: 10.1149/1.3002376.

[26] Y. H. Hu, H. Wang, and B. Hu, "Thinnest two-dimensional nanomaterial-

graphene for solar energy," *ChemSusChem*, vol. 3, no. 7, pp. 782–796, 2010, doi: 10.1002/cssc.201000061.

[27] L. Hu *et al.*, "Direct anodic exfoliation of graphite onto high-density aligned graphene for large capacity supercapacitors," *Nano Energy*, vol. 34, no. January, pp. 515–523, 2017, doi: 10.1016/j.nanoen.2017.03.007.

[28] E. Kusrini, A. Suhrowati, A. Usman, M. Khalil, and V. Degirmenci, "Synthesis and characterization of graphite oxide, graphene oxide, and reduced graphene oxide from graphite waste using modified hummers' method and zinc as reducing agent," *Int. J. Technol.*, vol. 10, no. 6, pp. 1093–1104, 2019, doi: 10.14716/ijtech.v10i6.3639.

[29] Z. Jiang, Z. Jiang, and W. Chen, "The role of holes in improving the performance of nitrogen-doped holey graphene as an active electrode material for supercapacitor and oxygen reduction reaction," *J. Power Sources*, vol. 251, pp. 55–65, 2014, doi: 10.1016/j.jpowsour.2013.11.031.

[30] D. Zhu *et al.*, "Nitrogen-doped porous carbons with nanofiber-like structure derived from poly (aniline-co-p-phenylenediamine) for supercapacitors," *Electrochim. Acta*, vol. 224, pp. 17–24, 2017, doi: 10.1016/j.electacta.2016.12.023.

[31] J. N. Ramavath, M. Raja, S. Kumar, and R. Kothandaraman, "Mild acidic mixed electrolyte for high-performance electrical double layer capacitor," *Appl. Surf. Sci.*, vol. 489, pp. 867–874, 2019, doi: 10.1016/j.apsusc.2019.05.343.

[32] Y. Lv, F. Zhang, Y. Zhai, and J. Wang, "PAPER A comprehensive study on KOH activation of ordered mesoporous carbons," no. September, 2011, doi: 10.1039/C1JM12742J.

[33] M. A. Lillo-Ródenas, D. Cazorla-Amorós, and A. Linares-Solano, "Understanding chemical reactions between carbons and NaOH and KOH: An insight into the chemical activation mechanism," *Carbon N. Y.*, vol. 41, no. 2, pp. 267–275, 2003, doi: 10.1016/S0008-6223(02)00279-8.

[34] H. C. Youn *et al.*, "High-surface-area nitrogen-doped reduced graphene oxide

for electric double-layer capacitors," *ChemSusChem*, vol. 8, no. 11, pp. 1875–1884, 2015, doi: 10.1002/cssc.201500122.

[35] K. Gopalsamy, J. Balamurugan, T. D. Thanh, N. H. Kim, and J. H. Lee, "Fabrication of nitrogen and sulfur co-doped graphene nanoribbons with porous architecture for high-performance supercapacitors," *Chem. Eng. J.*, vol. 312, pp. 180–190, 2017, doi: 10.1016/j.cej.2016.11.130.

[36] S. Zhang and N. Pan, "Supercapacitors performance evaluation," *Adv. Energy Mater.*, vol. 5, no. 6, pp. 1–19, 2015, doi: 10.1002/aenm.201401401.

[37] Y. Shao *et al.*, "Design and Mechanisms of Asymmetric Supercapacitors," *Chem. Rev.*, vol. 118, no. 18, pp. 9233–9280, 2018, doi: 10.1021/acs.chemrev.8b00252.

[38] Y. Wang, Y. Song, and Y. Xia, "Electrochemical capacitors: Mechanism, materials, systems, characterization and applications," *Chem. Soc. Rev.*, vol. 45, no. 21, pp. 5925–5950, 2016, doi: 10.1039/c5cs00580a.

[39] J. Libich, J. Máca, J. Vondrák, O. Čech, and M. Sedlaříková, "Supercapacitors: Properties and applications," *J. Energy Storage*, vol. 17, no. March, pp. 224–227, 2018, doi: 10.1016/j.est.2018.03.012.

[40] R. German, P. Venet, A. Sari, O. Briat, and J. M. Vinassa, "Electrochemical Double Layer Capacitors (supercapacitors) ageing impacts and comparison on different impedance models," *EPE J. (European Power Electron. Drives Journal)*, vol. 24, no. 3, pp. 6–13, 2014, doi: 10.1080/09398368.2014.11742747.

[41] X. Chen, R. Paul, and L. Dai, "Carbon-based supercapacitors for efficient energy storage," *Natl. Sci. Rev.*, vol. 4, no. 3, pp. 453–489, 2017, doi: 10.1093/nsr/nwx009.

[42] J.-H. Lee, S. Park, and J.-W. Choi, "Electrical Property of Graphene and Its Application to Electrochemical Biosensing," *Nanomaterials*, vol. 9, no. 2, p. 297, 2019, doi: 10.3390/nano9020297.

[43] G. Leofanti, M. Padovan, G. Tozzola, and B. Venturelli, "Surface area and pore

texture of catalysts," *Catal. Today*, vol. 41, no. 1–3, pp. 207–219, 1998, doi: 10.1016/S0920-5861(98)00050-9.

[44] Y. Wen, G. Cao, J. Cheng, and Y. Yang, "Correlation of capacitance with the pore structure for nanoporous glassy carbon electrodes," *J. Electrochem. Soc.*, vol. 152, no. 9, pp. 1770–1775, 2005, doi: 10.1149/1.1984447.

[45] S. M. Lamine, C. Ridha, H. M. Mahfoud, C. Mouad, B. Lotfi, and A. H. Al-Dujaili, "Chemical activation of an activated carbon prepared from coffee residue," *Energy Procedia*, vol. 50, pp. 393–400, 2014, doi: 10.1016/j.egypro.2014.06.047.

[46] C. Portet, Z. Yang, Y. Korenblit, Y. Gogotsi, R. Mokaya, and G. Yushin, "Electrical double-layer capacitance of zeolite-templated carbon in organic electrolyte," *J. Electrochem. Soc.*, vol. 156, no. 1, pp. 1–6, 2009, doi: 10.1149/1.3002375.

[47] J. S. Moon, H. Kim, D. C. Lee, J. T. Lee, and G. Yushin, "Increasing capacitance of zeolite-templated carbons in electric double layer capacitors," *J. Electrochem. Soc.*, vol. 162, no. 5, pp. A5070–A5076, 2015, doi: 10.1149/2.0131505jes.

[48] Z. He *et al.*, "The effect of activation methods on the electrochemical performance of ordered mesoporous carbon for supercapacitor applications," *J. Mater. Sci.*, vol. 52, no. 5, pp. 2422–2434, 2017, doi: 10.1007/s10853-016-0536-x.

[49] I. Yang, S. G. Kim, S. H. Kwon, M. S. Kim, and J. C. Jung, "Relationships between pore size and charge transfer resistance of carbon aerogels for organic electric double-layer capacitor electrodes," *Electrochim. Acta*, vol. 223, pp. 21–30, 2017, doi: 10.1016/j.electacta.2016.11.177.

[50] L. J. Wang *et al.*, "Flash Converted Graphene for Ultra-High Power Supercapacitors," *Adv. Energy Mater.*, vol. 5, no. 18, pp. 1–8, 2015, doi: 10.1002/aenm.201500786.

[51] S. Kerisit, B. Schwenzer, and M. Vijayakumar, "Effects of oxygen-containing

functional groups on supercapacitor performance," *J. Phys. Chem. Lett.*, vol. 5, no. 13, pp. 2330–2334, 2014, doi: 10.1021/jz500900t.

[52] L. Sun *et al.*, "Nitrogen-doped graphene with high nitrogen level via a one-step hydrothermal reaction of graphene oxide with urea for superior capacitive energy storage," *RSC Adv.*, vol. 2, no. 10, pp. 4498–4506, 2012, doi: 10.1039/c2ra01367c.

[53] K. Pinkert *et al.*, "Role of surface functional groups in ordered mesoporous carbide-derived carbon/ionic liquid electrolyte double-layer capacitor interfaces," *ACS Appl. Mater. Interfaces*, vol. 6, no. 4, pp. 2922–2928, 2014, doi: 10.1021/am4055029.

[54] M. P. Kumar, T. Kesavan, G. Kalita, P. Ragupathy, T. N. Narayanan, and D. K. Pattanayak, "On the large capacitance of nitrogen doped graphene derived by a facile route," *RSC Adv.*, vol. 4, no. 73, pp. 38689–38697, 2014, doi: 10.1039/c4ra04927f.

[55] A. K. Geim, "Random walk to graphene (Nobel lecture)," *Angew. Chemie - Int. Ed.*, vol. 50, no. 31, pp. 6966–6985, 2011, doi: 10.1002/anie.201101174.

[56] C. Lee, X. Wei, J. W. Kysar, and J. Hone, "Measurement of the elastic properties and intrinsic strength of monolayer graphene," *Science (80-.).*, vol. 321, no. 5887, pp. 385–388, 2008, doi: 10.1126/science.1157996.

[57] Y. Zhu *et al.*, "Graphene and graphene oxide: Synthesis, properties, and applications," *Adv. Mater.*, vol. 22, no. 35, pp. 3906–3924, 2010, doi: 10.1002/adma.201001068.

[58] Y. Lin, Y. Liao, Z. Chen, and J. W. Connell, "Holey graphene: a unique structural derivative of graphene," *Mater. Res. Lett.*, vol. 5, no. 4, pp. 209–234, 2017, doi: 10.1080/21663831.2016.1271047.

[59] F. Barzegar, A. Bello, J. K. Dangbegnon, N. Manyala, and X. Xia, "Asymmetric supercapacitor based on activated expanded graphite and pinecone tree activated carbon with excellent stability," *Appl. Energy*, vol. 207, pp. 417–426, 2017, doi: 10.1016/j.apenergy.2017.05.110.

[60] K. O. Oyedotun, T. M. Masikhwa, S. Lindberg, A. Matic, P. Johansson, and N. Manyala, “Comparison of ionic liquid electrolyte to aqueous electrolytes on carbon nanofibres supercapacitor electrode derived from oxygen-functionalized graphene,” *Chem. Eng. J.*, vol. 375, p. 121906, 2019, doi: 10.1016/j.cej.2019.121906.

[61] G. H. Films *et al.*, “Flexible Solid-State Supercapacitors Based on Three-Dimensional,” no. 5, pp. 4042–4049, 2013.

[62] S. Mundinamani, “The choice of noble electrolyte for symmetric polyurethane-graphene composite supercapacitors,” *Int. J. Hydrogen Energy*, vol. 44, no. 21, pp. 11240–11246, 2019, doi: 10.1016/j.ijhydene.2019.02.164.

[63] S. Ye, J. Feng, and P. Wu, “Deposition of three-dimensional graphene aerogel on nickel foam as a binder-free supercapacitor electrode,” *ACS Appl. Mater. Interfaces*, vol. 5, no. 15, pp. 7122–7129, 2013, doi: 10.1021/am401458x.

[64] B. Zheng, T. Chen, and F. Xiao, “KOH-activated nitrogen-doped graphene by means of thermal annealing for supercapacitor,” pp. 1809–1814, 2013, doi: 10.1007/s10008-013-2101-8.

[65] K. Kierzek, E. Frackowiak, G. Lota, G. Gryglewicz, and J. Machnikowski, “Electrochemical capacitors based on highly porous carbons prepared by KOH activation,” vol. 49, pp. 515–523, 2004, doi: 10.1016/j.electacta.2003.08.026.

[66] S. Wu, G. Chen, N. Y. Kim, K. Ni, W. Zeng, and Y. Zhao, “Creating Pores on Graphene Platelets by Low-Temperature KOH Activation for Enhanced Electrochemical Performance,” no. 17, pp. 2376–2384, 2016, doi: 10.1002/smll.201503855.

[67] M. Horn, B. Gupta, J. MacLeod, J. Liu, and N. Motta, “Graphene-based supercapacitor electrodes: Addressing challenges in mechanisms and materials,” *Curr. Opin. Green Sustain. Chem.*, vol. 17, pp. 42–48, 2019, doi: 10.1016/j.cogsc.2019.03.004.

[68] M. M. et al . Bhuyan, M.S.A, Uddin, M.n., Islam, “Synthesis of graphene,” *Int. Nano Lett.*, vol. 6, no. 2, pp. 65–83, 2016, doi: 10.1007/s40089-015-0176-1.

[69] W. S. Hummers and R. E. Offeman, “Preparation of Graphitic Oxide,” *J. Am. Chem. Soc.*, vol. 80, no. 6, p. 1339, 1958, doi: 10.1021/ja01539a017.

[70] Y. Hernandez *et al.*, “High-yield production of graphene by liquid-phase exfoliation of graphite,” *Nat. Nanotechnol.*, vol. 3, no. 9, pp. 563–568, 2008, doi: 10.1038/nnano.2008.215.

[71] T. E. Thompson, “Graphite intercalation compounds,” *Phys. Today*, vol. 31, no. 7, pp. 36–45, 1978, doi: 10.1063/1.2995104.

[72] A. A. F. Novoselov, A. K. Geim, S. V. Morozov, D. Jiang, Y. Zhang, S. V. Dubonos, I. V. Grigorieva, “Electric Field Effect in Atomically Thin Carbon Films,” vol. 666, no. 2004, pp. 666–669, 2013, doi: 10.1126/science.1102896.

[73] V. Sharma, A. Garg, and S. Chander Sood, “Graphene Synthesis via Exfoliation of Graphite by Ultrasonication,” *Int. J. Eng. Trends Technol.*, vol. 26, no. 1, pp. 37–42, 2015, doi: 10.14445/22315381/ijett-v26p208.

[74] C. N. R. Rao, U. Maitra, and H. S. S. R. Matte, “Synthesis, Characterization, and Selected Properties of Graphene,” *Graphene Synth. Prop. Phenom.*, pp. 1–47, 2012, doi: 10.1002/9783527651122.ch1.

[75] H. Hashimoto, Y. Muramatsu, Y. Nishina, and H. Asoh, “Bipolar anodic electrochemical exfoliation of graphite powders,” *Electrochem. commun.*, vol. 104, no. June, p. 106475, 2019, doi: 10.1016/j.elecom.2019.06.001.

[76] M. S. A. Bhuyan, M. N. Uddin, M. M. Islam, F. A. Bipasha, and S. S. Hossain, “Synthesis of graphene,” *Int. Nano Lett.*, vol. 6, no. 2, pp. 65–83, 2016, doi: 10.1007/s40089-015-0176-1.

[77] M. Zhou, F. Pu, Z. Wang, and S. Guan, “Nitrogen-doped porous carbons through KOH activation with superior performance in supercapacitors,” *Carbon N. Y.*, vol. 68, pp. 185–194, 2013, doi: 10.1016/j.carbon.2013.10.079.

[78] J. Feng and Z. Guo, “Wettability of graphene: From influencing factors and reversible conversions to potential applications,” *Nanoscale Horizons*, vol. 4, no. 2, pp. 526–530, 2019, doi: 10.1039/c8nh00348c.

[79] O. Akhavan, E. Ghaderi, E. Abouei, S. Hatamie, and E. Ghasemi, *Accelerated differentiation of neural stem cells into neurons on ginseng-reduced graphene oxide sheets*, vol. 66. Elsevier Ltd, 2014.

[80] N. Díez, A. Ƚiwak, S. Gryglewicz, B. Grzyb, and G. Gryglewicz, "Enhanced reduction of graphene oxide by high-pressure hydrothermal treatment," *RSC Adv.*, vol. 5, no. 100, pp. 81831–81837, 2015, doi: 10.1039/c5ra14461b.

[81] M. Wei *et al.*, "Engineering reduced graphene oxides with enhanced electrochemical properties through multiple-step reductions," *Electrochim. Acta*, vol. 258, pp. 735–743, 2017, doi: 10.1016/j.electacta.2017.11.120.

[82] Z. Wei *et al.*, "Nanoscale tunable reduction of graphene oxide for graphene electronics," *Science (80-.).*, vol. 328, no. 5984, pp. 1373–1376, 2010, doi: 10.1126/science.1188119.

[83] R. S. Cherian, S. Sandeman, S. Ray, I. N. Savina, J. Ashtami, and P. V. Mohanan, "Green synthesis of Pluronic stabilized reduced graphene oxide: Chemical and biological characterization," *Colloids Surfaces B Biointerfaces*, vol. 179, pp. 94–106, 2019, doi: 10.1016/j.colsurfb.2019.03.043.

[84] W. Gao, "The chemistry of graphene oxide," *Graphene Oxide Reduct. Recipes, Spectrosc. Appl.*, pp. 61–95, 2015, doi: 10.1007/978-3-319-15500-5_3.

[85] H. Wang, Q. Fu, and C. Pan, "Green mass synthesis of graphene oxide and its MnO 2 composite for high performance supercapacitor," *Electrochim. Acta*, vol. 312, pp. 11–21, 2019, doi: 10.1016/j.electacta.2019.04.178.

[86] M. Ghorbani, H. Abdizadeh, and M. R. Golobostanfard, "Reduction of Graphene Oxide via Modified Hydrothermal Method," *Procedia Mater. Sci.*, vol. 11, no. 2009, pp. 326–330, 2015, doi: 10.1016/j.mspro.2015.11.104.

[87] J. M. Calo, "Carbon activation with KOH as explored by temperature programmed techniques , and the effects of hydrogen," vol. 45, pp. 2529–2536, 2007, doi: 10.1016/j.carbon.2007.08.021.

[88] J. Díaz-Terán, D. M. Nevskaia, J. L. G. Fierro, A. J. López-Peinado, and A.

Jerez, “Study of chemical activation process of a lignocellulosic material with KOH by XPS and XRD,” *Microporous Mesoporous Mater.*, vol. 60, no. 1–3, pp. 173–181, 2003, doi: 10.1016/S1387-1811(03)00338-X.

[89] M. Kunowsky, B. Weinberger, and F. L. Darkrim, “Impact of the carbonisation temperature on the activation of carbon fibres and their application for hydrogen storage.”

[90] B. Khalid, Q. Meng, R. Akram, and B. Cao, “Effects of KOH activation on surface area , porosity and desalination performance of coconut carbon electrodes,” vol. 3994, no. January, 2016, doi: 10.1080/19443994.2014.979448.

[91] M. Li, W. Li, and S. Liu, “Hydrothermal synthesis , characterization , and KOH activation of carbon spheres from glucose,” *Carbohydr. Res.*, vol. 346, no. 8, pp. 999–1004, 2011, doi: 10.1016/j.carres.2011.03.020.

[92] X. Gao, C. Zhan, X. Yu, Q. Liang, R. Lv, and G. Gai, “A High Performance Lithium-Ion Capacitor with Both Electrodes Prepared from Sri Lanka Graphite Ore,” 2017, doi: 10.3390/ma10040414.

[93] C. Lenser and N. H. Menzler, “Impedance characterization of supported oxygen ion conducting electrolytes,” *Solid State Ionics*, vol. 334, no. January, pp. 70–81, 2019, doi: 10.1016/j.ssi.2019.01.031.

[94] L. Yu and G. Z. Chen, “Ionic Liquid-Based Electrolytes for Supercapacitor and Supercapattery,” *Front. Chem.*, vol. 7, 2019, doi: 10.3389/fchem.2019.00272.

[95] S. K. Tiwari, J. Mishra, G. Hatui, and G. C. Nayak, “Conducting Polymer Hybrids,” pp. 117–142, 2017, doi: 10.1007/978-3-319-46458-9.

[96] J. Zhang, C. Zhong, Y. Deng, W. Hu, J. Qiao, and L. Zhang, “A review of electrolyte materials and compositions for electrochemical supercapacitors,” *Chem. Soc. Rev.*, vol. 44, no. 21, pp. 7484–7539, 2015, doi: 10.1039/c5cs00303b.

[97] S. Vivekchand and C. Rout, “Graphene-based electrochemical supercapacitors,” *J. Chem. ...*, vol. 120, no. 1, pp. 9–13, 2008.

[98] A. Raghunandanan, M. Yeddala, P. Padikassu, and R. Pitchai, “Partially Exfoliated Graphite Paper as Free-Standing Electrode for Supercapacitors,” *ChemistrySelect*, vol. 3, no. 18, pp. 5032–5039, 2018, doi: 10.1002/slct.201800370.

[99] Z. Zhao, X. Wang, M. Yao, L. Liu, Z. Niu, and J. Chen, “Activated carbon felts with exfoliated graphene nanosheets for flexible all-solid-state supercapacitors,” *Chinese Chem. Lett.*, vol. 30, no. 4, pp. 915–918, 2019, doi: 10.1016/j.cclet.2019.03.003.

[100] M. Ghaffari *et al.*, “High-Volumetric Performance Aligned Nano- Porous Microwave Exfoliated Graphite Oxide-based Electrochemical Capacitors,” pp. 4879–4885, 2013, doi: 10.1002/adma.201301243.

[101] M. Hamedi, J. Wigenius, F. Tai, P. Björk, and D. Aili, “Linköping University Post Print Polypeptide-guided assembly of conducting polymer nanocomposites Polypeptide-Guided Assembly of Conducting Polymer Nanocomposites,” no. 2, pp. 2058–2061, 2010, doi: 10.1039/b000000x.

[102] H. Y. Li, Y. Yu, L. Liu, L. Liu, and Y. Wu, “One-step electrochemically expanded graphite foil for flexible all-solid supercapacitor with high rate performance,” *Electrochim. Acta*, vol. 228, pp. 553–561, 2017, doi: 10.1016/j.electacta.2017.01.063.

[103] M. Kyung *et al.*, “Factors in electrode fabrication for performance enhancement of anion exchange membrane water electrolysis,” *J. Power Sources*, vol. 347, pp. 283–290, 2017, doi: 10.1016/j.jpowsour.2017.02.058.

[104] Y. He *et al.*, “Capacitive mechanism of oxygen functional groups on carbon surface in supercapacitors,” *Electrochim. Acta*, vol. 282, no. 5, pp. 618–625, 2018, doi: 10.1016/j.electacta.2018.06.103.

[105] A. Bakandritsos, P. Jakubec, M. Pykal, and M. Otyepka, “Covalently functionalized graphene as a supercapacitor electrode material,” *FlatChem*, vol. 13, no. December, pp. 25–33, 2019, doi: 10.1016/j.flatc.2018.12.004.

[106] L. Guan, L. Yu, and G. Z. Chen, “Capacitive and non-capacitive faradaic charge

storage," *Electrochim. Acta*, vol. 206, pp. 464–478, 2016, doi: 10.1016/j.electacta.2016.01.213.

[107] M. J. Bleda-Martínez, J. A. Maciá-Agulló, D. Lozano-Castelló, E. Morallón, D. Cazorla-Amorós, and A. Linares-Solano, "Role of surface chemistry on electric double layer capacitance of carbon materials," *Carbon N. Y.*, vol. 43, no. 13, pp. 2677–2684, 2005, doi: 10.1016/j.carbon.2005.05.027.

[108] Y. Wang *et al.*, "Supercapacitor devices based on graphene materials," *J. Phys. Chem. C*, vol. 113, no. 30, pp. 13103–13107, 2009, doi: 10.1021/jp902214f.

[109] F. Barzegar, A. Bello, D. Momodu, M. J. Madito, J. Dangbegnon, and N. Manyala, "Preparation and characterization of porous carbon from expanded graphite for high energy density supercapacitor in aqueous electrolyte," *J. Power Sources*, vol. 309, pp. 245–253, 2016, doi: 10.1016/j.jpowsour.2016.01.097.

[110] N. C. Karunarathne and A. C. Wijayasinghe, "Amelioration of Sri Lankan Vein Graphite As an Advance Electrode Material for the Anode Application in Li-Ion Rechargeable Batteries Electrode Material for the Anode Application in Li-Ion," no. December, pp. 159–162, 2015.

[111] H. P. T. Sasanka Hewathilake, N. Karunarathne, A. Wijayasinghe, N. W. B. Balasooriya, and A. K. Arof, "Performance of developed natural vein graphite as the anode material of rechargeable lithium ion batteries," *Ionics (Kiel).*, vol. 23, no. 6, pp. 1417–1422, 2017, doi: 10.1007/s11581-016-1953-1.

[112] T. H. N. G. Amaraweera, N. W. B. Balasooriya, and H. W. M. A. C. Wijayasinghe, "Purity Enhancement of Sri Lankan Vein Graphite for Lithium - ion Rechargeable Battery Anode," *29th Tech. Sess. Geol. Soc. Sri Lanka*, vol. 2013, pp. 101–104, 2013.

[113] S. Lanka, S. Lanka, S. Lanka, S. Lanka, and S. Lanka, "Physical and Chemical Purification of Sri Lankan Flake," vol. 2017, no. January 2015, pp. 163–166, 2015.

[114] N. G. Amaraweera and A. C. Wijayasinghe, "Study of Thermal Behavior of

Vein Graphite for Advance Study of Thermal Behavior of Vein Graphite for Advance Technological Applications," no. April, 2017.

[115] T. H. N. G. Amaraweera, N. W. B. Balasooriya, H. W. M. A. C. Wijayasinghe, A. N. B. Attanayake, B. E. Mellander, and M. A. K. L. Dissanayake, "Surface modification of natural vein graphite for the anode application in Li-ion rechargeable batteries," *Ionics (Kiel).*, vol. 24, no. 11, pp. 3423–3429, 2018, doi: 10.1007/s11581-018-2523-5.

[116] C. B. Dissanayake, R. P. Gunawardena, and D. M. S. K. Dinalankara, "Trace elements in vein graphite of Sri Lanka," *Chem. Geol.*, vol. 68, no. 1–2, pp. 121–128, 1988, doi: 10.1016/0009-2541(88)90091-5.

[117] N. W. B. Balasooriya, P. Touzain, and P. W. S. K. Bandaranayake, "Lithium electrochemical intercalation into mechanically and chemically treated Sri Lanka natural graphite," *J. Phys. Chem. Solids*, vol. 67, no. 5–6, pp. 1213–1217, 2006, doi: 10.1016/j.jpcs.2006.01.051.

[118] W. Zhang *et al.*, "Fast and considerable adsorption of methylene blue dye onto graphene oxide," *Bull. Environ. Contam. Toxicol.*, vol. 87, no. 1, pp. 86–90, 2011, doi: 10.1007/s00128-011-0304-1.

[119] P. Montes-Navajas, N. G. Asenjo, R. Santamaría, R. Menéndez, A. Corma, and H. García, "Surface area measurement of graphene oxide in aqueous solutions," *Langmuir*, vol. 29, no. 44, pp. 13443–13448, 2013, doi: 10.1021/la4029904.

[120] C. A. Nunes and M. C. Guerreiro, "Estimation of surface area and pore volume of activated carbons by methylene blue and iodine numbers," *Quim. Nova*, vol. 34, no. 3, pp. 472–476, 2011, doi: 10.1590/S0100-40422011000300020.

[121] S. Altenor, B. Carene, E. Emmanuel, J. Lambert, J. J. Ehrhardt, and S. Gaspard, "Adsorption studies of methylene blue and phenol onto vetiver roots activated carbon prepared by chemical activation," *J. Hazard. Mater.*, vol. 165, no. 1–3, pp. 1029–1039, 2009, doi: 10.1016/j.jhazmat.2008.10.133.

[122] G. Annadurai, L. Y. Ling, and J. F. Lee, "Adsorption of reactive dye from an aqueous solution by chitosan: isotherm, kinetic and thermodynamic analysis,"

J. Hazard. Mater., vol. 152, no. 1, pp. 337–346, 2008, doi: 10.1016/j.jhazmat.2007.07.002.

[123] Y. Li *et al.*, "Methylene blue adsorption on graphene oxide/calcium alginate composites," *Carbohydr. Polym.*, vol. 95, no. 1, pp. 501–507, 2013, doi: 10.1016/j.carbpol.2013.01.094.

[124] Y. Li *et al.*, "Comparative study of methylene blue dye adsorption onto activated carbon, graphene oxide, and carbon nanotubes," *Chem. Eng. Res. Des.*, vol. 91, no. 2, pp. 361–368, 2013, doi: 10.1016/j.cherd.2012.07.007.

[125] A. S. Franca, L. S. Oliveira, and M. E. Ferreira, "Kinetics and equilibrium studies of methylene blue adsorption by spent coffee grounds," *Desalination*, vol. 249, no. 1, pp. 267–272, 2009, doi: 10.1016/j.desal.2008.11.017.

[126] G. A. Adebisi, Z. Z. Chowdhury, and P. A. Alaba, "Equilibrium, kinetic, and thermodynamic studies of lead ion and zinc ion adsorption from aqueous solution onto activated carbon prepared from palm oil mill effluent," *J. Clean. Prod.*, vol. 148, pp. 958–968, 2017, doi: 10.1016/j.jclepro.2017.02.047.

[127] G. Crini and P. M. Badot, "Application of chitosan, a natural aminopolysaccharide, for dye removal from aqueous solutions by adsorption processes using batch studies: A review of recent literature," *Prog. Polym. Sci.*, vol. 33, no. 4, pp. 399–447, 2008, doi: 10.1016/j.progpolymsci.2007.11.001.

[128] O. Adam, "Removal of Resorcinol from Aqueous Solution by Activated Carbon: Isotherms, Thermodynamics and Kinetics," *Am. Chem. Sci. J.*, vol. 16, no. 1, pp. 1–13, 2016, doi: 10.9734/acsj/2016/27637.

[129] C. Srinivasakannan and N. Balasubramaniam, "Analysis of various experimental methods and preparation of mesoporous activated carbon powders from sawdust using phosphoric acid," *Part. Sci. Technol.*, vol. 25, no. 6, pp. 535–548, 2007, doi: 10.1080/02726350701490896.

[130] S. J. Allen, G. Mckay, and J. F. Porter, "Adsorption isotherm models for basic dye adsorption by peat in single and binary component systems," vol. 280, pp. 322–333, 2004, doi: 10.1016/j.jcis.2004.08.078.

[131] M. M. El Jamal, H. A. Awala, and M. M. El Jamal, “Equilibrium and kinetics study of some dyes onto feldspar,” no. Iv, pp. 45–52, 2011.

[132] A. Regti, A. El Kassimi, M. R. Laamari, and M. El Haddad, “Competitive adsorption and optimization of binary mixture of textile dyes : A factorial design analysis,” *J. Assoc. Arab Univ. Basic Appl. Sci.*, 2016, doi: 10.1016/j.jaubas.2016.07.005.

[133] R. Farkas, “Methylene Blue Adsorption Study on Microcline Particles in the Function of Particle Size Range,” 2019.

[134] M. Sohail *et al.*, “Modified and improved Hummer’s synthesis of graphene oxide for capacitors applications,” *Mod. Electron. Mater.*, vol. 3, no. 3, pp. 110–116, 2017, doi: 10.1016/j.moem.2017.07.002.

[135] W. Peng, G. Han, Y. Huang, Y. Cao, and S. Song, “Insight the effect of crystallinity of natural graphite on the electrochemical performance of reduced graphene oxide,” *Results Phys.*, vol. 11, no. July, pp. 131–137, 2018, doi: 10.1016/j.rinp.2018.08.055.

[136] G. J. Simandl, S. Paradis, and C. Akam, “Graphite deposit types , their origin , and economic significance,” *Br. Columbia Geol. Surv. Pap.*, vol. 3, no. Symposium on Strategic and Critical Materials Proceedings, pp. 163–171, 2015.

[137] C. W. Chang, M. H. Hon, and I. C. Leu, “Ultrasound-Assisted Preparation of Large-Area Few-Layer Graphene,” *ECS J. Solid State Sci. Technol.*, vol. 4, no. 3, pp. M18–M23, 2015, doi: 10.1149/2.0261503jss.

[138] C. H. Manoratne, S. R. D. Rosa, and I. R. M. Kottegoda, “XRD-HTA, UV Visible, FTIR and SEM Interpretation of Reduced Graphene Oxide Synthesized from High Purity Vein Graphite,” *Mater. Sci. Res. India*, vol. 14, no. 1, pp. 19–30, 2017, doi: 10.13005/msri/140104.

[139] N. I. Zaaba, K. L. Foo, U. Hashim, S. J. Tan, W. W. Liu, and C. H. Voon, “Synthesis of Graphene Oxide using Modified Hummers Method: Solvent Influence,” *Procedia Eng.*, vol. 184, pp. 469–477, 2017, doi: 10.1016/j.proeng.2017.04.118.

[140] S. N. Alam, N. Sharma, and L. Kumar, “Synthesis of Graphene Oxide (GO) by Modified Hummers Method and Its Thermal Reduction to Obtain Reduced Graphene Oxide (rGO)*,” *Graphene*, vol. 06, no. 01, pp. 1–18, 2017, doi: 10.4236/graphene.2017.61001.

[141] J. Wang and S. Kaskel, “Feature article: KOH activation of carbon-based materials for energy storage,” no. June 2004, 2012, doi: 10.1039/c2jm34066f.

[142] F. F. Hatta, M. Z. A. Yahya, A. M. M. Ali, R. H. Y. Subban, M. K. Harun, and A. A. Mohamad, “Electrical conductivity studies on PVA/PVP-KOH alkaline solid polymer blend electrolyte,” *Ionics (Kiel).*, vol. 11, no. 5–6, pp. 418–422, 2005, doi: 10.1007/BF02430259.

[143] A. C. Lua and T. Yang, “Effect of activation temperature on the textural and chemical properties of potassium hydroxide activated carbon prepared from pistachio-nut shell,” *J. Colloid Interface Sci.*, vol. 274, no. 2, pp. 594–601, 2004, doi: 10.1016/j.jcis.2003.10.001.